國立臺灣海洋大學

河海工程學系

碩士學位論文

指導教授：陳正宗 博士

零場積分方程求解含圓形夾雜
之反平面壓電問題
Null-field approach for multiple circular inclusion problems in anti-plane piezoelectricity

研究生：吳安傑 撰

中華民國 95 年 6 月

零場積分方程求解含圓形夾雜之反平面壓電問題

Null-field approach for multiple circular inclusion problems in anti-plane piezoelectricity

研 究 生：吳安傑   Student：An-Chien Wu

指導教授：陳正宗   Advisor：Jeng-Tzong Chen

國 立 臺 灣 海 洋 大 學
河 海 工 程 學 系
碩 士 論 文

A Thesis
Submitted to Department of Harbor and River Engineering
College of Engineering
National Taiwan Ocean University
In Partial Fulfillment of the Requirements
for the Degree of
Master of Science
in
Harbor and River Engineering
June 2006
Keelung, Taiwan, Republic of China

中 華 民 國 95 年 6 月

國立臺灣海洋大學
博碩士論文全文上網授權書

本授權書所授權之論文為授權人在 國立臺灣海洋大學河海工程學系 94 學年度取得 碩士 學位之論文。

記錄編號：G0M93520008

論文題目：零場積分方程求解含圓形夾雜之反平面壓電問題
指導教授：陳正宗

■ 同意
茲同意將授權人擁有著作權之上列論文全文電子檔(含摘要)，依下述授權範圍，以非專屬、無償授權國立台灣海洋大學圖書館，不限地域、時間與次數，以微縮、光碟或其他各種數位化方式將上列論文重製，並得將數位化之上列論文及論文電子檔以上載網路方式，提供讀者基於個人非營利性質之線上檢索、閱覽、下載或列印。

■ 讀者基於非營利性質之線上檢索、閱覽、下載或列印上列論文，應依著作權法相關規定辦理。

論文全文上載網路公開之範圍及時間：

| 校內區域網路 | ■ 立即公開 |
| 校外網際網路 | ■ 立即公開 |

授 權 人：吳安傑
學　　　號：M93520008
E-mail：*chien71@msn.com*
親筆簽名或蓋章：

民 國 95 年 7 月 25 日

國家圖書館
博碩士論文電子檔案上網授權書

本授權書所授權之論文為授權人在 國立臺灣海洋大學河海工程學系 94 學年度第 二 學期取得碩士學位之論文。

論文題目：零場積分方程求解含圓形夾雜之反平面壓電問題
指導教授：陳正宗

茲同意將授權人擁有著作權之上列論文全文（含摘要），非專屬、無償授權國家圖書館，不限地域、時間與次數，以微縮、光碟或其他各種數位化方式將上列論文重製，並得將數位化之上列論文及論文電子檔以上載網路方式，提供讀者基於個人非營利性質之線上檢索、閱覽、下載或列印。

☐ 上列論文為授權人向經濟部智慧財產局申請專利之附件或相關文件之一（專利申請案號： ），請於 年 月 日後再將上列論文公開或上載網路。
☐ 因上列論文尚未正式對外發表，請於 年 月 日後再將上列論文公開或上載網路。

授權人：吳安傑
親筆簽名及蓋章：＿＿＿＿＿＿＿＿ 民國 95 年 7 月 25 日
身分證字號：F125789517
電話：(02) 2247-2903
聯絡地址：台北縣中和市復興路328號4樓
E-Mail：*chein71@msn.com*

誌 謝

<div style="text-align: right">

吳安傑 An-Chien Wu

2006/07/24 於力學聲響振動實驗室

</div>

Null-field approach for multiple circular inclusion problems in anti-plane piezoelectricity

Contents

Table captions

Figure captions

Notations

a	vector of forcing terms due to the coupling behavior of remote anti-plane shears and in-plane electric fields
$A(\cdot)$, $B(\cdot)$	bases of the degenerate kernel
a_n, b_n	Fourier coefficients of the boundary density $\varphi(s)$ ($n = 0, 1, 2, \cdots, L$)
b	vector of forcing terms due to remote electric fields without the coupling behavior
B	boundary
B_k	circular boundary ($k = 0, 1, 2, \cdots, N$)
c	vector of forcing terms due to remote shears
c_k	center of the circular boundary ($k = 0, 1, 2, \cdots, N$)
c_{44}	shear modulus for piezoelectric materials
c_{44}^M, c_{44}^I	shear moduli for the piezoelectric matrix and inclusions
$\mathbf{c}_{44}^M$, $\mathbf{c}_{44}^I$	diagonal matrices due to c_{44} of the piezoelectric matrix and inclusions
$C.P.V.$	Cauchy principal value
d	distance between two circular boundaries at the closest points
D	domain of interest
D^c	complementary domain
D_x, D_y	electric displacement components in the x and y directions
D_r, D_θ	radial and tangential components of electric displacements
D_r^M, D_θ^M, D_r^I, D_θ^I	radial and tangential components of electric displacements in the piezoelectric matrix and inclusions
e_x, e_y	eccentric distances in the x and y directions
e_{15}	piezoelectric constant for piezoelectric materials
e_{15}^M, e_{15}^I	piezoelectric constants for the piezoelectric matrix and inclusions
$\mathbf{e}_{15}^M$, $\mathbf{e}_{15}^I$	diagonal matrices due to e_{15} of the piezoelectric matrix and inclusions
E_x^∞, E_y^∞	electric fields in the x and y directions applied at infinity
E_z	electric field component in the z direction
E_r, E_θ	radial and tangential components of electric fields
E_r^M, E_θ^M,	radial and tangential components of electric fields in the piezoelectric

u, v, w	displacements in the x, y and z directions
$U(\mathrm{s},\mathrm{x})$	kernel function in the singular formulation
$U^i(\mathrm{s},\mathrm{x})$	degenerate kernel function of $U(\mathrm{s},\mathrm{x})$ for $R \geq \rho$
$U^e(\mathrm{s},\mathrm{x})$	degenerate kernel function of $U(\mathrm{s},\mathrm{x})$ for $\rho > R$
$\mathbf{U}$	influence matrix of the kernel function $U(\mathrm{s},\mathrm{x})$
$\mathbf{U}^M$, $\mathbf{U}^I$	influence matrices of the kernel function $U(\mathrm{s},\mathrm{x})$ for the matrix and inclusions
V_∞	velocity at infinity
$w(\mathrm{s})$	potential function of the displacement field at the source point s
w^∞	displacement at infinity
w^M, w^I	displacements in the matrix and inclusions
$\mathbf{w}^\infty$	vector of Fourier coefficients for boundary densities at infinity
$\mathbf{w}^M$, $\mathbf{w}^I$	vectors of Fourier coefficients for boundary densities in the matrix and inclusions
x	field point
x, y, z	Cartesian coordinates
β	orientation between two piezoelectric inclusions
$\delta(\mathrm{x}-\mathrm{s})$	Dirac-delta function
ε_0	permittivity of free space
ε	observed distance for boundary-layer effect
ε_k	dielectric constants for the dielectric matrix and inclusions ($k = 0, 1, 2, \cdots, N$)
ε_{11}	dielectric constant for piezoelectric materials
ε_{11}^M, ε_{11}^I	dielectric constants for the piezoelectric matrix and inclusions
$\boldsymbol{\varepsilon}_{11}^M$, $\boldsymbol{\varepsilon}_{11}^I$	diagonal matrices due to ε_{11} of the piezoelectric matrix and inclusions
γ_{zr}, $\gamma_{z\theta}$	radial and tangential components of shear strains
$\mathcal{L}$	operator
μ	shear modulus for elastic materials
μ_k	shear modulus for the elastic matrix and inclusions ($k = 0, 1, 2, \cdots, N$)
$\boldsymbol{\mu}_k$	diagonal matrix for shear moduli of the matrix and inclusions ($k = 0, 1, 2, \cdots, N$)
φ	vector of Fourier coefficients $\left\{ a_0 \quad a_1 \quad b_1 \quad \cdots \quad a_M \quad b_M \right\}^T$
$\varphi(\mathrm{s})$	potential function at the source point s

$\varphi(\mathrm{x})$	potential function at the field point x
Φ	electric potential
$\Phi(\mathrm{s})$	potential function of the electric potential at the source point s
Φ^M , Φ^I	electric potentials in the piezoelectric matrix and inclusions
$\mathbf{\Phi}^\infty$	vector of Fourier coefficients for boundary densities at infinity
$\mathbf{\Phi}^M$, $\mathbf{\Phi}^I$	vectors of Fourier coefficients for boundary densities in the matrix and inclusions
ψ	vector of Fourier coefficients $\left\{ p_0 \quad p_1 \quad q_1 \quad \cdots \quad p_M \quad q_M \right\}^T$
$\psi(\mathrm{s})$	normal derivative of $\varphi(\mathrm{s})$ at the source point s
$\Psi(\mathrm{s})$	normal derivative of $\Phi(\mathrm{s})$ at the source point s
$\mathbf{\Psi}^\infty$	vector of Fourier coefficients for boundary densities at infinity
$\mathbf{\Psi}^M$, $\mathbf{\Psi}^I$	vectors of Fourier coefficients for boundary densities in the matrix and inclusions
(R,θ,ϑ)	spherical coordinates of the source point s
(R,θ)	polar coordinates of the source point s
(ρ,ϕ)	polar coordinates of the field point x
σ_{zx} , σ_{zy}	shear stress components in the x and y directions
σ_{zx}^∞ , σ_{zy}^∞	shear stresses in the x and y directions applied at infinity
σ_{zr} , $\sigma_{z\theta}$	normal and tangential components of shear stresses
σ_{zr}^M , $\sigma_{z\theta}^M$, σ_{zr}^I , $\sigma_{z\theta}^I$	normal and tangential components of shear stresses in the matrix and inclusions
τ_∞	magnitude of applied shear stress at infinity
ξ , ζ	angles of radial and tangential gradient for the vector decomposition
∇^2	Laplacian operator

Abstract

In contrast to other numerical methods, the boundary integral equation method and boundary element method involve singular integrals. Although fictitious boundary element method and null-field integral formulation can avoid the singularity, they both result in an ill-posed model for direct problems. To avoid the singularity and to obtain a well-posed model at the same time are our goals. In this thesis, a unified formulation for solving boundary value problems with multiple circular inclusions using the null-field approach is proposed although our focus is on the Laplace problem only. The subdomain approach, namely, the concept of taking free body, is adopted for inclusion problems. For each subdomain, the null-field integral equation as well as boundary integral equation is derived. To fully capture the circular geometries, separable expressions of fundamental solutions in the adaptive observer system for field and source points and Fourier series for boundary densities are adopted to analytically calculate the boundary integral and to ensure the exponential convergence. By collocating the null-field point on the real boundary, singular and hypersingular integrals are transformed to series sums after introducing the concept of degenerate kernels. Not only the singularity but also senses of principle values are novelly avoided. Then the linear algebraic system is obtained after matching the boundary condition and the unknown coefficients can be easily determined. For the calculation of boundary stress, the Hadamard principal value for hypersingularity is not required and can be easily calculated by using series sums. For the eccentric case, the vector decomposition technique for the radial and tangential derivatives is carefully considered in implementing the hypersingular equation. At the same time, the boundary-layer effect is eliminated owing to the introduction of degenerate kernels. Convergence rate using various terms of Fourier series is also examined. Because the solution is formulated in a manner of semi-analytical form, it possesses certain advantages over the conventional boundary element method. Finally, three topics of engineering applications, anti-plane piezoelectricity, in-plane electrostatic and anti-plane elasticity problems, were given to demonstrate the accuracy and efficiency of present method after comparing with other

available methods. It is found that the stress and electric field concentrations are dependent on the distance between the two inclusions, the mismatch in the material constants and the magnitude of mechanical and electromechanical loadings. A general-purpose program for multiple circular inclusions of various radii, arbitrary positions and different materials constants was developed.

Keywords: degenerate kernel, Fourier series, null-field approach, inclusion, anti-plane deformation, piezoelectricity, boundary-layer effect

中文摘要

相較於其它數值方法，邊界積分方程法與邊界元素法皆會引入奇異積分。雖然虛擬邊界元素法與零場積分方程法可以避免奇異積分，卻會造成矩陣病態問題。本文目標則是提出一套可同時避免奇異積分並獲得良態模式的系統性解法，求解含多圓形夾雜之邊界值問題。利用多領域法，即切取自由體圖的觀念，對於每個次領域而言都可使用零場積分方程與邊界積分方程求解。其中，將基本解以場、源點分離的概念展開為分離（退化）的型式，而邊界物理量則以傅立葉級數展開，搭配自適性觀察座標系統可解析求出邊界積分及確保級數指數收斂。經由均勻佈點於真實邊界上，奇異與超奇異積分都可被轉換成級數和的形式，且無須面對主值計算問題，在滿足邊界條件後可由所得的線性代數系統輕易地解出未知係數。針對非同心圓的例子，使用超奇異積分式計算勢能導微時，需採用向量分解的技巧來加以處理；而在計算邊界應力時所產生的主值問題也可被轉換成級數和的形式求得。同時，由於分離核（退化核）的引入，邊界層效應可被消除。另外，選取不同項數的傅立葉級數進行收斂分析來測試本方法的收斂速率。相對於傳統邊界元素法，此半解析法擁有某種程度的優越性。最後，為了驗證此方法的準確性與效率性，對反平面壓電問題、平面靜電場問題與反平面彈力問題均予以測試。所得的數值結果也與由其它方法所得之結果加以比較，均能得到不錯的結果。由數值結果可以得知，應力與電場集中的大小取決於兩夾雜間的距離、材料常數與外力的作用大小。經由一系列的研究工作後，我們成功開發出一套系統性求解含任意數目、位置、不同大小與材料常數的圓形夾雜分析程式。

關鍵字：分離核函數、傅立葉級數、零場積分方程、夾雜、反平面位移、壓電力學、邊界層效應

Chapter 1 Introduction

1.1 Motivation of the research and literature review

Engineering analysis can be formulated as mathematical models of the boundary value problems. In order to solve the boundary value problems, researchers and engineers have paid more attention on the development of boundary integral equation method (BIEM), boundary element method (BEM) and meshless method than domain type methods, finite element method (FEM) and finite difference method (FDM). Among various numerical methods, BEM is one of the most popular numerical approaches for solving boundary value problems. Although BEM has been involved as an alternative numerical method for solving engineering problems, four critical issues are of concern.

(1) Treatment of singularity and hypersingularity

It is well known that BEM are based on the use of fundamental solutions to solve partial differential equations. These solutions are two-point functions which are singular as the source and field points coincide. Most of the efforts have been focused on the singular boundary integral equation for problems with ordinary boundaries. In some situations, the singular boundary integral equation is not sufficient, *e.g.* degenerate boundary, fictitious frequency and spurious eigenvalue. Therefore, the hypersingular equation is required. The role of hypersingularity in computational mechanics has been examined in the review article of Chen and Hong [27]. In the past, several regularizations for hypersingularity were offered to handle it in direct and indirect ways. Hong and Chen [99] have developed the theory of dual BIEM and dual BEM with hypersingular kernels. The analytical formula reveals the jump behavior of double-layer potentials. How to determine accurately the free terms has received more attentions in the past decade. To directly face the singular and hypersingular integrals, a large amount of papers on the Cauchy, Riemann and Hadamard principal values have been published through the bump contour approach. Two conventional approaches were employed to regularize the singular and hypersingular integrals. First, Guiggiani [55] has derived the free terms for Laplace and Navier equations using the differential geometry and bump

1

approach in Fig. 1-1 (a). Second, Gray and Manne [51] have employed a limiting process to ensure a unique solution by pushing an interior point to boundary in Fig. 1-1 (b) using the symbolic software. In the present approach, we employed the degenerate kernel to represent the two-point fundamental solution for problems with circular boundaries as shown in Fig. 1-1 (c). Recently, Wu [93] has developed a new boundary integral equation for the analysis of linear elastic bodies with cracks. In his formulation, displacement gradients and tractions on the non-crack boundary and dislocation on the crack line are required instead of displacement and traction in the dual BEM. Numerical quadratures for weak, strong singularities and hypersingularities have been proposed [65]. Chen and Chiu [25] has derived the separable expression of fundamental solution and can avoid calculating the improper integrals along the boundary. The singularity and hypersingularity disappeared in boundary integral equation after describing the potential into two parts. Unlike the conventional BEM and BIEM, Waterman [90] introduced first the so-called T-matrix method for electromagnetic scattering problems. Various names, null-field approach or extended boundary condition method (EBCM), have been coined. The null-field approach or T-matrix method is used widely for obtaining numerical solutions of acoustics [8, 9, 68, 91], elastodynamics [85, 92] and hydrodynamics [69]. Boström [14] introduced a new method of treating the scattering of transient fields by a bounded obstacle in three-dimensional space. He defined new sets of time-dependent basis functions, and use of these to expand the free space Green's function and the incoming and scattered fields. The method is a generalization to the time domain of the null-field approach first given by Waterman [90]. A crucial advantage of the null-field approach or T-matrix method consists in the fact that the influence matrix can be computed easily. Although many works for acoustic, elastodynamic and hydrodynamic problems have been done, only a few articles on elastostatics can be found [73]. The idea of changing real boundary to fictitious boundary (fictitious BEM) or putting the observation point outside the domain (null-field approach) can remove the singular and hypersingular integrals. However, they result in an ill-posed matrix which will be elaborated on later. A

method of well-posed mathematical model and free of directly determining singular and hypersingular integrals is one of our objects in this thesis.

(2) Boundary-layer effect

Boundary-layer effect in BEM has received attention in the recent years. In real applications, data near boundary can be smoothened since maximum principle always exists for potential problems. Nevertheless, it also deserves study to know how to manipulate the nearly singular integrals in applied mathematics. Kisu and Kawahara [63] proposed a concept of relative quantity to eliminate the boundary-layer effect. Chen and Hong in Taiwan [26] as well as Chen *et al.* in China [24] independently extended the idea of relative quantity to two regularization techniques which the boundary densities are subtracted by constant and linear terms. Sladek *et al.* [78, 79] used a regularized version of the stress boundary integral equation (σ BEM) to compute the correct values of stresses close to the boundary better than the non-regularized σ BEM. An interpolation scheme to compute stresses at points very close to the boundary was proposed. Others proposed a regularization of the integrand by variable transformations. For example, Telles *et al.* [84] used a cubic transformation such that its Jacobian is minimum at the point on the boundary close to the collocation point and can smooth the integrand. Similarly, Huang and Cruse [60] proposed rational transformations which regularize the nearly singular integrals. How to eliminate the boundary-layer effect in BEM is vital for researchers. The thesis will identify that the present approach is inherently free of boundary-layer effect.

(3) Convergence rate

Undoubtedly, BEM is very popular for boundary value problems with general geometries since it requires discretization on the boundary only. Regarding to constant, linear and quadratic elements, the discretization scheme does not take the special geometry into consideration. It leads to the slow convergence rate. For problems with special geometries, one can propose the special function to approximate the boundary density on the specific geometry. For example, Fourier series is suitable for boundary densities on circular boundaries while the spherical

harmonic function is always employed to approximate the boundary density on surface of sphere. Legendre and Chebyshev polynomials are suited to approximate the boundary densities on the regular and degenerate straight boundaries, respectively. Methieu function is taken to describe the boundary densities of elliptic boundaries. Figure 1-2 shows randomly distribution holes and/or inclusions with square, elliptic and circular shapes, *etc.* in the two-dimensional region. Bird and Steele [11, 12] have proposed a solution procedure for Laplace and biharmonic problems with circular holes of arbitrary size, position and number. Their method can be seen as one kind of the Trefftz method of interior and exterior problems. The T-complete function can be found in the degenerate kernel of fundamental solution. The equivalence between the method of fundamental solution (MFS) and Trefftz method was recently constructed although both methods have histories of more than sixty years [40]. Boundary densities can be expanded in terms of truncated Fourier series. Caulk and Barone [4, 5, 6, 7, 16, 17, 18, 19] have solved the Laplace problem in two-dimensional region with circular holes by using the special boundary integral equations. In their approach, the boundary potential and its normal derivative are approximated by using Fourier series on each hole. Mogilevskaya and Crouch [44, 71, 87] presented a method for solving problems with randomly distributed circular elastic inclusions with arbitrary properties. They combined the series expansion technique with a complex boundary integral equation method. Although previous researchers have employed the Fourier series expansion, no one has ever introduced the degenerate kernel in boundary integral equations to tackle their problems. Kress has proved that the exponential convergence instead of the algebraic convergence in the BEM can be achieved by using the degenerate kernel and Fourier expansion [64]. This thesis will take advantage of this higher convergence rate to deal with problems with circular boundaries using Fourier series in conjunction with degenerate kernels. Moreover, the present method can be directly applied to problems with general boundaries without any difficulty once the fundamental solution can be separated in the other coordinate, *e.g.* Cartesian coordinate or elliptic coordinate.

(4) Ill-posed model

   As mentioned previously in the first issue, to avoid directly calculating the singular and hypersingular integrals by using null-field approach or fictitious BEM yields an ill-condition system. The influence matrix is not diagonally dominated and needs preconditioning. To approach the fictitious boundary to the real boundary or to move the null-field point to the real boundary can make the system well-posed. However, singularity appears in the meantime. We may wonder is it possible to push the null-field point on the real boundary but free of facing the singular or hypersingular integrals. The answer is yes and the key idea is to describe the jump behavior of potential distribution in the separate region using degenerate (separate) kernels for fundamental solutions. The details will be addressed in this study.

In this thesis, we develop a semi-analytical approach for boundary value problems with circular boundaries by using the null-field integral equation in conjunction with the degenerate kernel and Fourier series. To fully capture the geometry of circular boundary, the fundamental solution and boundary densities are expanded into the degenerate form and Fourier series in the polar coordinate, respectively. Four intermediate advantages are obtained, (1) singularity free, (2) boundary-layer effect free, (3) exponential convergence, (4) well-posed model. The adaptive observer system is proposed to fully employ the property of degenerate kernel. All the boundary integrals are analytically determined through the orthogonal property between the degenerate kernel and Fourier series. Therefore, improper integrals are transformed to series sums instead of the sense of principal values. A linear algebraic equation is formulated to determine the unknown Fourier coefficients after collocating the null-field point on the boundary and matching the boundary condition. For the calculation of potential gradient, the Hadamard principal value for hypersingularity is not required and can be easily calculated by using series sums and by adapting the vector decomposition technique for eccentric cases. In addition, the boundary-layer effect for stress calculations near the boundary and the convergence test with various terms of Fourier series are studied. Engineering applications containing multiple circular inclusions are demonstrated to see the validity of present method. The limiting case of cavities by setting zero modulus is tested to

compare previous results by our NTOU/MSV group. The extension to study on coupling effect of electrical and mechanical loadings for piezoelectricity problems is also done in this thesis.

1.2 Organization of the thesis

The frame of the thesis is shown in Fig. 1-3. In this thesis, the boundary value problems with circular boundaries are studied by using the null-field approach conjunction with degenerate kernels and Fourier series. Applications to anti-plane piezoelectricity problems with circular piezoelectric inclusions subjected to the mechanical and electrical loadings are investigated. Anti-plane elastic and in-plane electrostatic problems can be treated as limiting cases of the piezoelectricity problems. Besides, the boundary-layer effect for stress calculations and the convergence test are addressed. The content of each chapter is summarized below.

In the chapter 2, we present a semi-analytical formulation using the null-field approach in conjunction with degenerate kernel and Fourier series for solving boundary value problems. The kernel function is separated into degenerate (separate) forms and the boundary density is expanded into Fourier series to fully utilize the property of circular geometry. Although the present formulation is suitable for the Laplacian, Helmholtz, biharmonic and biHelmholtz operators in one, two and three dimensional problems, only two-dimensional Laplace problems is adopted here.

In the chapter 3, the application to anti-plane piezoelectricity problems with arbitrary piezoelectric circular inclusions under remote anti-plane shears and in-plane electric fields is considered. Contour plots for the stresses and electric potential are illustrated to see the interaction of piezoelectric inclusions. The distributions of stresses, electric displacements and electric fields along various paths, *e.g.* the interface between the matrix and inclusion, the contour near the circular boundary and the x axis, are calculated. The two piezoelectric circular inclusions problems with different geometries, material constants and magnitudes of mechanical and electromechanical loadings are considered to test our program. Besides, the decoupling electrostatic problems are solved as an uncoupling case. Numerical results are compared with the exact solution

and those of previous researchers by using various methods.

In the chapter 4, we derive the null-field approach for an elastic infinite medium containing elastic circular inclusions with arbitrary radii, positions and material constants under the remote anti-plane shears. It can be seen as a limiting case of anti-plane piezoelectricity problems. The boundary-layer effect for the stress calculation is examined. The exact solution for a single elastic inclusion is also re-derived by using the present formulation. Several problems of two holes, two inclusions, one cavity surrounded by two inclusions and three inclusions are revisited to demonstrate the generality and validity of our method. Regardless of the number, size and the position of circular inclusions and cavities, the proposed method is tested for its generality and validity. Finally, we draw out some concluding remarks item by item and exhibit some further issues in the chapter 5.

Domain point   **Null-field point**
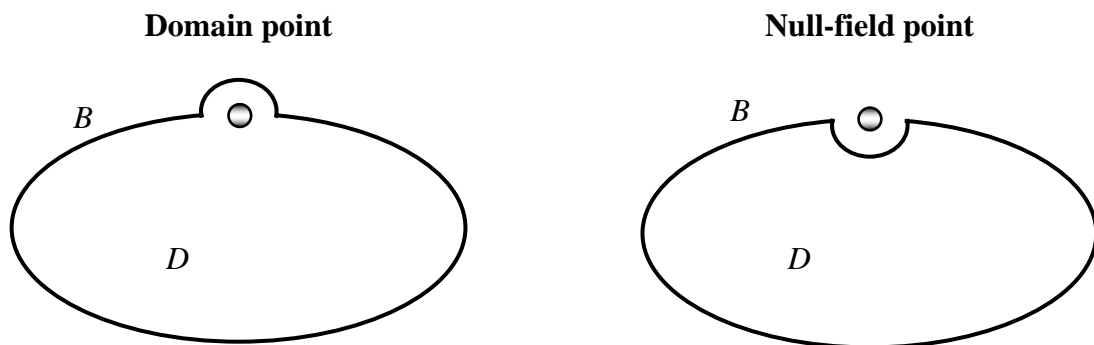
Figure 1-1 (a) Bump contour
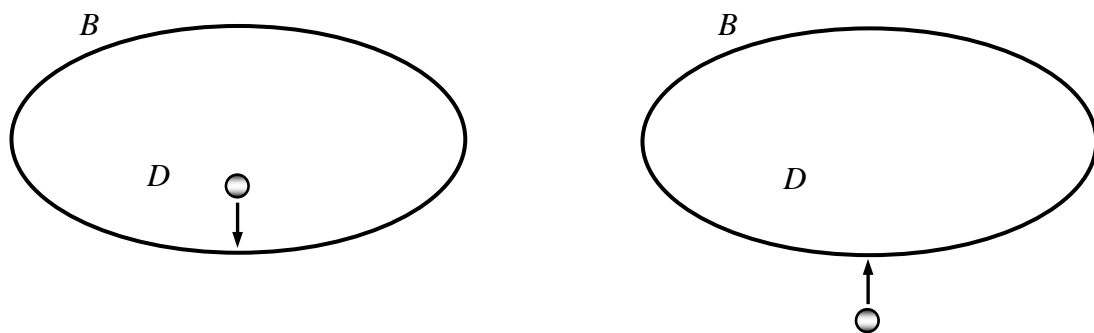
Figure 1-1 (b) Limiting process
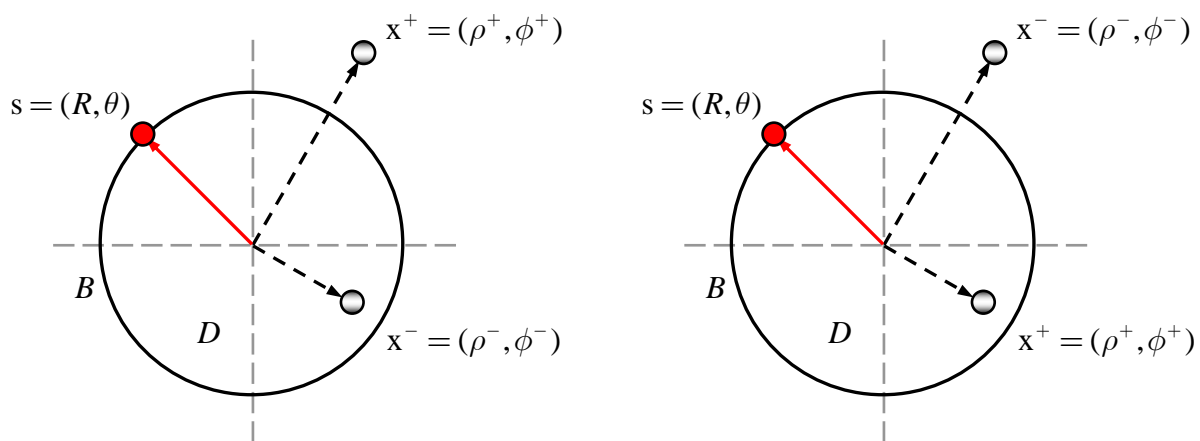
Figure 1-1 (c) Present method
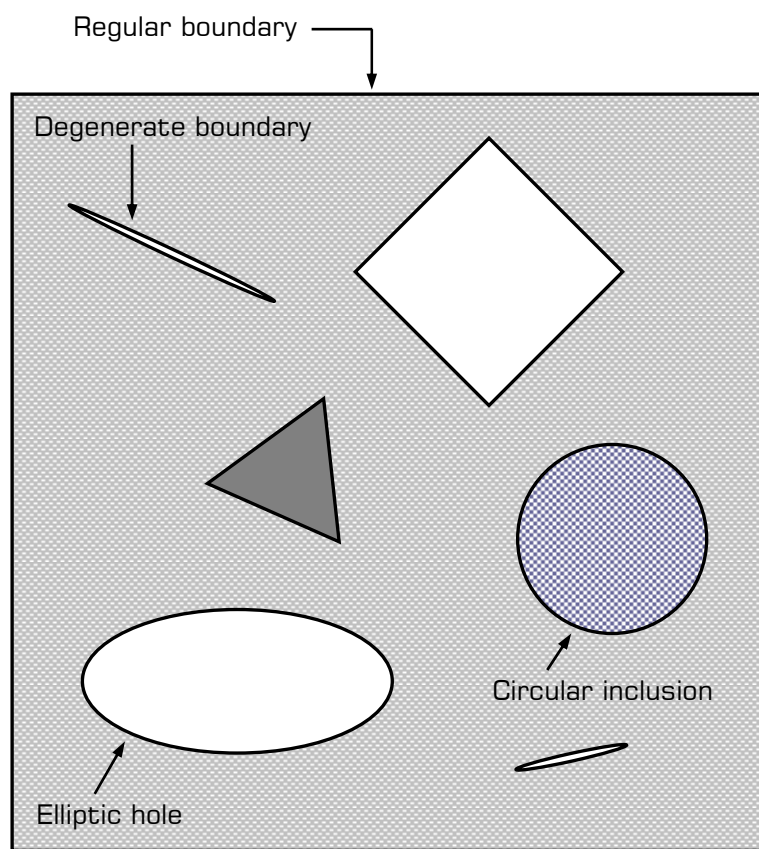
Figure 1-2 A two-dimensional problem with holes, inclusions and cracks

```
┌─────────────────────────────────────────────────────────┐
│                                                         │
│              Chapter 1 Introduction                     │
│                                                         │
└─────────────────────────────────────────────────────────┘
                           │
                           ▼
┌─────────────────────────────────────────────────────────┐
│        Chapter 2 Basic formulation of null-field        │
│    approach for boundary value problems with circular   │
│                      inclusions                         │
└─────────────────────────────────────────────────────────┘
                           │
                           ▼
┌─────────────────────────────────────────────────────────┐
│   Chapter 3 Applications to anti-plane piezoelectricity │
│   and in-plane electrostatic problems with circular     │
│                      inclusions                         │
└─────────────────────────────────────────────────────────┘
                           │
                           ▼
┌─────────────────────────────────────────────────────────┐
│    Chapter 4 Applications to anti-plane elasticity      │
│           problems with circular inclusions             │
└─────────────────────────────────────────────────────────┘
                           │
                           ▼
┌─────────────────────────────────────────────────────────┐
│        Chapter 5 Conclusions and further research       │
└─────────────────────────────────────────────────────────┘
```

Figure 1-3 The frame of the thesis

Chapter 2 Basic formulation of null-field approach for boundary value problems with circular inclusions

Summary

In this chapter, the boundary value problem with circular boundaries is formulated by using the null-field integral equation. Degenerate kernels for fundamental solutions and Fourier series for unknown boundary densities are introduced to derive the formulation analytically. Intermediate advantages are obtained: (1) well-posed model, (2) singularity free, (3) boundary-layer effect free and (4) exponential convergence. The method is basically a numerical approach, and because of its semi-analytical nature, it possesses certain advantages over the conventional boundary element method. The null-field approach employing degenerate kernels can be applied to solve boundary value problems which are governed by the Laplace, Helmholtz, biharmonic and biHelmholtz equations. Inclusion problems for anti-plane elasticity as well as the piezoelectricity study are our main concern.

2.1 Introduction

Many engineering problems can be described by using mathematical models of the Laplace, Helmholtz, biharmonic and biHelmholtz equations. For example, anti-plane piezoelectricity, in-plane electrostatic, anti-plane elasticity, steady state heat conduction, ideal steady flow problems are the classical problems which are always simulated by the Laplace equation. Membrane vibration, water wave and acoustic problems are often modeled by the Helmholtz problems. Plate vibration problems are governed by the biHelmholtz equation. Plate problems in solid mechanics and Stokes' flow in fluid mechanics can be formulated by the biharmonic equation through the Airy stress function and streamfunction, respectively.

Engineers often have the opportunity to apply circular components to engineering structures. Although these structures are rather simple, the analytical solutions for their

engineering system are difficult to obtain. To the author's best knowledge, special mapping technique or bipolar coordinate were always used to derive the analytical solution for two circular holes and/or inclusions, respectively. However, conformal mapping or bipolar coordinate is limited to doubly connected regions even to conforcal connected regions; most efforts have concentrated on special solution representations. Alternative methods have been adopted to solve problems with multiple circular holes [48, 49]. Numerical approaches, *e.g.* finite difference method (FDM), finite element method (FEM), boundary element method (BEM), boundary integral equation method (BIEM) and meshless method, *etc.*, are always resorted to handle the problems. Among diverse numerical approaches, FEM and BEM have become the popular research tools for engineers. In the past decade, FEM has been widely applied to carry out many engineering problems, but one deficiency is that discretizations are time-consuming to generate the mesh. Unlike FEM, the discretizations are restricted only to the boundary when using BEM. The main advantage is one-dimension reduction in mesh generation and particularly convenient for unbounded domain and stress concentration problems. BEM is also ideally suited to the analysis of external problems where domains extend to infinity, since discretizations are confined to the internal boundaries with no need to truncate the domain at a finite distance. There is no doubt that BEM has been appreciated as an alternative numerical method which has been extensively used. Practical engineers and academic researchers paid attention to theoretical study and applications of BEM in the recent decades. Although BEM is recognized as an acceptable tool, some pitfalls still exist, *e.g.* degenerate scale for potential problems, fictitious frequency for exterior acoustics and boundary-layer effect for stress calculations near the boundary. Detailed discussions for the pitfalls of BEM can consult with the three lectures by Chen *et al.* [28, 33, 34].

For problems with circular boundaries, the BIEM can be utilized instead of BEM to improve the convergence rate by introducing Fourier series. The Fourier series expansion is specially tailored to problems with circular geometry. Early attempts to solve problems involving circular boundaries using series expansions were reported by Mogilevskaya and Crouch [44, 71], Barone and Caulk [4-7] and Bird and Steele [11, 12].

Barone and Caulk explored the use of special BIEM for solving Laplace's equation in two-dimensional regions with circular holes. Based on his idea, the boundary potential and its normal derivative were expressed in a finite series of circular harmonics on each hole. Unlike other approaches, the unknown coefficients in each hole are determined by a new set of integral equations with special kernel functions. However, the explicit equations in [16] were limited to the case when a constant potential is specified on the boundary of each hole. Steele and his coworkers [11, 12] have adopted the Fourier series for harmonic and biharmonic problems with circular holes. In their numerical results, only six terms of Fourier series on each hole were sufficient to yield error of less than 0.05 percent. Recently, Mogilevskaya and Crouch [71] also presented a method by employing the Fourier series expansion technique and used the Galerkin method for solving problems with randomly distributed circular elastic inclusions with arbitrary properties. They combined the series expansion technique with a direct BIEM. However, all of previous studies didn't employ the null-field integral equation and degenerate kernels in polar coordinate to fully capture the circular boundary to the author's best knowledge although they have employed the Fourier series. Degenerate kernels play an important role not only for mathematical analysis [39] but also for numerical implementation [64]. For example, the spurious eigenvalue [31], fictitious frequency [30] and degenerate scale [32] have been mathematically and numerically studied by using degenerate kernels for problems with circular boundaries. One gain is that the exponential convergence instead of the algebraic convergence in BEM can be achieved by using the degenerate kernel and Fourier expansion [64].

In the chapter, we focus on the boundary value problems with circular inclusions and propose a semi-analytical approach. A major benefit of using degenerate kernels for the fundamental solution and the Fourier expansion for circular boundaries is that all integrations can be performed analytically instead of calculations using senses of principal values. Besides, the degenerate kernels for fundamental solutions and Fourier series for boundary densities lead to the exponential convergence [64]. After expanding the boundary density along each circular boundary by using the Fourier series expansion, the null-field integral equation yields a system of linear algebraic equations

for unknown coefficients of Fourier series. To match the interface condition between the matrix and each inclusion, additional constraints are provided to determine the unknown Fourier coefficients by the resulted linear algebraic system. A general-purpose program for solving boundary value problems containing circular inclusions with different radii, various center positions and arbitrary material properties is developed.

2.2 Dual boundary integral equations and dual null-field integral equations

Suppose there are N randomly distributed circular inclusions bounded to the contours B_k ($k = 0, 1, 2, \cdots, N$) as shown in Fig. 2-1. We define

$$B = \bigcup_{k=0}^{N} B_k \,. \tag{2-1}$$

In mathematical physics, many engineering problems can be modeled by the governing equation,

$$\mathcal{L}\,\varphi(\mathrm{x}) = 0 \,, \quad \mathrm{x} \in D \,, \tag{2-2}$$

where $\mathcal{L}$ may be the Laplacian, Helmholtz, biharmonic or biHelmholtz operators, $\varphi(\mathrm{x})$ is the potential function and D is the domain of interest. For the two-dimensional second-order operators of Laplacian and Helmholtz, the boundary integral equation for the domain point can be derived from the third Green's identity [27], we have

$$2\pi\varphi(\mathrm{x}) = \int_B T(\mathrm{s}, \mathrm{x})\varphi(\mathrm{s})dB(\mathrm{s}) - \int_B U(\mathrm{s}, \mathrm{x})\psi(\mathrm{s})dB(\mathrm{s}) \,, \quad \mathrm{x} \in D \,, \tag{2-3}$$

$$2\pi\frac{\partial\varphi(\mathrm{x})}{\partial\mathrm{n_x}} = \int_B M(\mathrm{s}, \mathrm{x})\varphi(\mathrm{s})dB(\mathrm{s}) - \int_B L(\mathrm{s}, \mathrm{x})\psi(\mathrm{s})dB(\mathrm{s}) \,, \quad \mathrm{x} \in D \,, \tag{2-4}$$

where s and x are the source and field points, respectively, $\psi(\mathrm{s}) = \partial\varphi(\mathrm{s})/\partial\mathrm{n_s}$, B is the boundary, $\mathrm{n_x}$ denotes the outward normal vector at the field point x and the kernel function $U(\mathrm{s}, \mathrm{x})$ is the fundamental solution which satisfies

$$\mathcal{L}\,U(\mathrm{s}, \mathrm{x}) = 2\pi\delta(\mathrm{x} - \mathrm{s}) \,, \tag{2-5}$$

in which $\delta(\mathrm{x} - \mathrm{s})$ denotes the Dirac-delta function. The other kernel functions, $T(\mathrm{s}, \mathrm{x})$, $L(\mathrm{s}, \mathrm{x})$ and $M(\mathrm{s}, \mathrm{x})$, are defined by

$$T(\mathrm{s},\mathrm{x}) \equiv \frac{\partial U(\mathrm{s},\mathrm{x})}{\partial \mathrm{n}_\mathrm{s}}, \quad L(\mathrm{s},\mathrm{x}) \equiv \frac{\partial U(\mathrm{s},\mathrm{x})}{\partial \mathrm{n}_\mathrm{x}}, \quad M(\mathrm{s},\mathrm{x}) \equiv \frac{\partial^2 U(\mathrm{s},\mathrm{x})}{\partial \mathrm{n}_\mathrm{s} \, \partial \mathrm{n}_\mathrm{x}}, \tag{2-6}$$

where n_s is the outward normal vector at the source point s. By moving the field point to the boundary, Eqs. (2-3) and (2-4) reduce to

$$\pi \varphi(\mathrm{x}) = C.P.V. \int_B T(\mathrm{s},\mathrm{x}) \varphi(\mathrm{s}) dB(\mathrm{s}) - R.P.V. \int_B U(\mathrm{s},\mathrm{x}) \psi(\mathrm{s}) dB(\mathrm{s}), \quad \mathrm{x} \in B, \tag{2-7}$$

$$\pi \frac{\partial \varphi(\mathrm{x})}{\partial \mathrm{n}_\mathrm{x}} = H.P.V. \int_B M(\mathrm{s},\mathrm{x}) \varphi(\mathrm{s}) dB(\mathrm{s}) - C.P.V. \int_B L(\mathrm{s},\mathrm{x}) \psi(\mathrm{s}) dB(\mathrm{s}), \quad \mathrm{x} \in B, \tag{2-8}$$

where $C.P.V.$, $R.P.V.$ and $H.P.V.$ denote the Cauchy principal value, Riemann principal value and Hadamard principal value, respectively. Once the field point x locates outside the domain, the null-field integral equation of the direct method in Eqs. (2-7) and (2-8) yield

$$0 = \int_B T(\mathrm{s},\mathrm{x}) \varphi(\mathrm{s}) dB(\mathrm{s}) - \int_B U(\mathrm{s},\mathrm{x}) \psi(\mathrm{s}) dB(\mathrm{s}), \quad \mathrm{x} \in D^c, \tag{2-9}$$

$$0 = \int_B M(\mathrm{s},\mathrm{x}) \varphi(\mathrm{s}) dB(\mathrm{s}) - \int_B L(\mathrm{s},\mathrm{x}) \psi(\mathrm{s}) dB(\mathrm{s}), \quad \mathrm{x} \in D^c, \tag{2-10}$$

where D^c is the complementary domain. Note that the conventional null-field integral equations are not singular since s and x never coincide. If the kernel function in Eqs. (2-3), (2-4), (2-9) and (2-10) can be described as degenerate (separate) forms for the inside D or outside D^c domain, we have

$$2\pi \varphi(\mathrm{x}) = \int_B T(\mathrm{s},\mathrm{x}) \varphi(\mathrm{s}) dB(\mathrm{s}) - \int_B U(\mathrm{s},\mathrm{x}) \psi(\mathrm{s}) dB(\mathrm{s}), \quad \mathrm{x} \in D \cup B, \tag{2-11}$$

$$2\pi \frac{\partial \varphi(\mathrm{x})}{\partial \mathrm{n}_\mathrm{x}} = \int_B M(\mathrm{s},\mathrm{x}) \varphi(\mathrm{s}) dB(\mathrm{s}) - \int_B L(\mathrm{s},\mathrm{x}) \psi(\mathrm{s}) dB(\mathrm{s}), \quad \mathrm{x} \in D \cup B, \tag{2-12}$$

$$0 = \int_B T(\mathrm{s},\mathrm{x}) \varphi(\mathrm{s}) dB(\mathrm{s}) - \int_B U(\mathrm{s},\mathrm{x}) \psi(\mathrm{s}) dB(\mathrm{s}), \quad \mathrm{x} \in D^c \cup B, \tag{2-13}$$

$$0 = \int_B M(\mathrm{s},\mathrm{x}) \varphi(\mathrm{s}) dB(\mathrm{s}) - \int_B L(\mathrm{s},\mathrm{x}) \psi(\mathrm{s}) dB(\mathrm{s}), \quad \mathrm{x} \in D^c \cup B. \tag{2-14}$$

It is noted that the boundary integral equation for the domain point and the null-field integral equation for the null-field point can include the collocation point on the real boundary since the appropriate kernel can be used as elaborated on later in the following section.

2.3 Expansions of fundamental solution and boundary density

Now, we adopt the mathematical tools, degenerate kernels and Fourier series, for the purpose of analytical study. The combination of degenerate kernels and Fourier series plays the major role in handling problems with circular boundaries. Instead of directly calculating the $C.P.V.$, $R.P.V.$ and $H.P.V.$ in Eqs. (2-7) and (2-8), we obtain the linear algebraic system from the null-field integral equation of Eqs. (2-13) and (2-14) through the kernel expansion by "exactly" collocating the point on the real boundary. Based on the separable property, the kernel function $U(\mathrm{s},\mathrm{x})$ can be expanded into the separable form by dividing the source and field points:

$$U(\mathrm{s},\mathrm{x}) = \begin{cases} U^i(\mathrm{s},\mathrm{x}) = \sum_j A_j(\mathrm{s})B_j(\mathrm{x}), \ |\mathrm{s}| \geq |\mathrm{x}| \\ \\ U^e(\mathrm{s},\mathrm{x}) = \sum_j A_j(\mathrm{x})B_j(\mathrm{s}), \ |\mathrm{x}| > |\mathrm{s}| \end{cases}, \qquad (2\text{-}15)$$

where the bases of $A(\cdot)$ and $B(\cdot)$ can be found for the Laplacian, Helmholtz, biharmonic and biHelmholtz operators and the superscripts "i" and "e" denote the interior ($|\mathrm{s}| \geq |\mathrm{x}|$) and exterior ($|\mathrm{x}| > |\mathrm{s}|$) cases, respectively. To classify the interior (left, 1-D) and exterior (right, 1-D) regions, Figure 2-2 shows for one, two and three dimensional cases. For the degenerate form of T, L and M kernels, they can be derived according to their definitions in Eq. (2-6). For simplicity, Table 2-1 summarizes the main difference between the present formulation and conventional BEM for simply-connected domain problems. Regarding the multiply-connected domain problems, the interior "i" and exterior "e" expansions for the kernel should be taken with care. Although the mathematical tools of degenerate kernels, are suitable for the Laplacian, Helmholtz, biharmonic and biHelmholtz operators in one, two and three dimensional problems, we focus on the two-dimensional Laplace problems in this thesis as explained below.

Degenerate kernels for fundamental solutions:
Based on the separable property, the kernel function $U(\mathrm{s},\mathrm{x}) = \ln r$, ($r \equiv |\mathrm{x}-\mathrm{s}|$), is expanded into the degenerate form by separating the source point and field point in the

polar coordinate [25]:

$$U(\mathrm{s},\mathrm{x}) = \begin{cases} U^i(R,\theta;\rho,\phi) = \ln R - \displaystyle\sum_{m=1}^{\infty} \frac{1}{m}(\frac{\rho}{R})^m \cos m(\theta-\phi), \ R \geq \rho \\ \\ U^e(R,\theta;\rho,\phi) = \ln \rho - \displaystyle\sum_{m=1}^{\infty} \frac{1}{m}(\frac{R}{\rho})^m \cos m(\theta-\phi), \ \rho > R \end{cases}, \qquad (2\text{-}16)$$

where the superscripts "i" and "e" denote the interior ($R > \rho$) and exterior ($\rho > R$) cases, respectively. The origin of the observer system for the degenerate kernel is $(0,0)$. Figure 2-3 shows the graph of separate expressions of fundamental solutions where source point s located at $R = 10.0$ and $\theta = \pi/3$. By setting the origin at o for the observer system, a circle with radius R from the origin o to the source point s is plotted. If the field point x is situated inside the circular region, the degenerate kernel belongs to the interior expression of U^i; otherwise, it is the exterior case. It is noted that the leading term and numerator term in Eq. (2-16) involve the larger argument to ensure the log singularity and series convergence, respectively. After taking the normal derivative $\partial/\partial R$ with respect to Eq. (2-16), the $T(\mathrm{s},\mathrm{x})$ kernel yields

$$T(\mathrm{s},\mathrm{x}) = \begin{cases} T^i(R,\theta;\rho,\phi) = \dfrac{1}{R} + \displaystyle\sum_{m=1}^{\infty}(\frac{\rho^m}{R^{m+1}})\cos m(\theta-\phi), \ R > \rho \\ \\ T^e(R,\theta;\rho,\phi) = -\displaystyle\sum_{m=1}^{\infty}(\frac{R^{m-1}}{\rho^m})\cos m(\theta-\phi), \ \rho > R \end{cases}, \qquad (2\text{-}17)$$

and the higher-order kernel functions, $L(\mathrm{s},\mathrm{x})$ and $M(\mathrm{s},\mathrm{x})$, are shown below

$$L(\mathrm{s},\mathrm{x}) = \begin{cases} L^i(R,\theta;\rho,\phi) = -\displaystyle\sum_{m=1}^{\infty}(\frac{\rho^{m-1}}{R^m})\cos m(\theta-\phi), \ R > \rho \\ \\ L^e(R,\theta;\rho,\phi) = \dfrac{1}{\rho} + \displaystyle\sum_{m=1}^{\infty}(\frac{R^m}{\rho^{m+1}})\cos m(\theta-\phi), \ \rho > R \end{cases}, \qquad (2\text{-}18)$$

$$M(\mathrm{s},\mathrm{x}) = \begin{cases} M^i(R,\theta;\rho,\phi) = \displaystyle\sum_{m=1}^{\infty}(\frac{m\rho^{m-1}}{R^{m+1}})\cos m(\theta-\phi), \ R \geq \rho \\ \\ M^e(R,\theta;\rho,\phi) = \displaystyle\sum_{m=1}^{\infty}(\frac{mR^{m-1}}{\rho^{m+1}})\cos m(\theta-\phi), \ \rho > R \end{cases}. \qquad (2\text{-}19)$$

Since the potentials resulted from $T(\mathrm{s},\mathrm{x})$ and $L(\mathrm{s},\mathrm{x})$ kernels are discontinuous across the boundary, the potentials of $T(\mathrm{s},\mathrm{x})$ and $L(\mathrm{s},\mathrm{x})$ for $R \to \rho^+$ and $R \to \rho^-$

are different. This is the reason why $R = \rho$ is not included for degenerate kernels of $T(\mathrm{s}, \mathrm{x})$ and $L(\mathrm{s}, \mathrm{x})$ in Eqs. (2-17) and (2-18).

Fourier series expansions for unknown boundary densities

For problems with circular boundaries, we apply the Fourier series expansions to approximate the potential φ and its normal derivative ψ on the boundary B_k as

$$\varphi(\mathrm{s}_k) = a_0^k + \sum_{n=1}^{L} (a_n^k \cos n\theta_k + b_n^k \sin n\theta_k), \quad \mathrm{s}_k \in B_k, \quad k = 0, 1, 2, \cdots, N, \qquad (2\text{-}20)$$

$$\psi(\mathrm{s}_k) = p_0^k + \sum_{n=1}^{L} (p_n^k \cos n\theta_k + q_n^k \sin n\theta_k), \quad \mathrm{s}_k \in B_k, \quad k = 0, 1, 2, \cdots, N, \qquad (2\text{-}21)$$

where $\psi(\mathrm{s}_k) = \partial \varphi(\mathrm{s}_k) / \partial \mathrm{n}_\mathrm{s}$, a_n^k, b_n^k, p_n^k and q_n^k ($n = 0, 1, 2, \cdots, L$) are the Fourier coefficients and θ_k is the polar angle. In the real computation, only $2L + 1$ finite terms are considered where L indicates the truncated terms of Fourier series.

2.4 Mathematical formulation and solution procedure

2.4.1 Adaptive observer system

By using the collocation method, the null-field integral equation becomes a set of algebraic equations for the Fourier coefficients. To ensure the stability of algebraic equations, one has to choose collocation points throughout all the circular boundaries of inclusions. Since the boundary integral equation is derived from the reciprocal theorem of energy concept, the boundary integral equation is frame indifferent due to the objectivity rule. This is the reason why the observer system is adaptively to locate the origin at the center of circle in the boundary integration. The adaptive observer system is chosen to fully employ the property of degenerate kernels. Figures 2-4 (a) and 2-4 (b) show the boundary integration for the circular boundary in the adaptive observer system. It is worth noting that the origin of the observer system is located on the center of the corresponding circle under integration to entirely utilize the geometry of circular boundary for the expansion of degenerate kernels and boundary densities. The dummy variable in the circular integration is the angle (θ) instead of the radial coordinate (R).

2.4.2 Linear algebraic equation

By moving the null-field point x_m to the *kth* circular boundary in the limit sense for Eq. (2-13) in Fig. 2-4 (a), we have

$$0 = \sum_{k=0}^{N} \int_{B_k} T(R_k, \theta_k; \rho_m, \phi_m)\varphi(R_k, \theta_k)R_k d\theta_k - \sum_{k=0}^{N} \int_{B_k} U(R_k, \theta_k; \rho_m, \phi_m)\psi(R_k, \theta_k)R_k d\theta_k$$

$$, \mathrm{x}(\rho_m, \phi_m) \in D^c \cup B,$$

(2-22)

where N is the number of circular inclusions and B_0 denotes the outer boundary for the bounded domain. In case of the infinite problem, B_0 becomes B_∞. Note that the kernels $U(\mathrm{s},\mathrm{x})$ and $T(\mathrm{s},\mathrm{x})$ are shown in the degenerate form given by Eqs. (2-16) and (2-17), respectively, while the boundary densities φ and ψ are expressed in terms of the Fourier series expansion forms given by Eqs. (2-20) and (2-21), respectively. Then, the integrals multiplied by separate expansion coefficients in Eq. (2-22) are non-singular and the limit of the null-field point to the boundary is easily implemented by using appropriate forms of degenerate kernels. Through such an idea, all the singular and hypersingular integrals are well captured. Thus, the collocation point $\mathrm{x}(\rho_m, \phi_m)$ in the discretized Eq. (2-22) can be considered on the boundary B_k, as well as the null-field point. Along each circular boundary, $2L+1$ collocation points are required to match $2L+1$ terms of Fourier series for constructing a square influence matrix with the dimension of $2L+1$ by $2L+1$. In contrast to the standard discretized boundary integral equation formulation with nodal unknowns of the physical boundary densities φ and ψ. Now the degrees of freedom are transformed to Fourier coefficients employed in expansion of boundary densities. It is found that the compatible relationship of the boundary unknowns is equivalent by moving either the null-field point or the domain point to the boundary in different directions using various degenerate kernels as shown in Fig. 2-4 (a) and 2-4 (b). Both approaches yield the same linear algebraic equation due to the Wronskian property (see the Appendix in [36]). In the B_k integration, we set the origin of the observer system to collocate at the center c_k to fully utilize the degenerate kernels and Fourier series. By collocating the null-field point on the boundary, the linear algebraic system is obtained

$$[\mathbf{U}]\{\boldsymbol{\psi}\} = [\mathbf{T}]\{\boldsymbol{\varphi}\},$$

(2-23)

where $[\mathbf{U}]$ and $[\mathbf{T}]$ are the influence matrices with a dimension of $(N+1)(2L+1)$ by $(N+1)(2L+1)$, $\{\varphi\}$ and $\{\psi\}$ denote the column vectors of Fourier coefficients with a dimension of $(N+1)(2L+1)$ by 1 in which those are defined as follows:

$$[\mathbf{U}]=\begin{bmatrix} \mathbf{U}_{00} & \mathbf{U}_{01} & \cdots & \mathbf{U}_{0N} \\ \mathbf{U}_{10} & \mathbf{U}_{11} & \cdots & \mathbf{U}_{1N} \\ \vdots & \vdots & \ddots & \vdots \\ \mathbf{U}_{N0} & \mathbf{U}_{N1} & \cdots & \mathbf{U}_{NN} \end{bmatrix}, \quad [\mathbf{T}]=\begin{bmatrix} \mathbf{T}_{00} & \mathbf{T}_{01} & \cdots & \mathbf{T}_{0N} \\ \mathbf{T}_{10} & \mathbf{T}_{11} & \cdots & \mathbf{T}_{1N} \\ \vdots & \vdots & \ddots & \vdots \\ \mathbf{T}_{N0} & \mathbf{T}_{N1} & \cdots & \mathbf{T}_{NN} \end{bmatrix}, \tag{2-24}$$

$$\{\varphi\}=\begin{Bmatrix} \varphi_0 \\ \varphi_1 \\ \varphi_2 \\ \vdots \\ \varphi_N \end{Bmatrix}, \quad \{\psi\}=\begin{Bmatrix} \psi_0 \\ \psi_1 \\ \psi_2 \\ \vdots \\ \psi_N \end{Bmatrix}, \tag{2-25}$$

where $\{\varphi_k\}$ and $\{\psi_k\}$ are in the form of $\{a_0^k \quad a_1^k \quad b_1^k \quad \cdots \quad a_L^k \quad b_L^k\}^T$ and $\{p_0^k \quad p_1^k \quad q_1^k \quad \cdots \quad p_L^k \quad q_L^k\}^T$, respectively; the first subscript "j" ($j=0,1,2,\cdots,N$) in $[\mathbf{U}_{jk}]$ and $[\mathbf{T}_{jk}]$ denotes the index of the jth circle where the collocation point is located and the second subscript "k" ($k=0,1,2,\cdots,N$) denotes the index of the kth circle when integrating on each boundary data $\{\varphi_k\}$ and $\{\psi_k\}$, N is the number of circular inclusions in the domain and the number L indicates the truncated terms of Fourier series. The coefficient matrix of the linear algebraic system is partitioned into blocks, and each off-diagonal block corresponds to the influence matrices between two different circular boundaries. The diagonal blocks are the influence matrices due to themselves in each individual circle. After uniformly collocating the points along the kth circular boundary, the submatrix can be written as

$$[\mathbf{U}_{jk}]=\begin{bmatrix} U_{jk}^{0c}(\phi_1) & U_{jk}^{1c}(\phi_1) & U_{jk}^{1s}(\phi_1) & \cdots & U_{jk}^{Lc}(\phi_1) & U_{jk}^{Ls}(\phi_1) \\ U_{jk}^{0c}(\phi_2) & U_{jk}^{1c}(\phi_2) & U_{jk}^{1s}(\phi_2) & \cdots & U_{jk}^{Lc}(\phi_2) & U_{jk}^{Ls}(\phi_2) \\ U_{jk}^{0c}(\phi_3) & U_{jk}^{1c}(\phi_3) & U_{jk}^{1s}(\phi_3) & \cdots & U_{jk}^{Mc}(\phi_3) & U_{jk}^{Ls}(\phi_3) \\ \vdots & \vdots & \vdots & \ddots & \vdots & \vdots \\ U_{jk}^{0c}(\phi_{2L}) & U_{jk}^{1c}(\phi_{2L}) & U_{jk}^{1s}(\phi_{2L}) & \cdots & U_{jk}^{Lc}(\phi_{2L}) & U_{jk}^{Ls}(\phi_{2L}) \\ U_{jk}^{0c}(\phi_{2L+1}) & U_{jk}^{1c}(\phi_{2L+1}) & U_{jk}^{1s}(\phi_{2L+1}) & \cdots & U_{jk}^{Lc}(\phi_{2L+1}) & U_{jk}^{Ls}(\phi_{2L+1}) \end{bmatrix}, \tag{2-26}$$

$$
\left[\mathbf{T}_{jk}\right] =
\begin{bmatrix}
T_{jk}^{0c}(\phi_1) & T_{jk}^{1c}(\phi_1) & T_{jk}^{1s}(\phi_1) & \cdots & T_{jk}^{Lc}(\phi_1) & T_{jk}^{Ls}(\phi_1) \\
T_{jk}^{0c}(\phi_2) & T_{jk}^{1c}(\phi_2) & T_{jk}^{1s}(\phi_2) & \cdots & T_{jk}^{Lc}(\phi_2) & T_{jk}^{Ls}(\phi_2) \\
T_{jk}^{0c}(\phi_3) & T_{jk}^{1c}(\phi_3) & T_{jk}^{1s}(\phi_3) & \cdots & T_{jk}^{Lc}(\phi_3) & T_{jk}^{Ls}(\phi_3) \\
\vdots & \vdots & \vdots & \ddots & \vdots & \vdots \\
T_{jk}^{0c}(\phi_{2L}) & T_{jk}^{1c}(\phi_{2L}) & T_{jk}^{1s}(\phi_{2L}) & \cdots & T_{jk}^{Lc}(\phi_{2L}) & T_{jk}^{Ls}(\phi_{2L}) \\
T_{jk}^{0c}(\phi_{2L+1}) & T_{jk}^{1c}(\phi_{2L+1}) & T_{jk}^{1s}(\phi_{2L+1}) & \cdots & T_{jk}^{Lc}(\phi_{2L+1}) & T_{jk}^{Ls}(\phi_{2L+1})
\end{bmatrix}, \qquad (2\text{-}27)
$$

where ϕ_m, $m = 1, 2, \cdots, 2L+1$, is the angle of collocation point along the circular boundary. Although both the matrices in Eqs. (2-26) and (2-27) are not sparse, it is found that the higher order harmonics are considered, the lower influence coefficients in numerical experiments are obtained. It is noted that the superscript "$0s$" in Eqs. (2-26) and (2-27) disappears since $\sin n\theta = 0$ ($n = 0$). The element of $\left[\mathbf{U}_{jk}\right]$ and $\left[\mathbf{T}_{jk}\right]$ are defined respectively as

$$
U_{jk}^{nc}(\phi_m) = \int_{B_k} U(\mathbf{s}_k, \mathbf{x}_m) \cos(n\theta_k) R_k d\theta_k ,
$$
$$
n = 0, 1, 2, \cdots, L , \quad m = 1, 2, \cdots, 2L+1 , \tag{2-28}
$$

$$
U_{jk}^{ns}(\phi_m) = \int_{B_k} U(\mathbf{s}_k, \mathbf{x}_m) \sin(n\theta_k) R_k d\theta_k ,
$$
$$
n = 1, 2, \cdots, L , \quad m = 1, 2, \cdots, 2L+1 , \tag{2-29}
$$

$$
T_{jk}^{ns}(\phi_m) = \int_{B_k} T(\mathbf{s}_k, \mathbf{x}_m) \cos(n\theta_k) R_k d\theta_k ,
$$
$$
n = 0, 1, 2, \cdots, L , \quad m = 1, 2, \cdots, 2L+1 , \tag{2-30}
$$

$$
T_{jk}^{ns}(\phi_m) = \int_{B_k} T(\mathbf{s}_k, \mathbf{x}_m) \sin(n\theta_k) R_k d\theta_k ,
$$
$$
n = 1, 2, \cdots, L , \quad m = 1, 2, \cdots, 2L+1 , \tag{2-31}
$$

where k is no sum, $\mathbf{s}_k = (R_k, \theta_k)$, and ϕ_m is the angle of collocation point $\mathbf{x}_m$ along the boundary. The influence coefficient of $U_{jk}^{nc}(\phi_m)$ in Eq. (2-28) denotes the response at $\mathbf{x}_m$ due to the $\cos n\theta$ distribution as shown in Fig. 2-5. Equation (2-22) can be calculated by employing the orthogonal property of trigonometric function in the real computation. Only the finite L terms are used in the summation of Eqs. (2-20) and (2-21). The explicit forms of all the boundary integrals for U, T, L and M kernels are listed in the Table 2-2. Finite values of singular and hypersingular integrals are well captured after introducing the degenerate kernel. Besides, the limiting case across the boundary ($R^- \to \rho \to R^+$) is also addressed. The continuous and jump

behavior across the boundary is well described. After introducing the Wronskian property of two bases ρ^m, ρ^{-m} in Eq. (2-16), the jump behavior across the boundary for the double layer potential T and the normal derivative of singular layer potential L is well captured by

$$\int_0^{2\pi} [T^i - T^e] \cos(n\theta) R d\theta = 2\pi \cos(n\phi), \tag{2-32}$$

$$\int_0^{2\pi} [T^i - T^e] \sin(n\theta) R d\theta = 2\pi \sin(n\phi), \tag{2-33}$$

$$\int_0^{2\pi} [L^i - L^e] \cos(n\theta) R d\theta = -2\pi \cos(n\phi), \tag{2-34}$$

$$\int_0^{2\pi} [L^i - L^e] \sin(n\theta) R d\theta = -2\pi \sin(n\phi). \tag{2-35}$$

The term of 2π depends on the Wronskian of two bases. Reader can consult the 1-D case. Besides, the continuous and pseudo-continuous behavior across the boundary for the singular layer potential U and the normal derivative of double layer potential M is well described as

$$\int_0^{2\pi} [U^i - U^e] \cos(n\theta) R d\theta = 0, \tag{2-36}$$

$$\int_0^{2\pi} [U^i - U^e] \sin(n\theta) R d\theta = 0, \tag{2-37}$$

$$\int_0^{2\pi} [M^i - M^e] \cos(n\theta) R d\theta = 0, \tag{2-38}$$

$$\int_0^{2\pi} [M^i - M^e] \sin(n\theta) R d\theta = 0. \tag{2-39}$$

Instead of using nodal values for boundary densities in the BEM, the Fourier coefficients become the new unknown degrees of freedom in the formulation.

Regarding the circular inclusion problems in the infinite domain, it can be decomposed to one exterior and many interior Laplace problems with circular boundaries after taking free body along the interface of matrix and each inclusion. Two kinds of problems can be formulated in a unified manner as shown in Eq. (2-23) after superimposing remote loadings:

(1) One bounded problem of the circular domain becomes the interior problem for each inclusion as the only boundary B_0 in Fig. 2-4 (a) exists.

(2) The other is unbounded, *i.e.* the outer boundary B_0 in Fig. 2-4 (a) is B_∞. It is the exterior problem for the matrix.

The direction of contour integration should be taken care, *i.e.* counterclockwise and clockwise directions are for the interior and exterior problems, respectively. To match the interface condition between the matrix and each inclusion, additional constraints are provided. Matrix form for the constraints will be elaborated on later in Chapters 3 and Chapter 4. The unknown Fourier coefficients can be determined by the resulted linear algebraic system. Then the potential field is obtained after employing Eq. (2-11). The differences between the present formulation and the conventional BEM are listed in Table 2-3.

2.4.3 Vector decomposition technique for the potential gradient in the hyper-singular equation

In order to determine the field of potential gradient, the normal and tangential derivatives should be calculated with care. Also Eq. (2-12) shows the normal derivative of potential for domain points. For the nonconcentric cases, special treatment for the potential gradient should be considered as the source point and field point locate on different circular boundaries. As shown in Fig. 2-6, the normal direction on the boundary (1, 1') should be superimposed by those of the radial derivative (3, 3') and angular derivative (4, 4') through the vector decomposition technique. According to the concept of vector decomposition technique, the kernel functions of Eqs. (2-18) and (2-19) can be modified to

$$L(\mathrm{s},\mathrm{x})=\begin{cases} L^i(R,\theta;\rho,\phi)=-\displaystyle\sum_{m=1}^{\infty}(\frac{\rho^{m-1}}{R^m})\cos m(\theta-\phi)\cos(\zeta-\xi) \\ \qquad -\displaystyle\sum_{m=1}^{\infty}(\frac{\rho^{m-1}}{R^m})\sin m(\theta-\phi)\cos(\frac{\pi}{2}-\zeta+\xi),\ R>\rho \\ L^e(R,\theta;\rho,\phi)=\dfrac{1}{\rho}+\displaystyle\sum_{m=1}^{\infty}(\frac{R^m}{\rho^{m+1}})\cos m(\theta-\phi)\cos(\zeta-\xi) \\ \qquad -\displaystyle\sum_{m=1}^{\infty}(\frac{R^m}{\rho^{m+1}})\sin m(\theta-\phi)\cos(\frac{\pi}{2}-\zeta+\xi),\ \rho>R \end{cases}, \quad (2\text{-}40)$$

$$
M(\mathrm{s},\mathrm{x}) = \begin{cases} M^{i}(R,\theta;\rho,\phi) = \displaystyle\sum_{m=1}^{\infty}(\frac{m\rho^{m-1}}{R^{m+1}})\cos m(\theta-\phi)\cos(\zeta-\xi) \\ \qquad -\displaystyle\sum_{m=1}^{\infty}(\frac{m\rho^{m-1}}{R^{m+1}})\sin m(\theta-\phi)\cos(\frac{\pi}{2}-\zeta+\xi),\ \ R\geq\rho \\ M^{e}(R,\theta;\rho,\phi) = \displaystyle\sum_{m=1}^{\infty}(\frac{mR^{m-1}}{\rho^{m+1}})\cos m(\theta-\phi)\cos(\zeta-\xi) \\ \qquad -\displaystyle\sum_{m=1}^{\infty}(\frac{mR^{m-1}}{\rho^{m+1}})\sin m(\theta-\phi)\cos(\frac{\pi}{2}-\zeta+\xi),\ \ \rho>R \end{cases}, \quad (2\text{-}41)
$$

where ζ and ξ are shown in Fig. 2-6. For the special case of confocal, the potential gradient is derived free of special treatment since $\zeta=\xi$.
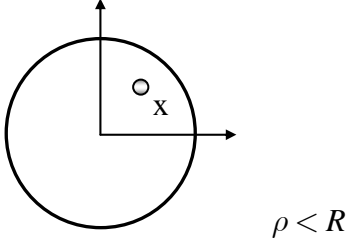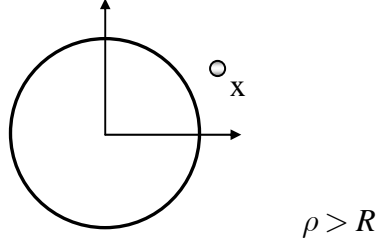
2.5 Concluding remarks

For boundary value problems with circular boundaries, the null-field approach by using the null-field integral equation, degenerate kernels and Fourier series in the adaptive observer system was proposed. The singularity and hypersingularity were avoided after introducing the concept of degenerate kernels for interior and exterior regions. Besides, the boundary-layer effect for the potential gradient calculation is expected to be eliminated since the degenerate kernel can describe the jump behavior for interior and exterior domains, respectively. The generality and versatility for the problems with multiple circular inclusions of arbitrary radii, positions and properties will be examined in the following chapters. Both the efficiency and accuracy will be investigated. Moreover, the presented method here can be applied to Laplace problems with circular boundaries, *e.g.* piezoelectricity, electrostatic, magnetic, torsion, elasticity, heat conduction and hydrodynamic problems. Besides, extensions to the Helmholtz, biharmonic and biHelmholtz operators as well as 3-D problems are straightforward once the corresponding degenerate kernels and bases for boundary densities can be found. In this thesis, our main concern is only the Laplace problem.
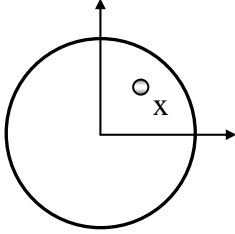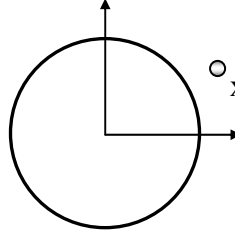
Table 2-1 Comparison of formulation between the present approach and conventional BEM for simply-connected domain problems

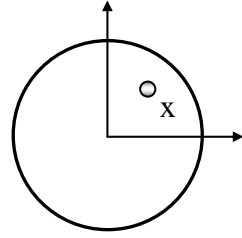| Conventional BEM	Present formulation
Primary field (essential formulation)	
$2\pi\varphi(\mathrm{x}) = \int_B T(\mathrm{s},\mathrm{x})\varphi(\mathrm{s})dB(\mathrm{s}) - \int_B U(\mathrm{s},\mathrm{x})\psi(\mathrm{s})dB(\mathrm{s}),\ \mathrm{x} \in D$	$2\pi\varphi(\mathrm{x}) = \int_B T^i(\mathrm{s},\mathrm{x})\varphi(\mathrm{s})dB(\mathrm{s}) - \int_B U^i(\mathrm{s},\mathrm{x})\psi(\mathrm{s})dB(\mathrm{s}),\ \mathrm{x} \in D \cup B$
$\pi\varphi(\mathrm{x}) = C.P.V.\int_B T(\mathrm{s},\mathrm{x})\varphi(\mathrm{s})dB(\mathrm{s}) - R.P.V.\int_B U(\mathrm{s},\mathrm{x})\psi(\mathrm{s})dB(\mathrm{s}),\ \mathrm{x} \in B$	$0 = \int_B T^e(\mathrm{s},\mathrm{x})\varphi(\mathrm{s})dB(\mathrm{s}) - \int_B U^e(\mathrm{s},\mathrm{x})\psi(\mathrm{s})dB(\mathrm{s}),\ \mathrm{x} \in D^c \cup B$
$0 = \int_B T(\mathrm{s},\mathrm{x})\varphi(\mathrm{s})dB(\mathrm{s}) - \int_B U(\mathrm{s},\mathrm{x})\psi(\mathrm{s})dB(\mathrm{s}),\ \mathrm{x} \in D^c$	
Secondary field (natural formulation)	
$2\pi\dfrac{\partial\varphi(\mathrm{x})}{\partial\,\mathrm{n_x}} = \int_B M(\mathrm{s},\mathrm{x})\varphi(\mathrm{s})dB(\mathrm{s}) - \int_B L(\mathrm{s},\mathrm{x})\psi(\mathrm{s})dB(\mathrm{s}),\ \mathrm{x} \in D$	$2\pi\dfrac{\partial\varphi(\mathrm{x})}{\partial\,\mathrm{n_x}} = \int_B M^i(\mathrm{s},\mathrm{x})\varphi(\mathrm{s})dB(\mathrm{s}) - \int_B L^i(\mathrm{s},\mathrm{x})\psi(\mathrm{s})dB(\mathrm{s}),\ \mathrm{x} \in D \cup B$
$\pi\dfrac{\partial\varphi(\mathrm{x})}{\partial\,\mathrm{n_x}} = H.P.V.\int_B M(\mathrm{s},\mathrm{x})\varphi(\mathrm{s})dB(\mathrm{s}) - C.P.V.\int_B L(\mathrm{s},\mathrm{x})\psi(\mathrm{s})dB(\mathrm{s}),\ \mathrm{x} \in B$	$0 = \int_B M^e(\mathrm{s},\mathrm{x})\varphi(\mathrm{s})dB(\mathrm{s}) - \int_B L^e(\mathrm{s},\mathrm{x})\psi(\mathrm{s})dB(\mathrm{s}),\ \mathrm{x} \in D^c \cup B$
$0 = \int_B M(\mathrm{s},\mathrm{x})\varphi(\mathrm{s})dB(\mathrm{s}) - \int_B L(\mathrm{s},\mathrm{x})\psi(\mathrm{s})dB(\mathrm{s}),\ \mathrm{x} \in D^c$	

Table 2-2 Influence coefficients for the singularity distribution on the circular boundary

$\rho < R$

$\rho > R$

| $U(s,x)$ | Degenerate kernel | $U^i(R,\theta;\rho,\phi) = \ln R - \sum_{m=1}^{\infty} \frac{1}{m}(\frac{\rho}{R})^m \cos m(\theta-\phi),\ R \geq \rho$ | $U^e(R,\theta;\rho,\phi) = \ln \rho - \sum_{m=1}^{\infty} \frac{1}{m}(\frac{R}{\rho})^m \cos m(\theta-\phi),\ \rho > R$ |

$U(s,x)$ — Orthogonal process

$$\int_0^{2\pi} [U^i][1]Rd\theta = 2\pi \ln R,\ R \geq \rho$$

$$\int_0^{2\pi} [U^i][\cos n\theta]Rd\theta = \pi \frac{1}{n}\frac{\rho^n}{R^{n-1}}\cos n\phi,\ R \geq \rho$$

$$\int_0^{2\pi} [U^i][\sin n\theta]Rd\theta = \pi \frac{1}{n}\frac{\rho^n}{R^{n-1}}\sin n\phi,\ R \geq \rho$$

$$\int_0^{2\pi} [U^e][1]Rd\theta = 2\pi \ln \rho,\ \rho > R$$

$$\int_0^{2\pi} [U^e][\cos n\theta]Rd\theta = \pi \frac{1}{n}\frac{R^{n+1}}{\rho^n}\cos n\phi,\ \rho > R$$

$$\int_0^{2\pi} [U^e][\sin n\theta]Rd\theta = \pi \frac{1}{n}\frac{R^{n+1}}{\rho^n}\sin n\phi,\ \rho > R$$

Limiting behavior across the boundary

$$\lim_{\rho \to R} 2\pi \ln R = 2\pi \ln R$$

$$\lim_{\rho \to R} \pi \frac{1}{n}\frac{\rho^n}{R^{n-1}}\cos n\phi = \pi \frac{1}{n} R \cos n\phi$$

$$\lim_{\rho \to R} \pi \frac{1}{n}\frac{\rho^n}{R^{n-1}}\sin n\phi = \pi \frac{1}{n} R \sin n\phi$$

Continuous

$(R^- \to R \to R^+)$

$$\lim_{\rho \to R} 2\pi \ln \rho = 2\pi \ln R$$

$$\lim_{\rho \to R} \pi \frac{1}{n}\frac{R^{n+1}}{\rho^n}\cos n\phi = \pi \frac{1}{n} R \cos n\phi$$

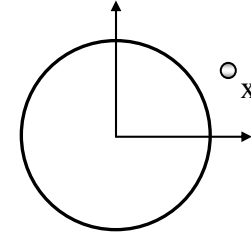$$\lim_{\rho \to R} \pi \frac{1}{n}\frac{R^{n+1}}{\rho^n}\sin n\phi = \pi \frac{1}{n} R \sin n\phi$$

		$\rho < R$	$\rho > R$
$T(s,x)$	Degenerate kernel	$T^i(R,\theta;\rho,\phi) = \dfrac{1}{R} + \sum\limits_{m=1}^{\infty}(\dfrac{\rho^m}{R^{m+1}})\cos m(\theta-\phi),\ R > \rho$	$T^e(R,\theta;\rho,\phi) = -\sum\limits_{m=1}^{\infty}(\dfrac{R^{m-1}}{\rho^m})\cos m(\theta-\phi),\ \rho > R$
	Orthogonal process	$\displaystyle\int_0^{2\pi}[T^i][1]Rd\theta = \dfrac{2\pi}{R},\ R > \rho$ $\displaystyle\int_0^{2\pi}[T^i][\cos n\theta]Rd\theta = \pi(\dfrac{\rho}{R})^n\cos n\phi,\ R > \rho$ $\displaystyle\int_0^{2\pi}[T^i][\sin n\theta]Rd\theta = \pi(\dfrac{\rho}{R})^n\sin n\phi,\ R > \rho$	$\displaystyle\int_0^{2\pi}[T^e][1]Rd\theta = 0,\ \rho > R$ $\displaystyle\int_0^{2\pi}[T^e][\cos n\theta]Rd\theta = -\pi(\dfrac{R}{\rho})^n\cos n\phi,\ \rho > R$ $\displaystyle\int_0^{2\pi}[T^e][\sin n\theta]Rd\theta = -\pi(\dfrac{R}{\rho})^n\sin n\phi,\ \rho > R$
	Limiting behavior across the boundary	$\lim\limits_{\rho\to R}\dfrac{2\pi}{R} = \dfrac{2\pi}{R}$ $\lim\limits_{\rho\to R}\pi(\dfrac{\rho}{R})^n\cos n\phi = \pi\cos n\phi$ $\lim\limits_{\rho\to R}\pi(\dfrac{\rho}{R})^n\sin n\phi = \pi\sin n\phi$ Jump $(R^- \to R \to R^+)$	$\lim\limits_{\rho\to R}0 = 0$ $\lim\limits_{\rho\to R}-\pi(\dfrac{R}{\rho})^n\cos n\phi = -\pi\cos n\phi$ $\lim\limits_{\rho\to R}-\pi(\dfrac{R}{\rho})^n\sin n\phi = -\pi\sin n\phi$

$$\rho < R \qquad\qquad \rho > R$$

$L(s,x)$	Degenerate kernel	$L^i(R,\theta;\rho,\phi) = -\sum_{m=1}^{\infty}(\dfrac{\rho^{m-1}}{R^m})\cos m(\theta-\phi),\ R>\rho$	$L^e(R,\theta;\rho,\phi) = \dfrac{1}{\rho} + \sum_{m=1}^{\infty}(\dfrac{R^m}{\rho^{m+1}})\cos m(\theta-\phi),\ \rho>R$
	Orthogonal process	$\displaystyle\int_0^{2\pi}[L^i][1]Rd\theta = 0,\ R>\rho$ $\displaystyle\int_0^{2\pi}[L^i][\cos n\theta]Rd\theta = -\pi(\dfrac{\rho}{R})^{n-1}\cos n\phi,\ R>\rho$ $\displaystyle\int_0^{2\pi}[L^i][\sin n\theta]Rd\theta = -\pi(\dfrac{\rho}{R})^{n-1}\sin n\phi,\ R>\rho$	$\displaystyle\int_0^{2\pi}[L^e][1]Rd\theta = \dfrac{2\pi}{\rho},\ \rho>R$ $\displaystyle\int_0^{2\pi}[L^e][\cos n\theta]Rd\theta = \pi(\dfrac{R}{\rho})^{n+1}\cos n\phi,\ \rho>R$ $\displaystyle\int_0^{2\pi}[L^e][\sin n\theta]Rd\theta = \pi(\dfrac{R}{\rho})^{n+1}\sin n\phi,\ \rho>R$
	Limiting behavior across the boundary	$\displaystyle\lim_{\rho\to R} 0 = 0$ $\displaystyle\lim_{\rho\to R} -\pi(\dfrac{\rho}{R})^{n-1}\cos n\phi = -\pi\cos n\phi$ $\displaystyle\lim_{\rho\to R} -\pi(\dfrac{\rho}{R})^{n-1}\sin n\phi = -\pi\sin n\phi$ Jump $(R^- \to R \to R^+)$	$\displaystyle\lim_{\rho\to R}\dfrac{2\pi}{\rho} = \dfrac{2\pi}{R}$ $\displaystyle\lim_{\rho\to R}\pi(\dfrac{R}{\rho})^{n+1}\cos n\phi = \pi\cos n\phi$ $\displaystyle\lim_{\rho\to R}\pi(\dfrac{R}{\rho})^{n+1}\sin n\phi = \pi\sin n\phi$
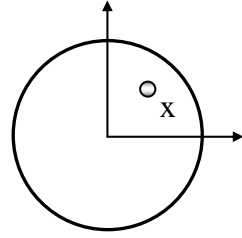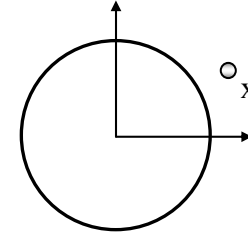
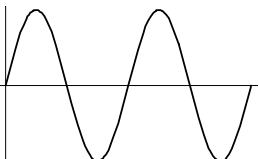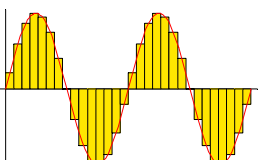|		$\rho < R$	$\rho > R$
$M(s,x)$	Degenerate kernel	$M^i(R,\theta;\rho,\phi)=\sum_{m=1}^{\infty}(\dfrac{m\rho^{m-1}}{R^{m+1}})\cos m(\theta-\phi),\ R\geq\rho$	$M^e(R,\theta;\rho,\phi)=\sum_{m=1}^{\infty}(\dfrac{mR^{m-1}}{\rho^{m+1}})\cos m(\theta-\phi),\ \rho>R$
	Orthogonal process	$\int_0^{2\pi}[M^i][1]Rd\theta=0,\ R\geq\rho$ $\int_0^{2\pi}[M^i][\cos n\theta]Rd\theta=n\pi\dfrac{\rho^{n-1}}{R^n}\cos n\phi,\ R\geq\rho$ $\int_0^{2\pi}[M^i][\sin n\theta]Rd\theta=n\pi\dfrac{\rho^{n-1}}{R^n}\sin n\phi,\ R\geq\rho$	$\int_0^{2\pi}[M^e][1]Rd\theta=0,\ \rho>R$ $\int_0^{2\pi}[M^e][\cos n\theta]Rd\theta=n\pi\dfrac{R^n}{\rho^{n+1}}\cos n\phi,\ \rho>R$ $\int_0^{2\pi}[M^e][\sin n\theta]Rd\theta=n\pi\dfrac{R^n}{\rho^{n+1}}\sin n\phi,\ \rho>R$
	Limiting behavior across the boundary	$\lim_{\rho\to R}0=0$ $\lim_{\rho\to R}n\pi\dfrac{\rho^{n-1}}{R^n}\cos n\phi=n\pi\dfrac{1}{R}\cos n\phi$ $\lim_{\rho\to R}n\pi\dfrac{\rho^{n-1}}{R^n}\sin n\phi=n\pi\dfrac{1}{R}\sin n\phi$	$\lim_{\rho\to R}0=0$ $\lim_{\rho\to R}n\pi\dfrac{R^n}{\rho^{n+1}}\cos n\phi=n\pi\dfrac{1}{R}\cos n\phi$ $\lim_{\rho\to R}n\pi\dfrac{R^n}{\rho^{n+1}}\sin n\phi=n\pi\dfrac{1}{R}\sin n\phi$

Pseudo-continuous $(R^-\to R\to R^+)$

Table 2-3 Comparisons of the present method and the conventional BEM

	Boundary density discretization	Auxiliary system	Formulation	Observer system	Singularity	Convergence	Boundary-layer effect
Present method	Fourier series	Degenerate kernel	Null-field integral equation	Adaptive observer system	Disappear after introducing the degenerate kernel	Exponential convergence	Eliminate
Conventional BEM	Constant element	Fundamental solution	Boundary integral equation	Fixed observer system	Principal values ($C.P.V.$, $R.P.V.$ and $H.P.V.$)	Linear algebraic convergence	Appear

where $C.P.V.$, $R.P.V.$ and $H.P.V.$ are the Cauchy, Riemann and Hadamard principal values, respectively.
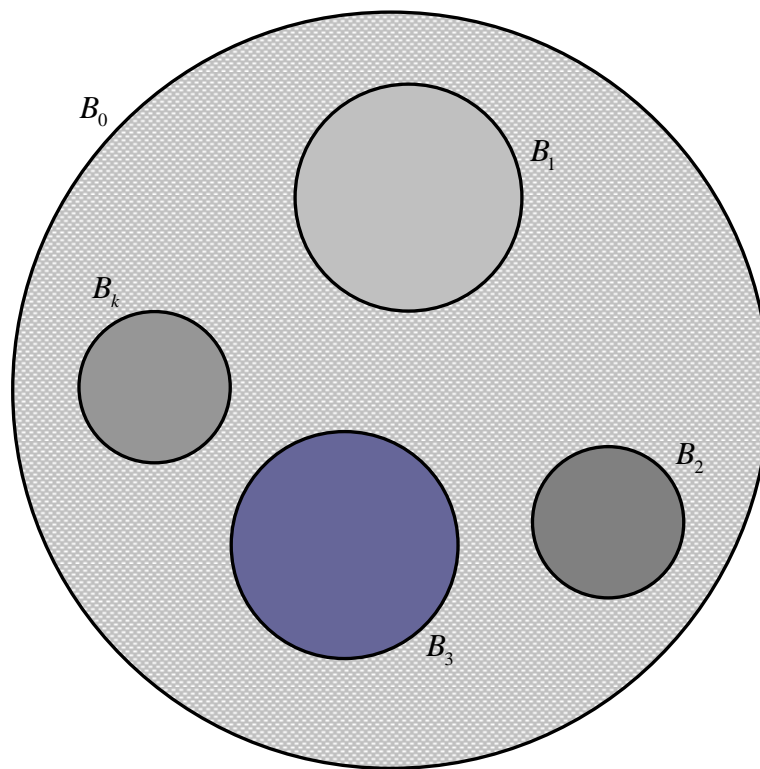
Figure 2-1 Randomly distributed circular inclusions bounded to the contour B_k
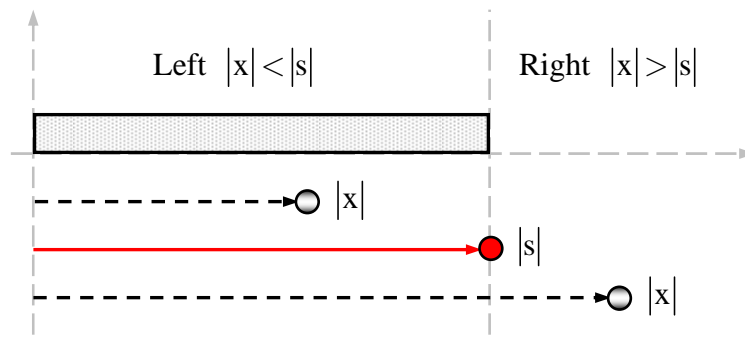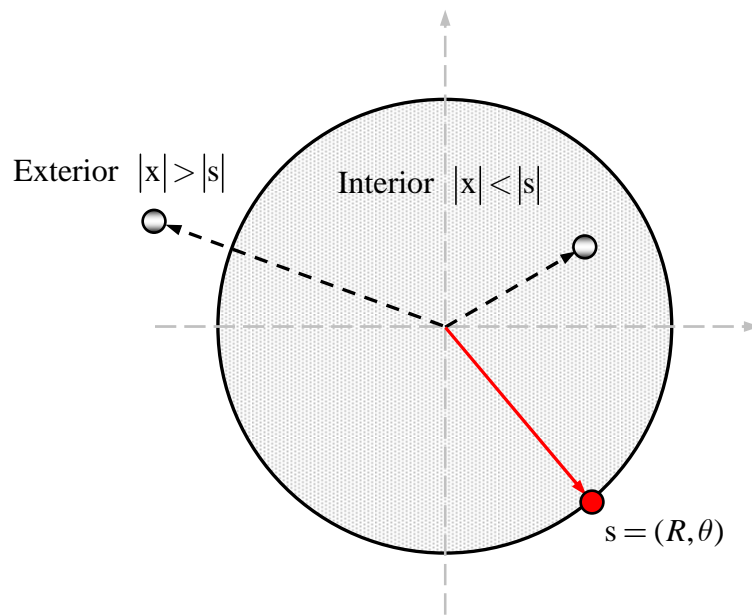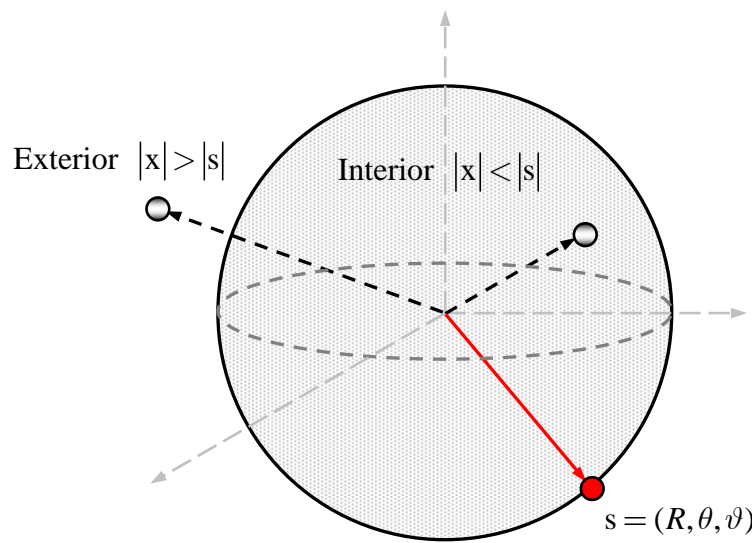
Figure 2-2 Degenerate kernels for one, two and three dimensional problems
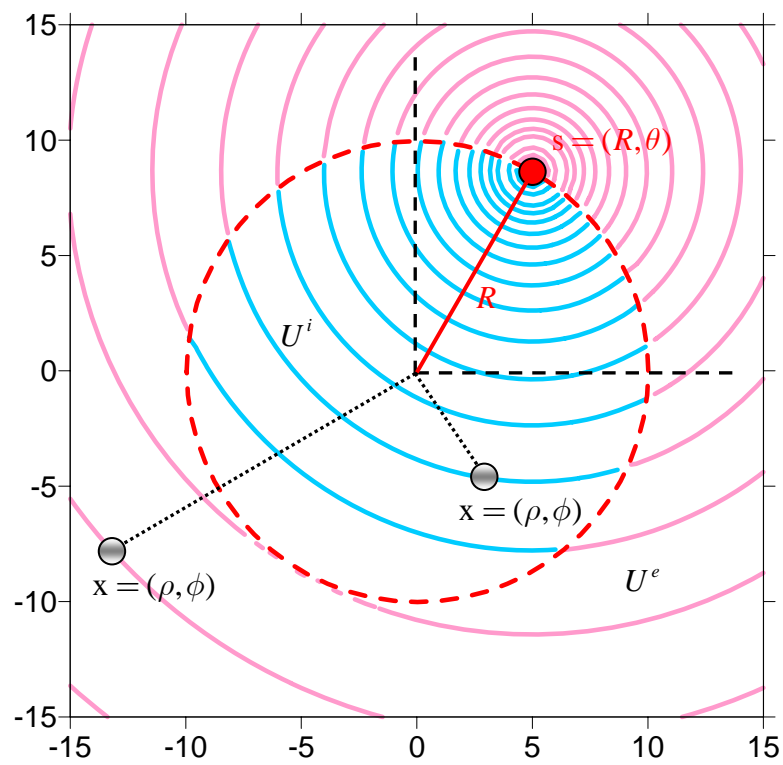
Figure 2-3 Graph of the degenerate kernel for the fundamental solution
$s = (10, \pi/3)$
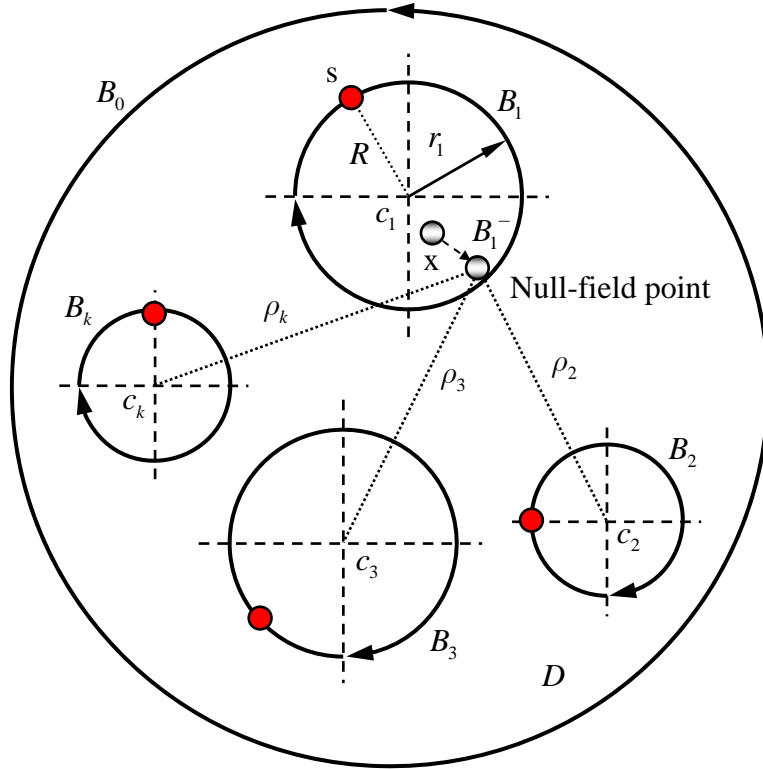
Figure 2-4 (a) Sketch of the null-field integral equation for a null-field point in conjunction with the adaptive observer system ($x \notin D$, $x \to B_k$)
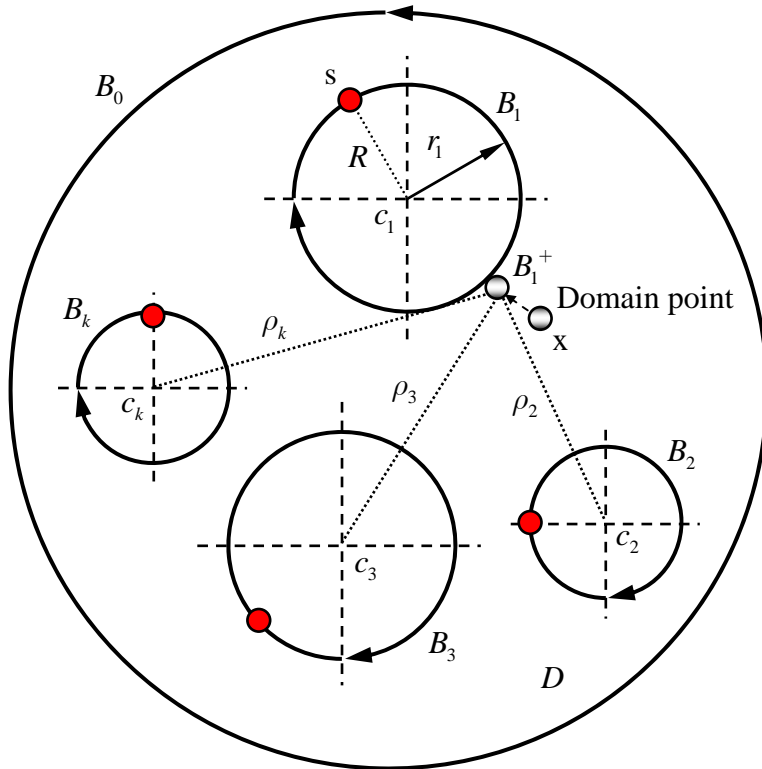
Figure 2-4 (b) Sketch of the boundary integral equation for a domain point in conjunction with the adaptive observer system ($x \in D$, $x \to B_k$)
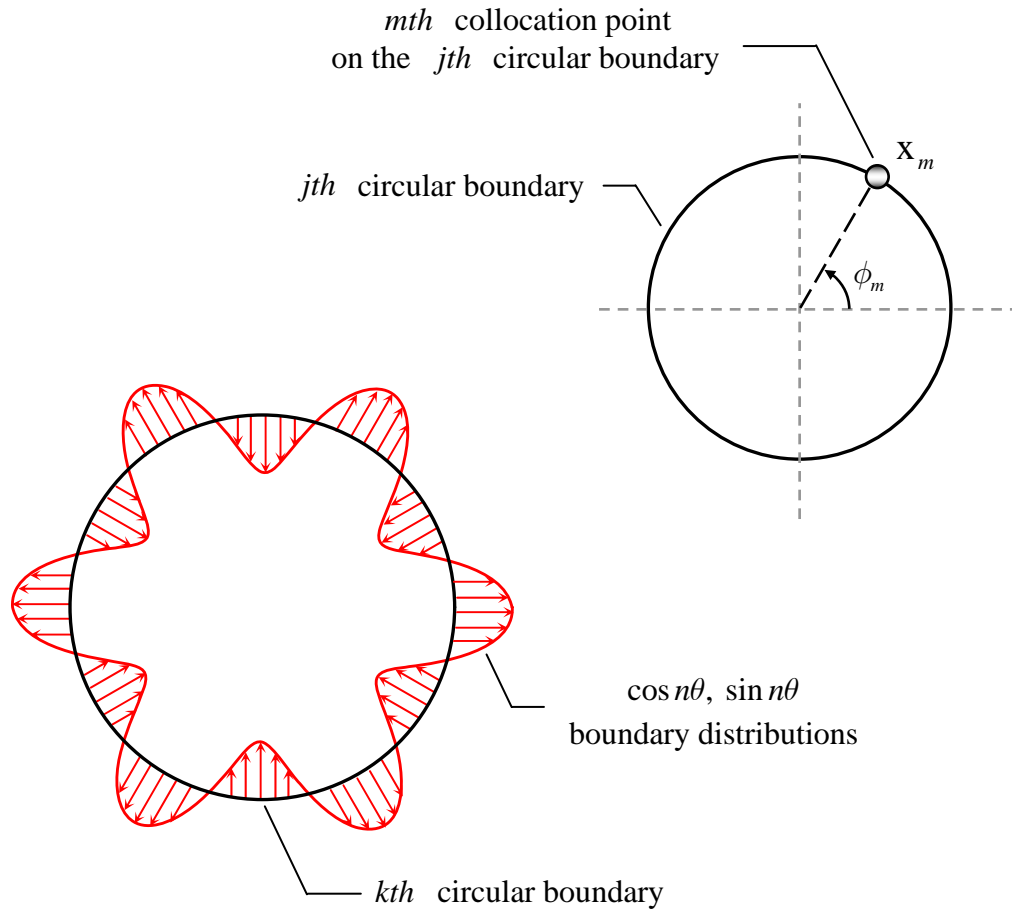
Figure 2-5 Physical meaning of influence coefficients $U_{jk}^{nc}(\phi_m)$, $U_{jk}^{ns}(\phi_m)$: the responses for the x_m point of the jth boundary due to the $\cos n\theta$, $\sin n\theta$ boundary distributions of the kth circular boundary
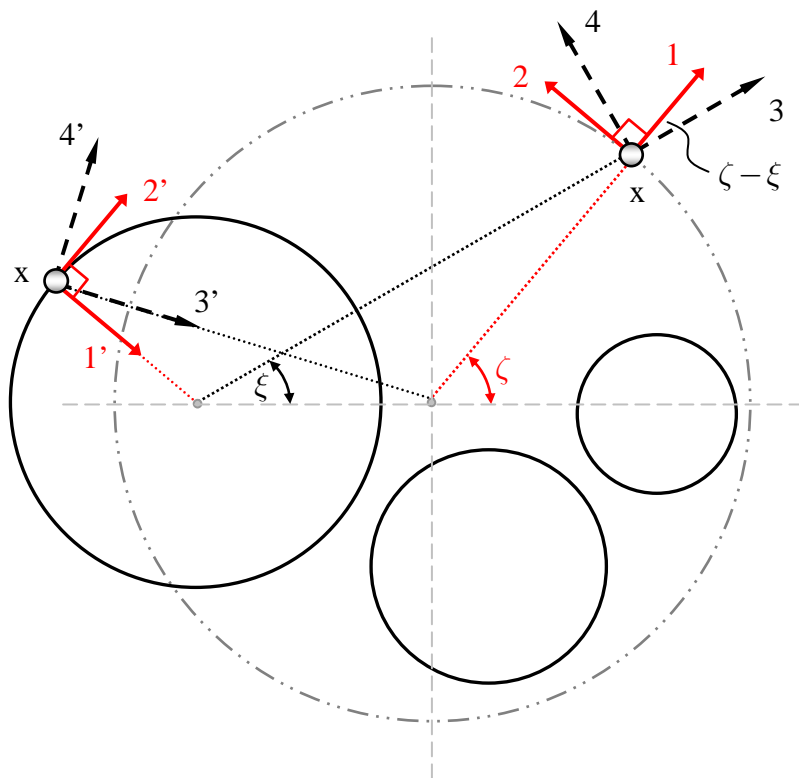
Figure 2-6 Vector decomposition for the potential gradient in the hypersingular equation

Chapter 3 Applications to anti-plane piezoelectricity and in-plane electrostatic problems with circular inclusions

Summary

In this chapter, piezoelectricity problems with arbitrary number of circular inclusions under remote anti-plane shears and in-plane electric fields are studied. Piezoelectric problems with two piezoelectric circular inclusions are revisited and compared with the solutions by previous researchers to demonstrate the validity of our method. The limiting case shows that the two inclusions separating far away leads to the Pak's exact solution of a single inclusion. Stress and electric field concentrations are calculated and are dependent on the distance between the two inclusions, the mismatch in the material constants and the magnitude of mechanical and electromechanical loadings. Besides, the uncoupling case for in-plane electrostatic problems in electric fields is also addressed.

3.1 Introduction

The recent technological developments and the increasing market demand have opened promising research opportunities and engineering priorities in the field of micromechanics. Coupled electro-elastic analysis in smart composites and micro-electro-mechanical systems (MEMS) receives much attention. Due to the intrinsic coupling effect of electrical and mechanical fields, the piezoelectric material is widely applied to intelligent structures. Regarding the piezoelectric circular inclusions, an exact solution of a single piezoelectric inclusion was derived by Pak [74] under remote anti-plane shear and in-plane electric loadings. For the two piezoelectric inclusions, Honein *et al.* [58] employed the Möbius transformation to derive the electromechanical field. Based upon the complex variable theory and the method of successive approximations, Chao and Chang [20] revisited the problem of two piezoelectric inclusions in terms of explicit series form. Wu and Funami [95] also solved this problem by using the conformal mapping and the theorem of analytical

continuation. Wang and Shen [88] considered the shear and electric loadings in two directions. In addition, Chen and Chiang [41] employed conformal mapping techniques to analyze this kind of boundary value problems and specific results were given for elliptical, polygonal and star-shape inclusions. For the decoupling problems, Emets and Onofrichuk [46] presented an analytic solution for two dielectric cylinders in electric fields.

This chapter aims the first attempt to employ the null-field formulation to solve piezoelectricity problems with multiple circular inclusions. By introducing a multi-domain approach, an inclusion problem can be decomposed into two parts. One is the piezoelectric infinite medium with circular holes and the other is the problem with each piezoelectric circular inclusion. After considering the continuity and equilibrium conditions on the interface for electrical and mechanical fields, a linear algebraic system can be obtained and the unknown Fourier coefficients in the algebraic system can be determined. Then the displacement field and electric potential are obtained. Furthermore, an arbitrary number of piezoelectric circular inclusions are treated by using the present method without any difficulty. The calculation of potential gradient must be determined with care by using the vector decomposition and the adaptive observer system for the nonconfocal case. Also the boundary stress and electric fields can be easily determined by using series sums instead of employing the sense of Hadamard principal value. A general-purpose program for arbitrary number of piezoelectric circular inclusions with various radii, arbitrary positions and different material constants was developed. Several examples solved previously by other researchers [20, 46, 74, 88, 95] were revisited to see the accuracy and efficiency of the present formulation. The Pak's solution of a single inclusion is designed as a limiting case when two inclusions dispart far away.

3.2 Problem statements and mathematical formulation

The physical problem to be considered is shown in Fig. 3-1, where multiple piezoelectric circular inclusions are imbedded in an infinite piezoelectric medium under the far-field antiplane shear σ_{zx}^{∞}, σ_{zy}^{∞} and the far-field inplane electric field E_x^{∞}, E_y^{∞}. Bleustein [13] has found that if one takes the plane normal to the poling direction as the

plane of interest, only the anti-plane displacement w couples with the in-plane electric field E_r and E_θ. Therefore, we only consider the anti-plane displacement and the in-plane electric field such that

$$u = v = 0, \quad w = w(r,\theta); \quad E_r = E_r(r,\theta), \quad E_\theta = E_\theta(r,\theta), \quad E_z = 0, \tag{3-1}$$

where u, v and E_z are the vanishing components of displacements and electric field, respectively. The governing equation for anti-plane elasticity w and in-plane electrostatics Φ, in the absence of body forces and body charges, can be decoupled and simplified to

$$\nabla^2 w = 0, \quad \nabla^2 \Phi = 0, \tag{3-2}$$

where ∇^2 is the two-dimensional Laplacian operator

$$\nabla^2 \equiv \frac{\partial}{\partial r^2} + \frac{1}{r}\frac{\partial}{\partial r} + \frac{1}{r^2}\frac{\partial}{\partial \theta^2}, \tag{3-3}$$

and Φ is the in-plane electric potential. The coupling between the elastic field and the electrical field occurs only through the constitutive equations

$$\sigma_{zr} = c_{44}\gamma_{zr} - e_{15}E_r, \quad \sigma_{z\theta} = c_{44}\gamma_{z\theta} - e_{15}E_\theta, \tag{3-4}$$

$$D_r = e_{15}\gamma_{zr} + \varepsilon_{11}E_r, \quad D_\theta = e_{15}\gamma_{z\theta} + \varepsilon_{11}E_\theta, \tag{3-5}$$

where c_{44} is the elastic modulus, e_{15} is the piezoelectric constant, ε_{11} is the dielectric constant, σ_{ij} and D_i are respectively the anti-plane shear stress and in-plane electric displacement, γ_{ij} and E_i are respectively the anti-plane shear strain and in-plane electric field, which are defined as

$$\gamma_{zr} = \frac{\partial w}{\partial r}, \quad \gamma_{z\theta} = \frac{1}{r}\frac{\partial w}{\partial \theta}, \quad E_r = -\frac{\partial \Phi}{\partial r}, \quad E_\theta = -\frac{1}{r}\frac{\partial \Phi}{\partial \theta}. \tag{3-6}$$

The analogy between the anti-plane shear deformation and in-plane electrostatics for anti-plane piezoelectric problems is listed in Table 3-1. For the stress fields σ_{zx}, σ_{zy} and electric displacement fields D_x, D_y, they are found in Table 3-1 or can be superimposed by σ_{zr}, $\sigma_{z\theta}$ in Eq. (3-4) and D_r, D_θ in Eq. (3-5) as

$$\sigma_{zx} = \sigma_{zr}\cos\phi - \sigma_{z\theta}\sin\phi, \tag{3-7}$$

$$\sigma_{zy} = \sigma_{zr}\sin\phi + \sigma_{z\theta}\cos\phi, \tag{3-8}$$

$$D_x = D_r\cos\phi - D_\theta\sin\phi, \tag{3-9}$$

$$D_y = D_r\sin\phi + D_\theta\cos\phi. \tag{3-10}$$

By taking free body along the interface between the matrix and inclusions, the problem can be decomposed into two systems. One is an infinite medium with N circular holes under remote anti-plane shear and in-plane electric loadings as shown in Fig. 3-2 (a). The other is N circular inclusions bounded by the B_k contour which satisfies the Laplace equation as shown in Fig. 3-2 (b). From the numerical point of view, this is the so-called multi-domain approach. For the problem in Fig. 3-2 (a), it can be superimposed by two parts. One is an infinite medium under remote shear and electric loadings and the other is an infinite medium with N circular holes which satisfies the Laplace equation as shown in Figs. 3-2 (c) and 3-2 (d), respectively. Therefore, one exterior problem for the matrix is shown in Fig. 3-2 (d) and several interior problems for nonoverlapping inclusions are shown in Fig. 3-2 (b). The two problems in Figs. 3-2 (d) and 3-2 (b) can be solved in a unified manner by the null-field integral formulation since they both satisfy the Laplace equation.

When the coupled effect between the mechanical and electrical fields is absent or the piezoelectric constant are equal to zero, the expressions of the electro-elastic field in the present formulation reduces to the results given by Emets and Onofrichuk [46] and Honein *et al.* [56], respectively.

3.3 Matching of interface conditions and solution procedures

In the present application, both anti-plane mechanical and in-plane electrical fields are modeled by using the null-field formulation. Since both the displacement field w and the electric potential Φ satisfy the Laplace equation, the variables φ and $\psi(\mathrm{s}) = \partial \varphi(\mathrm{s}) / \partial \mathrm{n}_\mathrm{s}$ formulated in Chapter 2, can be replaced by w, $t(\mathrm{s}) = \partial w(\mathrm{s}) / \partial \mathrm{n}_\mathrm{s}$ for anti-plane elasticity and Φ, $\Psi(\mathrm{s}) = \partial \Phi(\mathrm{s}) / \partial \mathrm{n}_\mathrm{s}$ for in-plane electrostatics, respectively. By collocating the null-field point on the boundary, the linear algebraic system is obtained from Eq. (2-22):

For the exterior problem of matrix in Fig. 3-2 (d), we have

$$\left[\mathbf{U}^M\right]\left\{\mathbf{t}^M - \mathbf{t}^\infty\right\} = \left[\mathbf{T}^M\right]\left\{\mathbf{w}^M - \mathbf{w}^\infty\right\}, \tag{3-11}$$

$$\left[\mathbf{U}^M\right]\left\{\boldsymbol{\Psi}^M - \boldsymbol{\Psi}^\infty\right\} = \left[\mathbf{T}^M\right]\left\{\boldsymbol{\Phi}^M - \boldsymbol{\Phi}^\infty\right\}. \tag{3-12}$$

For the interior problem of each inclusion in Fig. 3-2 (b), we have

$$\left[\mathbf{U}^I\right]\left\{\mathbf{t}^I\right\} = \left[\mathbf{T}^I\right]\left\{\mathbf{w}^I\right\}, \tag{3-13}$$

$$\left[\mathbf{U}^I\right]\left\{\boldsymbol{\Psi}^I\right\} = \left[\mathbf{T}^I\right]\left\{\boldsymbol{\Phi}^I\right\}, \tag{3-14}$$

where the superscripts "M" and "I" denote the matrix and inclusion, respectively. The matrix due to degenerate kernels $\left[\mathbf{U}^M\right]$, $\left[\mathbf{T}^M\right]$, $\left[\mathbf{U}^I\right]$ and $\left[\mathbf{T}^I\right]$ and vectors for Fourier series $\left\{\mathbf{w}^M\right\}$, $\left\{\mathbf{t}^M\right\}$, $\left\{\mathbf{w}^\infty\right\}$, $\left\{\mathbf{t}^\infty\right\}$, $\left\{\boldsymbol{\Phi}^M\right\}$, $\left\{\boldsymbol{\Psi}^M\right\}$, $\left\{\boldsymbol{\Phi}^\infty\right\}$, $\left\{\boldsymbol{\Psi}^\infty\right\}$, $\left\{\mathbf{w}^I\right\}$, $\left\{\mathbf{t}^I\right\}$, $\left\{\boldsymbol{\Phi}^I\right\}$ and $\left\{\boldsymbol{\Psi}^I\right\}$ employed in the null-field equation can be found in Chapter 2. It is noted that $\left\{\mathbf{w}^\infty\right\}$, $\left\{\mathbf{t}^\infty\right\}$, $\left\{\boldsymbol{\Phi}^\infty\right\}$ and $\left\{\boldsymbol{\Psi}^\infty\right\}$ in Fig. 3-2 (c) are the displacement and traction fields due to the remote shear and electric loadings, respectively.

According to the continuity of displacement and equilibrium of traction along the kth interface, we have the four compatible relationships for boundary data on the interface. For the stress field, the interface condition yields

$$w^M = w^I \quad \text{on} \quad B_k, \tag{3-15}$$

$$\sigma_{zr}^M = \sigma_{zr}^I \quad \text{on} \quad B_k. \tag{3-16}$$

For the electric field, the interface condition gives

$$\Phi^M = \Phi^I \quad \text{on} \quad B_k, \tag{3-17}$$

$$D_r^M = D_r^I \quad \text{on} \quad B_k. \tag{3-18}$$

Invoking the governing equation of piezoelectricity with proper continuity conditions, fully coupled equations are obtained. By assembling the matrices in Eqs. (3-11) ~(3-14) and (3-15) ~(3-18), we have

$$
\begin{bmatrix}
\mathbf{T}^M & -\mathbf{U}^M & \mathbf{0} & \mathbf{0} & \mathbf{0} & \mathbf{0} & \mathbf{0} & \mathbf{0} \\
\mathbf{0} & \mathbf{0} & \mathbf{T}^I & -\mathbf{U}^I & \mathbf{0} & \mathbf{0} & \mathbf{0} & \mathbf{0} \\
\mathbf{0} & \mathbf{0} & \mathbf{0} & \mathbf{0} & \mathbf{T}^M & -\mathbf{U}^M & \mathbf{0} & \mathbf{0} \\
\mathbf{0} & \mathbf{0} & \mathbf{0} & \mathbf{0} & \mathbf{0} & \mathbf{0} & \mathbf{T}^I & -\mathbf{U}^I \\
\mathbf{I} & \mathbf{0} & -\mathbf{I} & \mathbf{0} & \mathbf{0} & \mathbf{0} & \mathbf{0} & \mathbf{0} \\
\mathbf{0} & \mathbf{c}_{44}^M & \mathbf{0} & \mathbf{c}_{44}^I & \mathbf{0} & \mathbf{e}_{15}^M & \mathbf{0} & \mathbf{e}_{15}^I \\
\mathbf{0} & \mathbf{0} & \mathbf{0} & \mathbf{0} & \mathbf{I} & \mathbf{0} & -\mathbf{I} & \mathbf{0} \\
\mathbf{0} & \mathbf{e}_{15}^M & \mathbf{0} & \mathbf{e}_{15}^I & \mathbf{0} & -\boldsymbol{\varepsilon}_{11}^M & \mathbf{0} & -\boldsymbol{\varepsilon}_{11}^I
\end{bmatrix}
\begin{Bmatrix}
\mathbf{w}^M \\ \mathbf{t}^M \\ \mathbf{w}^I \\ \mathbf{t}^I \\ \boldsymbol{\Phi}^M \\ \boldsymbol{\Psi}^M \\ \boldsymbol{\Phi}^I \\ \boldsymbol{\Psi}^I
\end{Bmatrix}
=
\begin{Bmatrix}
\mathbf{a} \\ \mathbf{0} \\ \mathbf{b} \\ \mathbf{0} \\ \mathbf{0} \\ \mathbf{0} \\ \mathbf{0} \\ \mathbf{0}
\end{Bmatrix},
\tag{3-19}
$$

where $\{\mathbf{a}\}$ and $\{\mathbf{b}\}$ are the forcing terms due to the far-field antiplane shears and the far-field inplane electric fields as shown in Appendix 3-1, $[\mathbf{c}_{44}^M]$, $[\mathbf{c}_{44}^I]$, $[\mathbf{e}_{15}^M]$, $[\mathbf{e}_{15}^I]$, $[\boldsymbol{\varepsilon}_{11}^M]$ and $[\boldsymbol{\varepsilon}_{11}^I]$ are defined as follows:

$$
[\mathbf{c}_{44}^M]=
\begin{bmatrix}
c_{44}^M & 0 & \cdots & 0 \\
0 & c_{44}^M & \cdots & 0 \\
\vdots & \vdots & \ddots & \vdots \\
0 & 0 & \cdots & c_{44}^M
\end{bmatrix},
\quad
[\mathbf{c}_{44}^I]=
\begin{bmatrix}
c_{44}^I & 0 & \cdots & 0 \\
0 & c_{44}^I & \cdots & 0 \\
\vdots & \vdots & \ddots & \vdots \\
0 & 0 & \cdots & c_{44}^I
\end{bmatrix},
\tag{3-20}
$$

$$
[\mathbf{e}_{15}^M]=
\begin{bmatrix}
e_{15}^M & 0 & \cdots & 0 \\
0 & e_{15}^M & \cdots & 0 \\
\vdots & \vdots & \ddots & \vdots \\
0 & 0 & \cdots & e_{15}^M
\end{bmatrix},
\quad
[\mathbf{e}_{15}^I]=
\begin{bmatrix}
e_{15}^I & 0 & \cdots & 0 \\
0 & e_{15}^I & \cdots & 0 \\
\vdots & \vdots & \ddots & \vdots \\
0 & 0 & \cdots & e_{15}^I
\end{bmatrix},
\tag{3-21}
$$

$$
[\boldsymbol{\varepsilon}_{11}^M]=
\begin{bmatrix}
\varepsilon_{11}^M & 0 & \cdots & 0 \\
0 & \varepsilon_{11}^M & \cdots & 0 \\
\vdots & \vdots & \ddots & \vdots \\
0 & 0 & \cdots & \varepsilon_{11}^M
\end{bmatrix},
\quad
[\boldsymbol{\varepsilon}_{11}^I]=
\begin{bmatrix}
\varepsilon_{11}^I & 0 & \cdots & 0 \\
0 & \varepsilon_{11}^I & \cdots & 0 \\
\vdots & \vdots & \ddots & \vdots \\
0 & 0 & \cdots & \varepsilon_{11}^I
\end{bmatrix}.
\tag{3-22}
$$

The matrix $[\mathbf{I}]$ is an identity matrix. After obtaining the unknown Fourier coefficients in Eq. (3-19), the origin of observer system is set to c_k in the B_k integration as shown in Fig. 2-4 (b) to obtain the field potential by employing Eq. (2-11). In determining the stress and electric fields, the gradient of potential should be determined with care as shown in Section 2.4.3. The flowchart of the present method for anti-plane piezoelectricity problems is shown in Table 3-2.

3.4 Illustrative examples and discussions

The exact solution for a single piezoelectric inclusion, which was obtained by Pak [74], can be derived by using the present formulation. Although our formulation is general for multiple inclusions, we consider two piezoelectric circular inclusions perfectly bonded to a matrix which is subjected to the remote shear and electric field as shown in Fig. 3-3. For the purpose of comparison, the applied loadings and material properties of the matrix and inclusions are assumed as the same of Pak [74], Chao and Chang [20], Wang and Shen [88], Wu and Funami [95] and Emets and Onofrichuk [46]. All the numerical results are given below by using only twenty terms of Fourier series ($L = 20$) since those are checked to achieve good accuracy under acceptable error tolerance as compared to those by using the thirty terms.

Case 1: Two piezoelectric circular inclusions parallel to the applied loadings solved by Chao and Chang

We consider two piezoelectric circular inclusions of radii $r_2 = 2r_1$ perfectly bonded to a piezoelectric matrix which is subjected to the remote shear $\sigma_{zy}^\infty = \tau_\infty$ and electric field $E_y^\infty = E_\infty$ as shown in Fig. 3-3. In the following discussion, the material constants of the matrix and two inclusions are assumed as the same of Chao and Chang [20] by using $c_{44}^M = c_{44}^I = 3.53 \times 10^{10} \, \text{Nm}^{-2}$, $\varepsilon_{11}^M = \varepsilon_{11}^I = 1.51 \times 10^{-8} \, \text{CV}^{-1} \, \text{m}^{-1}$, $e_{15}^I = 10 \, \text{Cm}^{-2}$ and other values are stated specifically.

In order to examine the accuracy of the present formulation, the stress concentration factor $\sigma_{z\theta} / \tau_\infty$ in the matrix at $\theta = 0°$ under remote loadings of $\tau_\infty = 5 \times 10^7 \, \text{Nm}^{-2}$ and $E_\infty = 10^6$, 0, $10^{-6} \, \text{Vm}^{-1}$ is plotted in Fig. 3-4 (a) as a function of the ratio of piezoelectric constants e_{15}^M / e_{15}^I, where the two circular inclusions are arrayed parallel to the applied loadings ($\beta = 90°$) and the distance between two circular inclusions $d / r_1 = 10$. It is found that the results displayed in Fig. 3-4 (a) agree very well with Chao and Chang's results [20] and approach the Pak's solution of a single inclusion [74]. The electric field concentration E_θ / E_∞ in the matrix at $\theta = 0°$ with $E_\infty = 10^6 \, \text{Vm}^{-1}$ and $\tau_\infty = 5 \times 10^7$, 0, $-5 \times 10^7 \, \text{Nm}^{-2}$ is plotted in Fig. 3-4 (b) as a function of the ratio of piezoelectric constants. It is also found that the results in Fig. 3-4 (b) leads to the

Pak's solution of a single inclusion [74] since the two inclusions displace far away ($d/r_1 = 10$). The electric field concentration E_θ/E_∞ occurring at $\theta = 0°$ is plotted in Fig. 3-5 as a function of the ratio of dielectric constants $\varepsilon_{11}^M/\varepsilon_{11}^I$ while letting $c_{44}^M = c_{44}^I = 3.53 \times 10^{10}\,\mathrm{Nm}^{-2}$, $e_{15}^M = e_{15}^I = 17\,\mathrm{Cm}^{-2}$ and $\varepsilon_{11}^I = 1.51 \times 10^{-8}\,\mathrm{CV}^{-1}\,\mathrm{m}^{-1}$. It is shown that the electric field concentration approaches two for a large value of $\varepsilon_{11}^M/\varepsilon_{11}^I$ as $d/r_1 = 10$ which is consistent with Chao and Chang's results [20] and reduces to the Pak's solution of a single inclusion [74]. When the two inclusions approach each other, both the tangential stress $\sigma_{z\theta}$ and tangential electric field E_θ in the matrix along the boundary of the smaller inclusion are plotted in Figs. 3-6 (a) and 3-6 (b), respectively, as the piezoelectric constants are fixed at $e_{15}^M/e_{15}^I = 3$. Furthermore, we adopted the Parseval's theorem to study the convergence rate with different terms of Fourier series since the boundary densities are continuous on $[0, 2\pi]$. The Parseval's theorem are defined as below

$$\int_0^{2\pi} [f(\theta)]^2\, d\theta \doteq 2\pi a_0^2 + \pi \sum_{n=1}^{L} (a_n^2 + b_n^2)\,, \tag{3-23}$$

where

$$f(\theta) = a_0 + \sum_{n=1}^{L} (a_n \cos n\theta + b_n \sin n\theta)\,. \tag{3-24}$$

According to Eq. (3-23), we have the Parseval's sum versus various terms of Fourier series for boundary densities of each circular boundary in anti-plane elastic and in-plane electric fields as plotted in Figs. 3-7 (a) ~3-7 (h). It is found that no more than 20 terms can yield convergence. Figures 3-8 (a) and 3-8 (b) respectively show the tangential stress and tangential electric field distribution that the matrix is subjected to the reversal of the poling direction as compared to the inclusion due to the negative ratio of piezoelectric constants $e_{15}^M/e_{15}^I = -5$. The two figures show the consistency between the present data and those of Chao and Chang in ranges of $\theta = 0° \sim 180°$ except near $\theta = 90°$. It is open for discussions why our results are different from those of Chao and Chang near $\theta = 90°$. The tangential stress and tangential electric field are continuous across $\theta = 90°$ using our formulation while the results of Chao and Chang seems to have a jump at $\theta = 90°$ for the case of $d/r_1 = 0.01, 0.02$. For the negative ratio of $e_{15}^M/e_{15}^I = -5$, the Parseval's sum versus various terms of Fourier series for boundary

densities of each circular boundary in anti-plane elastic and in-plane electric fields is also done in Figs. 3-9 (a) ~3-9 (h). From the convergence test using the Parseval's theorem, it is also observed that only few terms of Fourier series can yield convergence for boundary densities.

Case 2: Two piezoelectric circular inclusions perpendicular to the applied loadings solved by Chao and Chang

As the two circular inclusions are arrayed perpendicular to the applied loadings ($\beta = 0°$), both the stress and electric field concentrations and distributions are also experienced. When the two inclusions approach each other, both the tangential stress $\sigma_{z\theta}$ and tangential electric field E_θ in the matrix along the boundary of the smaller inclusion are plotted in Figs. 3-10 (a) and 3-10 (b), respectively, as the piezoelectric constants are fixed at $e_{15}^M / e_{15}^I = -5$. After comparing with the results of Chao and Chang [20], agreement is made except near $\theta = 0°$ and $180°$. Variations of stress and electric field concentrations appear at $\theta = 0°$ with the ratio of piezoelectric constants as shown in Figs. 3-11 (a) and 3-11 (b). It is seen that, from Figs. 3-11 (a) ~3-12 (b), both the stress and electric field concentrations are equal to one as $e_{15}^M / e_{15}^I = 1$ which are reasonable results due to homogeneity. The stress and electric field concentrations are plotted in Figs. 3-12 (a) and 3-12 (b) under loadings of various magnitude for a far-field inplane electric load E_∞ and a far-field antiplane shear τ_∞, respectively. After comparing with the results of Chao and Chang [20], agreement is made except for the negative value of e_{15}^M / e_{15}^I. However, our results are smoother as shown in Figs. 3-11 (a) ~3-12 (b) which are different from the oscillation behavior in the Chao and Chang's paper [20]. To reconfirm our validity of formulation, we choose other cases by others for comparison.

Case 3: Two piezoelectric circular inclusions under two-direction loadings solved by Wang and Shen

In this case, the radii of two piezoelectric circular inclusions are r_1 and r_2 with $r_2 = 1.5r_1$ and the magnitude of remote loadings are $\sigma_{zx}^\infty = \tau_\infty / 2 = 2.5 \times 10^7 \, \text{Nm}^2$,

$\sigma_{zy}^{\infty} = \tau_{\infty} = 5 \times 10^7 \, \text{Nm}^2$, $E_x^{\infty} = E_{\infty}/2 = 0.5 \times 10^6 \, \text{Vm}$ and $E_y^{\infty} = E_{\infty} = 10^6 \, \text{Vm}$. The distance between the two inclusions is $d = 0.01r_1$ and the orientation is $\beta = 0°$. The material constants of the matrix and two inclusions are assumed as the same of Wang and Shen [88] by using $c_{44}^M = 3.53 \times 10^{10} \, \text{Nm}^{-2}$, $c_{44}^I = 1.00 \times 10^9 \, \text{Nm}^{-2}$, $e_{15}^M = 10 \, \text{Cm}^{-2}$, $e_{15}^I = 20 \, \text{Cm}^{-2}$, $\varepsilon_{11}^M = \varepsilon_{11}^I = 1.51 \times 10^{-8} \, \text{CV}^{-1} \text{m}^{-1}$.

Figure 3-13 shows that the stress and electric displacement distribution along the x axis. It is observed that σ_{zx} and D_x are continuous while σ_{zy} and D_y are discontinuous across the interface between the matrix and inclusions. We also note that the stress and electric displacement are not uniform within the two inclusions. Figure 3-14 shows the distribution of stress and electric displacement along the interface between the matrix and the smaller inclusion. Figure 3-15 shows the distribution of stress and electric displacement along the interface between the matrix and the larger inclusion. According to these curves, it is found that the normal stress σ_{zr} and electric displacement D_r in the matrix and inclusion are continuous through the interface due to the equilibrium and continuity requirement, respectively. Figure 3-16 illustrates the case when the larger inclusion and the matrix have the same material property. It indicates that the stress and electric displacement are uniform within the only inclusion. Figure 3-17 shows the case when the two inclusions are separated far away ($d / r_1 = 10$). In this case, the stress and electric displacement are uniform in both of the two inclusions. Figures 3-18 (a) ~3-18 (c) respectively show the contours of shear stresses $\sigma_{zx}/\tau_{\infty}$, $\sigma_{zy}/\tau_{\infty}$ and electric potential Φ/E_{∞} subjected to the loadings $\sigma_{zx}^{\infty} = 0$, $\sigma_{zy}^{\infty} = \tau_{\infty}$, $E_x^{\infty} = 0$, $E_y^{\infty} = E_{\infty}$. It reveals that σ_{zx} and Φ are anti-symmetric with respect to the x axis and σ_{zy} is symmetric with respect to the x axis. There exists serious amplification at the point where the two inclusions are nearly in contact with each other. The electric potential is continuous across the interface between the matrix and each inclusion. The present results agree very well with Wang and Shen's results [88].

Case 4: Two piezoelectric circular inclusions with different geometries and material constants subjected to various loadings solved by Wu and Funami

In order to analyze the interaction between two piezoelectric circular inclusions centered on the x axis ($\beta = 0°$), we consider the variations of components of stresses and electric displacements along two different paths, the x axis and the contour $(1.01, \theta)$. In Figs. 3-19 (a) ~3-20 (b), the inhomogeneous medium is comprised of the polymer matrix and two PZT-7A circular inclusions. In Figs. 3-21 (a) ~3-22 (b), PZT-7A is still chosen as two inclusions and PZT-5 is taken as the matrix to show the interaction of different piezoelectric media. The material constants used in the numerical calculation are shown in Table 3-3. Figures 3-19 (a) ~3-19 (c) illustrate the stress and electric displacement distributions along the x axis when the distance d between two inclusions is equal to 0.05, 0.5 and 1.5, respectively and only the remote shear stress $\sigma_{zy}^{\infty} = \tau_{\infty}$ is applied. From these three figures, it is observed that the varying gradients of stress and electric displacement components inside two piezoelectric circular inclusions along the x axis become larger when the distance d decreases. It means that the interaction of two piezoelectric circular inclusions becomes more prominent when the distance d tends towards zero. Since the polymer is taken as the matrix that has no piezoelectric properties, the stress σ_{zy} and electric displacement D_y tend to τ_{∞} and zero, respectively, when the variable x tends to infinity.

To show the effect of the geometric size of the piezoelectric circular inclusion on the distribution of stress and electric displacement, the radii of two inclusions are taken as $r_2 = 2r_1$ in Fig. 3-20 (a). After comparing with Fig. 3-19 (b), the symmetry of the stress and electric displacement distributions on the point $x = 1.25$ is broken. The stress field in the left inclusion is slightly lower while it is relatively higher in the right inclusion. It indicates a smooth variation when the right inclusion becomes larger. This implies that the uniform shear stress $\sigma_{zy}^{\infty} = \tau_{\infty}$ at infinity is borne more by the larger inclusion than the smaller one. For the electric displacement component, a similar variation to the stress field is found in Fig. 3-20 (a). Figure 3-20 (b) shows the stress and electric displacement distributions along the contour $(1.01, \theta)$ when only the remote shear stress $\sigma_{zy}^{\infty} = \tau_{\infty}$ is applied. It is seen that the stress σ_{zr} and electric displacement D_r have an asymmetric distribution and the electro-elastic field $\sigma_{z\theta}$ and D_{θ} have a symmetric distribution on $\theta = \pi$. The value of stress component $\sigma_{z\theta}$ is relatively low in

comparison with σ_{zr}.

To show the interaction of different piezoelectric media and different loadings applied at infinity, we choose PZT-5 as the matrix and different loadings are applied at infinity in Figs. 3-21 (a) ~3-22 (b). Figures 3-21 (a) ~3-21 (c) illustrate the stress and electric displacement distributions along the x axis subjected to the applied loading $E_y^\infty = E_\infty$, $E_x^\infty = E_\infty$ and $\sigma_{zx}^\infty = \tau_\infty$ at infinity, respectively. From Fig. 3-21 (a), it indicates that the stress field σ_{zy} in two piezoelectric circular inclusions has a different sign from one in the matrix. Particularly, the stress σ_{zy} between two inclusions has a larger varying gradient. In comparison with the stress field, the electric displacement field has a smooth tendency. From Figs. 3-21 (b) and 3-21 (c), it is seen that the distributions of stress σ_{zx} and electric displacement D_x are continuous across the interface between the matrix and inclusions. In comparison with Fig. 3-21 (c), the stress component between the matrix and right inclusion in Fig. 3-21 (b) has a larger varying gradient. This means that the electric field intensity E_∞ has a more important impact on the distribution of the stress field than the shear stress τ_∞.

Figures 3-22 (a) and 3-22 (b) show the stress and electric displacement distributions along the x axis when two piezoelectric circular inclusions are tangent to each other. Since two piezoelectric circular inclusions have the same material properties, the stress component σ_{zy} and electric displacement component D_y at the point $x = 1$ are continuous. From Fig. 3-22 (a), it is found that the stress field near the tangent point of two piezoelectric circular inclusions has a larger varying gradient when the electric field $E_y^\infty = E_\infty$ at infinity is applied. In comparison with the stress field of Fig. 3-22 (a), the stress field of Fig. 3-22 (b) has a relatively smooth variation. The present results in Figs. 3-19 (a) ~3-22 (b) agree very well with those solved by Wu and Funami [95].

Case 5: Uncoupling case of in-plane electrostatic problems

As mentioned previously, the present solution on the mechanical and electrical fields can reduce to the uncoupling case of Emets and Onofrichuk [46] when the coupling effect between the mechanical and electrical fields of the piezoelectric medium is absent. Figure 3-23 shows that two dielectric circular inclusions with radii of $r_2 = 0.8 r_1$

imbedded in an infinite dielectric medium are in various uniform electric fields $E_x^\infty = E_\infty$, $(E_x^\infty, E_y^\infty) = (E_\infty \cos 45°, E_\infty \sin 45°)$ and $E_y^\infty = E_\infty$ applied at infinity, respectively. The distance between two inclusions is $d = 0.1r_1$ and dielectric constants for matrix and each inclusion are ε_0, ε_1 and ε_2. Illustrations of the patterns of the electric field are shown in Figures 3-24 (a) and 3-24 (b) for different compositions of the dielectric constant, *e.g.* $\varepsilon_0 = 3$, $\varepsilon_1 = 9$, $\varepsilon_2 = 5$ and $\varepsilon_0 = 2$, $\varepsilon_1 = 9$, $\varepsilon_2 = 1$. From these patterns of the electric field, it is observed that the electric field is continuous across the interface between the matrix and inclusions and agrees well with those of Emets and Onofrichuk [46].

3.5 Concluding remarks

The present work not only demonstrated an elegant method for solving boundary value problems but also understood the interesting coupling behaviors between mechanical and electrical fields that have not been studied previously by using BIE. It was shown that the concentration behavior of stress and electric fields depends on the distance between two piezoelectric inclusions, the mismatch in the material constants and the magnitude of mechanical and electromechanical loadings. In addition, the interaction between two piezoelectric circular inclusions has a more important effect on the distributions of stress and electric displacement when the distance between two inclusions approaches zero or even touches each other. The uncoupling case reduces to either anti-plane elastic or in-plane electrostatic problems. Singularity free and boundary-layer effect free are the main gains using the present formulation as well as the exponential convergence. The present study is useful in designing piezoelectric composites and in understanding the coupling effects of two inclusions.

Table 3-1 Analogy between the anti-plane shear deformation and in-plane electrostatics for anti-plane piezoelectric problems

Anti-plane shear deformation	Constitutive equations for anti-plane piezoelectricity	In-plane electrostatics
z-displacement w		Electric potential Φ
Strain γ_{zi}		Electric field E_i
Stress σ_{zi}	Shear modulus c_{44}	Electric displacement D_i
Shear modulus μ	Dielectric constant ε_{11}	Dielectric constant ε
Body force f	Piezoelectric constant e_{15}	Charge density ρ *
Strain-disp. relationship $\gamma_{zi} = w_{,i}$	Coupling effect $\sigma_{zi} = c_{44}\gamma_{zi} - e_{15}E_i$ $D_i = e_{15}\gamma_{zi} + \varepsilon_{11}E_i$	Electricity $E_i = -\Phi_{,i}$
Constitutive law $\sigma_{zi} = \mu\gamma_{zi}$		Constitutive law $D_i = \varepsilon E_i$
Governing equation of equilibrium $\sigma_{zi,i} = -f_z$		Governing equation of Maxwell $D_{i,i} = \rho$
Poisson equation $\nabla^2 w = -f/\mu$		Poisson equation $\nabla^2 \Phi = -\rho/\varepsilon$

* Here, ρ is the charge density. The subscript "," refers to partial differentiation with respect to the subsequent spatial coordinate "i".

Table 3-2 Flowchart of the present method for anti-plane piezoelectricity problems

```
┌──────────────────────────────────────────────────────┐
│         Laplace problem with circular boundaries       │
│      (anti-plane elastic and in-plane electric fields)│
└──────────────────────────────────────────────────────┘
                          │
┌──────────────────────────────────────────────────────┐
│          Null-field integral equation in Eq. (2-22)    │
└──────────────────────────────────────────────────────┘
         │                                    │
┌─────────────────────────┐   ┌──────────────────────────┐
│   Fundamental solution   │   │   Boundary densities for  │
│ [Degenerate kernels are  │   │    circular boundaries    │
│   listed in Table 2-2]   │   │  [Fourier series in Eqs.  │
│                          │   │    (2-20) and (2-21)]     │
└─────────────────────────┘   └──────────────────────────┘
                          │
┌──────────────────────────────────────────────────────┐
│    Adaptive observer system in the boundary integrations│
└──────────────────────────────────────────────────────┘
```

Analytical part

```
┌──────────────────────────────────────────────────────┐
│  Collocating the null-field point to construct the     │
│  compatible relationship among boundary data in        │
│  Eqs. (3-11)~ (3-14)                                   │
└──────────────────────────────────────────────────────┘
                          │
┌──────────────────────────────────────────────────────┐
│       Constructing influence coefficients in Table 2-2 │
└──────────────────────────────────────────────────────┘
         │                                    │
┌─────────────────────────┐   ┌──────────────────────────┐
│ Continuity and equilibrium│  │ Continuity and equilibrium│
│ conditions of anti-plane │   │ conditions of in-plane    │
│ elastic field using Eq.  │   │ electric field using Eq.  │
│ (3-15) and (3-16)        │   │ (3-17) and (3-18)         │
└─────────────────────────┘   └──────────────────────────┘
```

Numerical Part

```
┌──────────────────────────────────────────────────────┐
│         Linear algebraic system in Eq. (3-19)          │
└──────────────────────────────────────────────────────┘
                          │
┌──────────────────────────────────────────────────────┐
│   Obtain the unknown Fourier coefficients in Eq. (3-19)│
└──────────────────────────────────────────────────────┘
                          │
┌──────────────────────────────────────────────────────┐
│ Boundary integral equation for the domain point in Eq. (2-11)│
└──────────────────────────────────────────────────────┘
                          │
┌──────────────────────────────────────────────────────┐
│              Vector decomposition technique            │
└──────────────────────────────────────────────────────┘
                          │
┌──────────────────────────────────────────────────────┐
│       Potential gradient for stress and electric fields│
└──────────────────────────────────────────────────────┘
```

Table 3-3 Electro-elastic material properties

	c_{44} (GPa)	e_{15} (Cm^{-2})	$\varepsilon_{11}/\varepsilon_0$
PZT-7A	25.4	9.2	460
PZT-5	21.1	12.3	916
Polymer	0.64	0	9

Note: permittivity of free space $\varepsilon_0 = 8.85 \times 10^{-12}$ C^2 N^{-1} m^{-2}
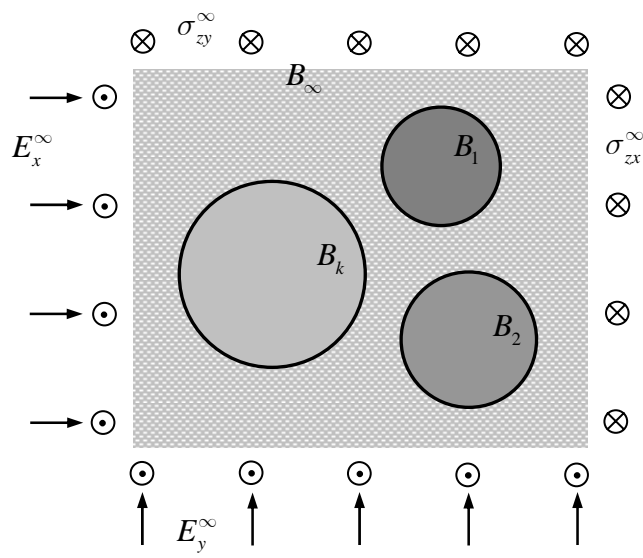
Figure 3-1 Infinite anti-plane piezoelectricity problem with arbitrary number of circular inclusions under remote shear and electric loadings
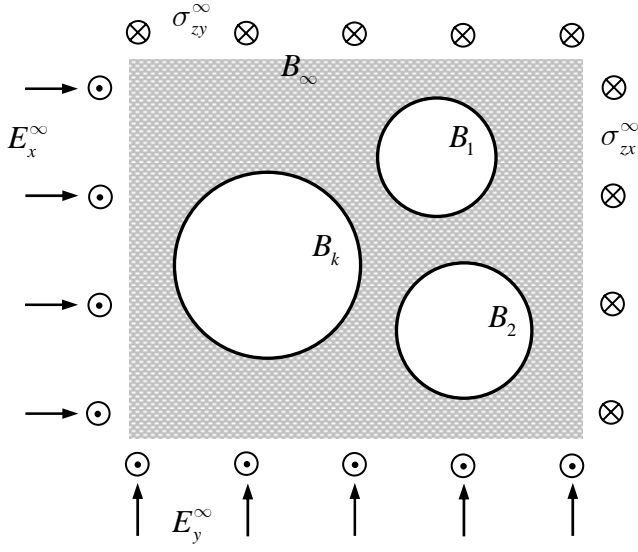
Figure 3-2 (a) Infinite piezoelectric medium with circular holes under remote shear and electric loadings
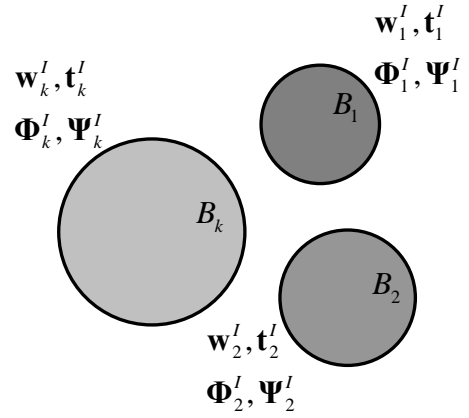
Figure 3-2 (b) Interior Laplace problems for each piezoelectric inclusion
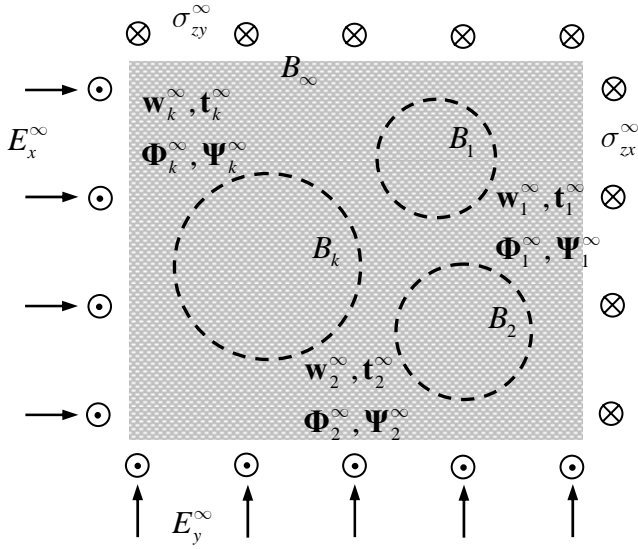
Figure 3-2 (c) Infinite piezoelectric medium under remote shear and electric loadings
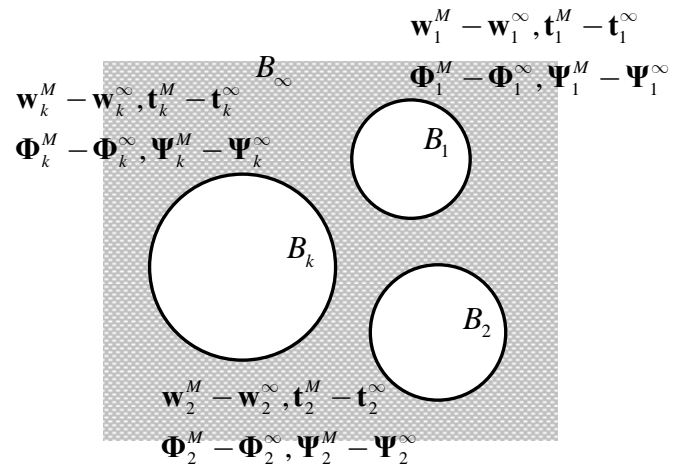
Figure 3-2 (d) Exterior Laplace problems for the piezoelectric medium
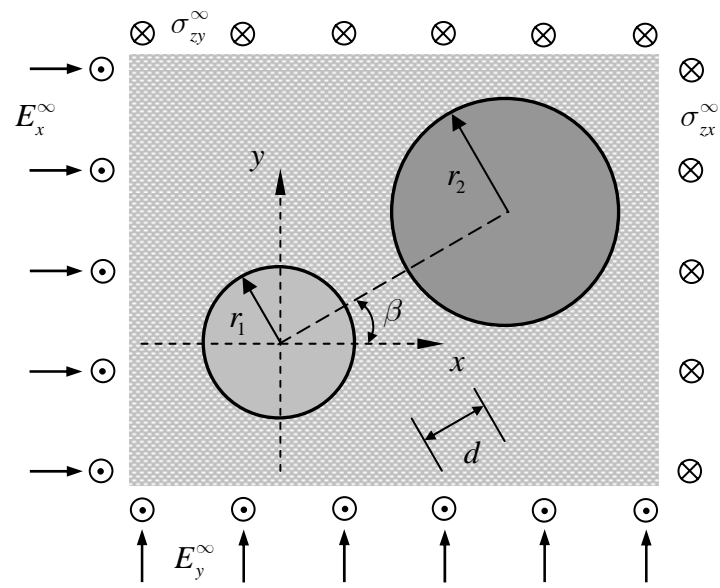
Figure 3-3 Two piezoelectric circular inclusions embedded in a piezoelectric matrix
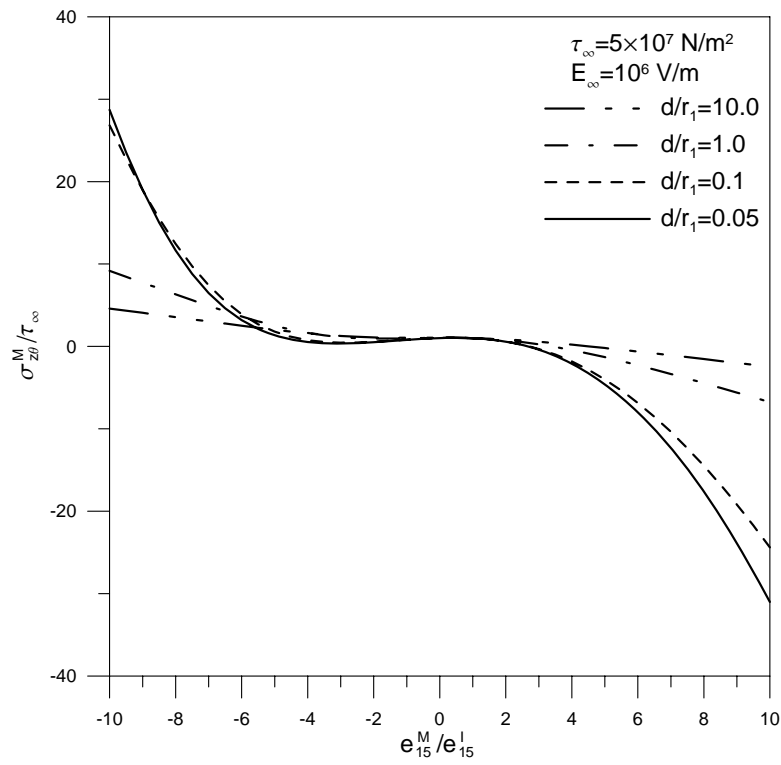under remote shear and electric loadings
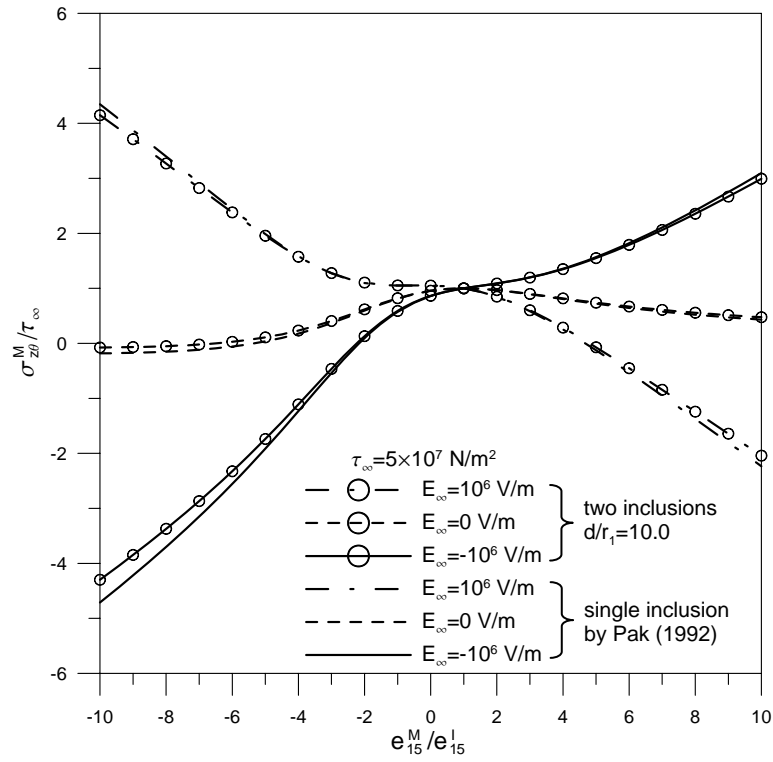
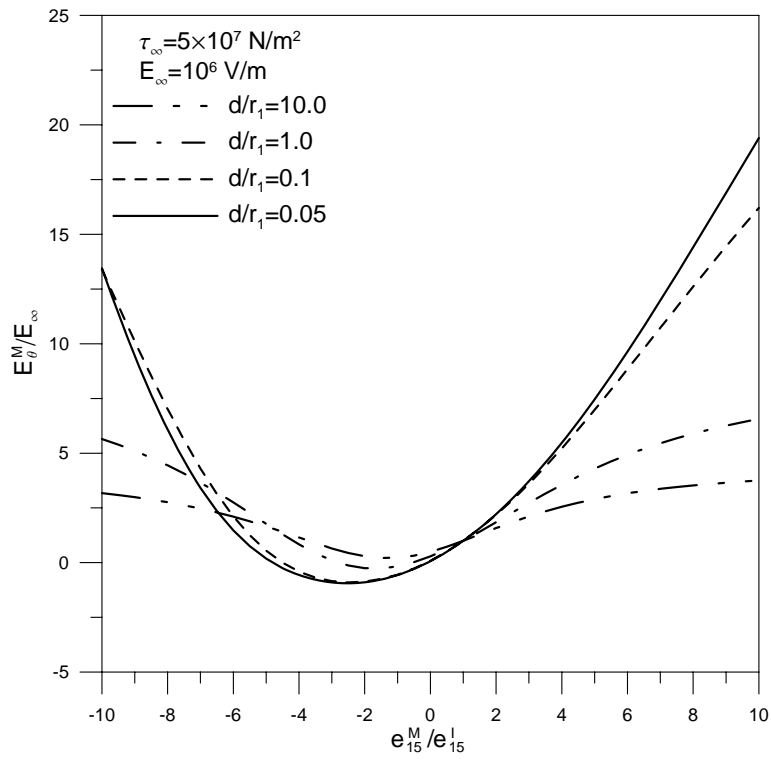Figure 3-4 (a) Stress concentrations as a function of the ratio of piezoelectric constants with $\beta = 90°$
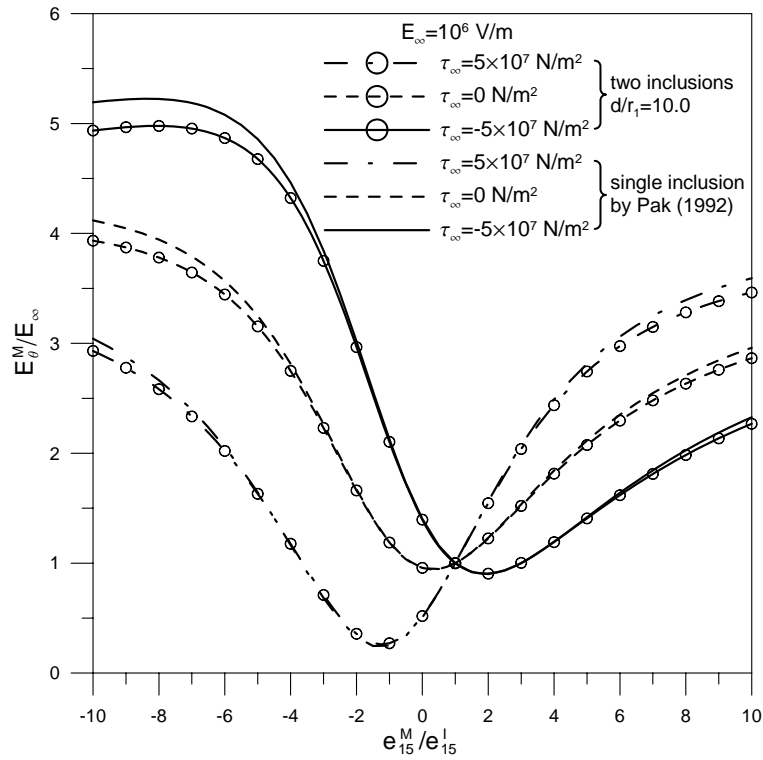
Figure 3-4 (b) Electric field concentrations as a function of the ratio of piezoelectric constants with $\beta = 90°$
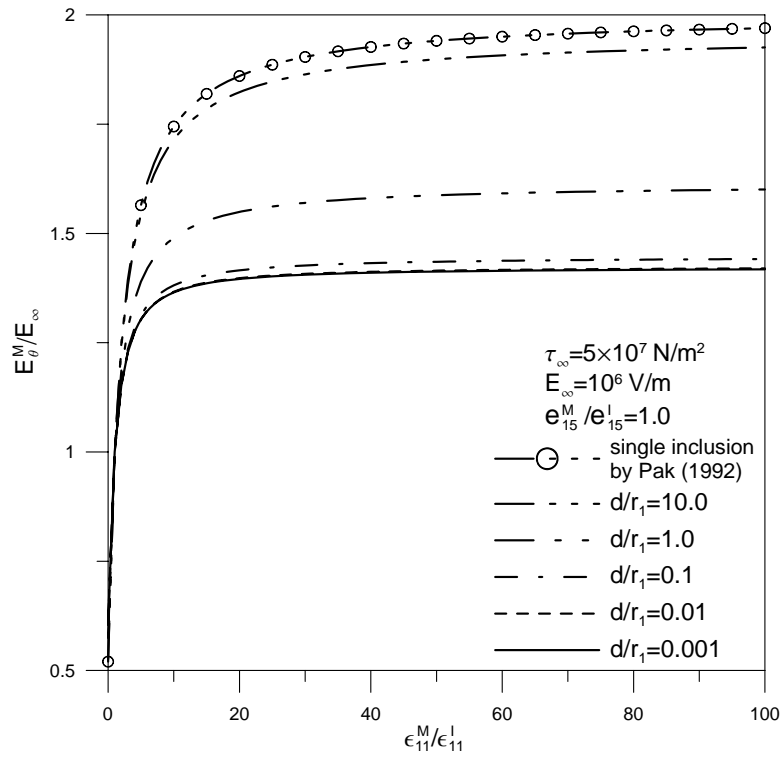
Figure 3-5 Electric field concentrations as a function of the ratio of dielectric constants with $e_{15}^M / e_{15}^I = 1.0$ and $\beta = 90°$
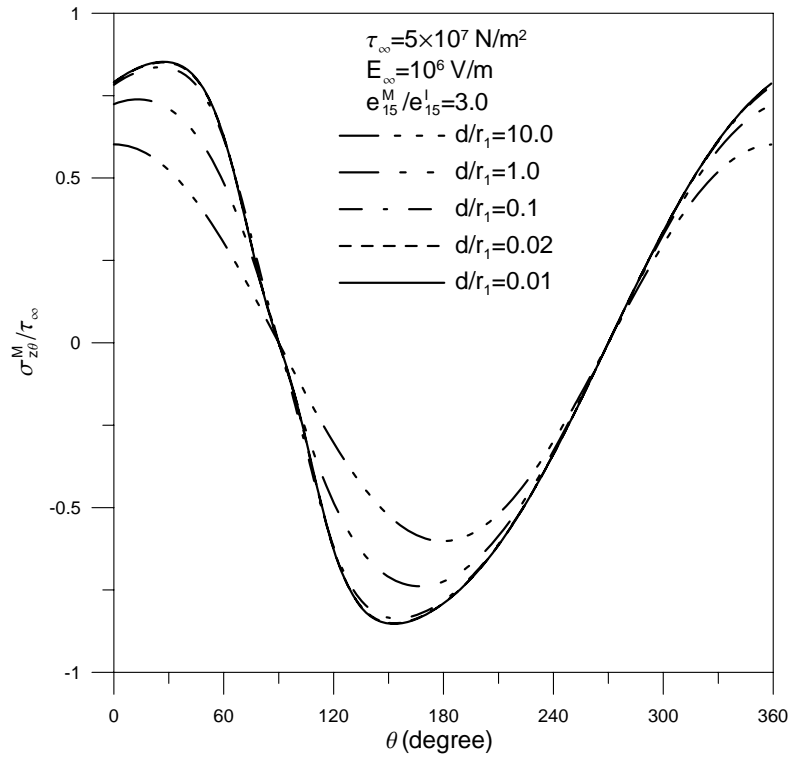
Figure 3-6 (a) Tangential stress distributions for different ratios d/r_1 with $e_{15}^M/e_{15}^I = 3.0$ and $\beta = 90°$
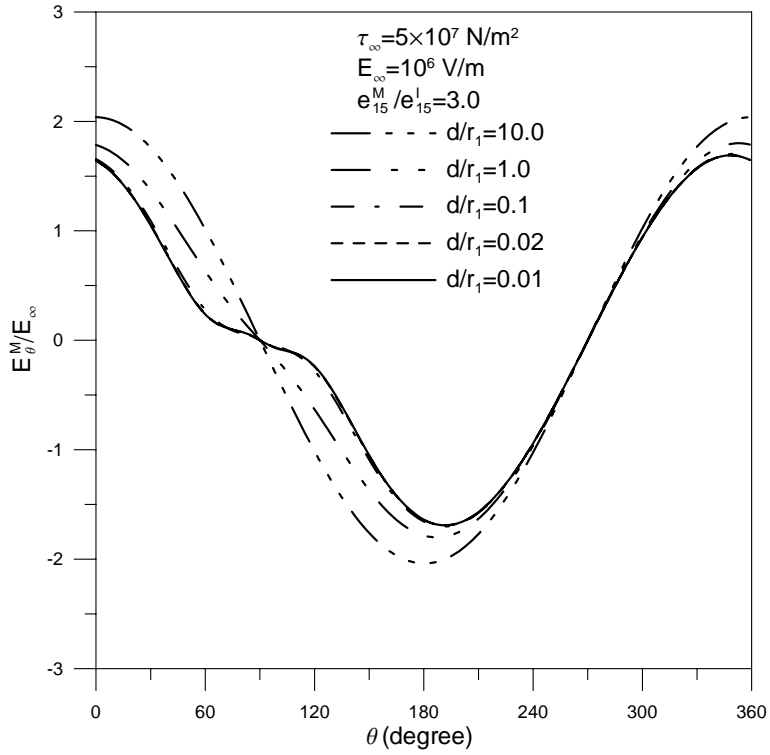
Figure 3-6 (b) Tangential electric field distributions for different ratios d/r_1 with $e_{15}^M/e_{15}^I = 3.0$ and $\beta = 90°$
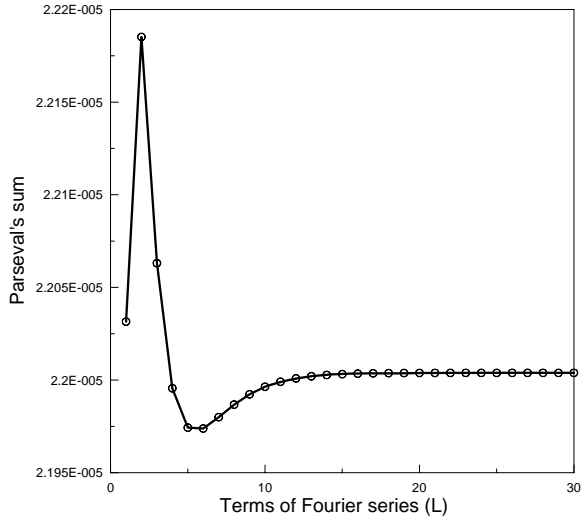
Figure 3-7 (a) Parseval's sum for w_1^M with $e_{15}^M / e_{15}^I = 3.0$ and $d / r_1 = 0.01$
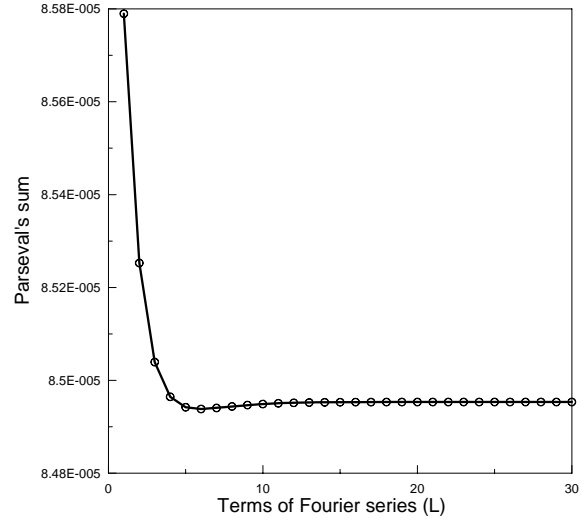
Figure 3-7 (b) Parseval's sum for w_2^M with $e_{15}^M / e_{15}^I = 3.0$ and $d / r_1 = 0.01$
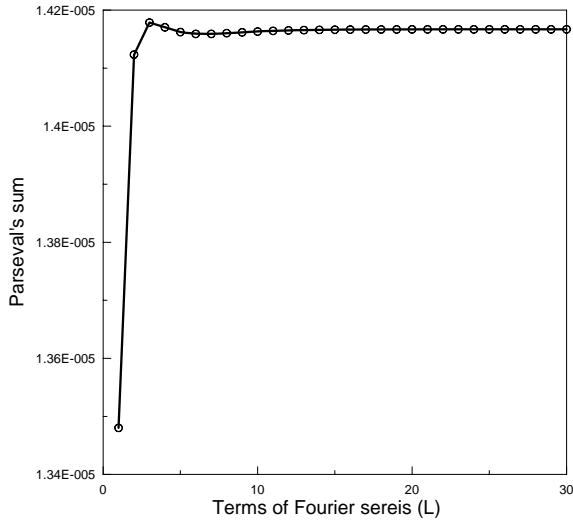
Figure 3-7 (c) Parseval's sum for t_1^M with $e_{15}^M / e_{15}^I = 3.0$ and $d / r_1 = 0.01$
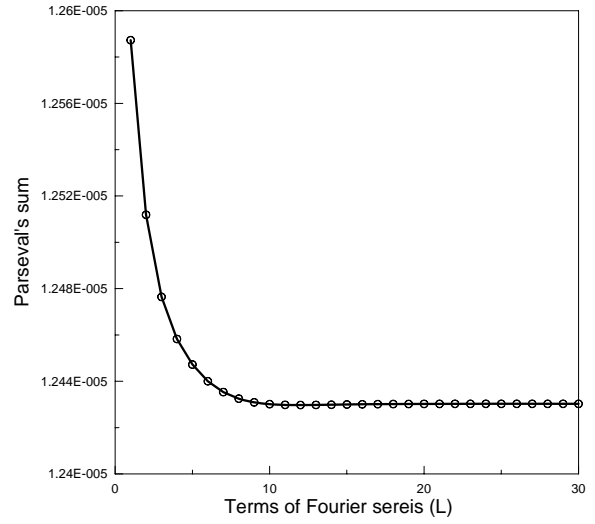
Figure 3-7 (d) Parseval's sum for t_2^M with $e_{15}^M / e_{15}^I = 3.0$ and $d / r_1 = 0.01$

59
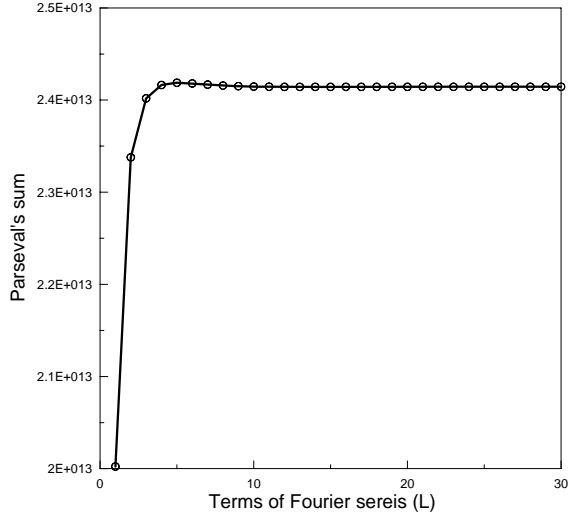
Figure 3-7 (e) Parseval's sum for Φ_1^M with $e_{15}^M / e_{15}^I = 3.0$ and $d / r_1 = 0.01$
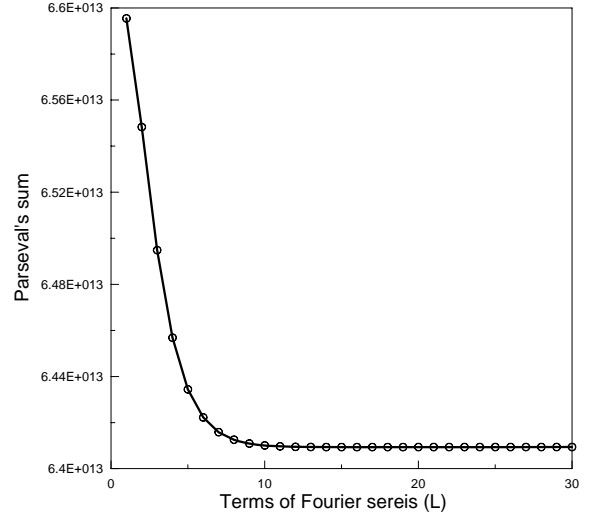
Figure 3-7 (f) Parseval's sum for Φ_2^M with $e_{15}^M / e_{15}^I = 3.0$ and $d / r_1 = 0.01$
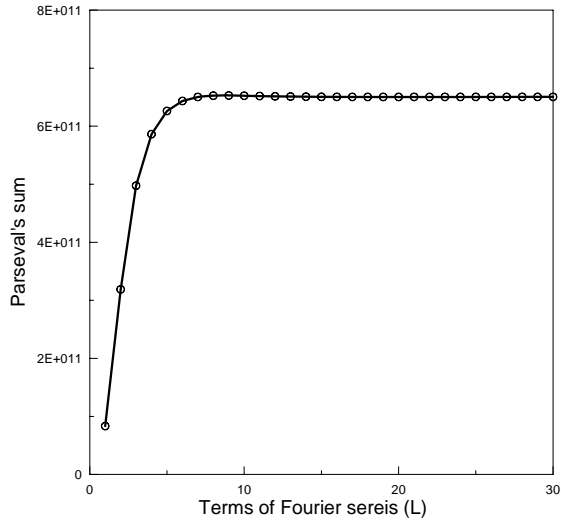
Figure 3-7 (g) Parseval's sum for Ψ_1^M with $e_{15}^M / e_{15}^I = 3.0$ and $d / r_1 = 0.01$
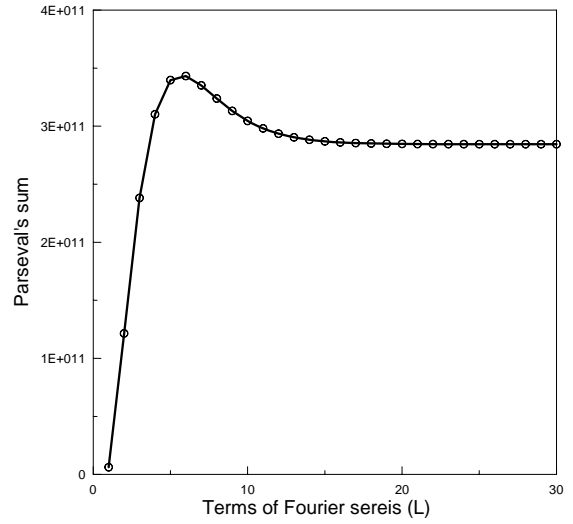
Figure 3-7 (h) Parseval's sum for Ψ_2^M with $e_{15}^M / e_{15}^I = 3.0$ and $d / r_1 = 0.01$
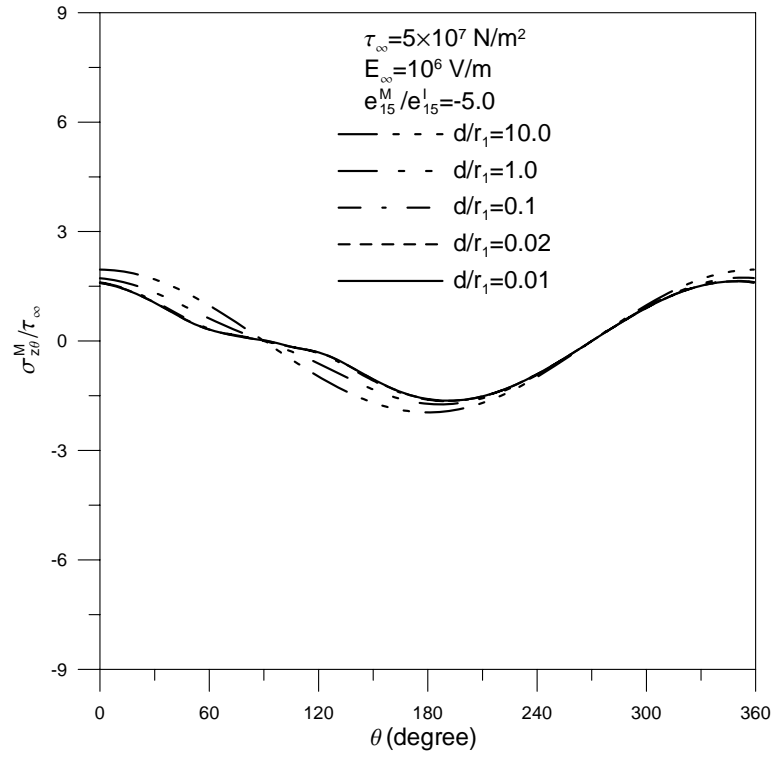
Figure 3-8 (a) Tangential stress distributions for different ratios d/r_1 with $e_{15}^M/e_{15}^I = -5.0$ and $\beta = 90°$
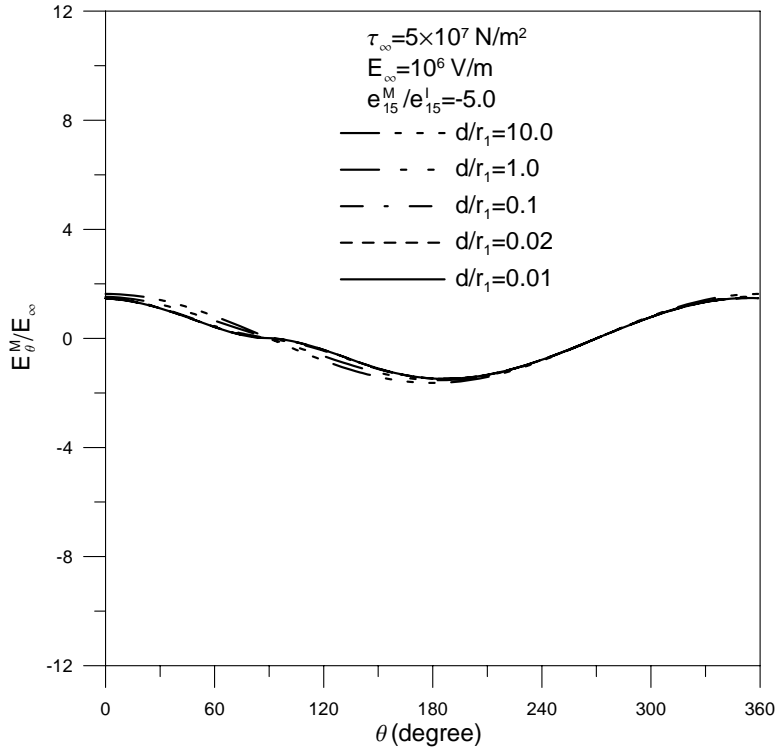
Figure 3-8 (b) Tangential electric field distributions for different ratios d/r_1 with $e_{15}^M/e_{15}^I = -5.0$ and $\beta = 90°$
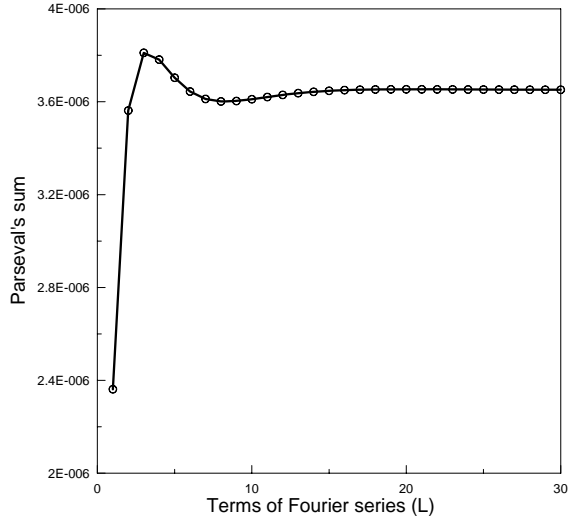
Figure 3-9 (a) Parseval's sum for w_1^M with $e_{15}^M / e_{15}^I = -5.0$ and $d / r_1 = 0.01$
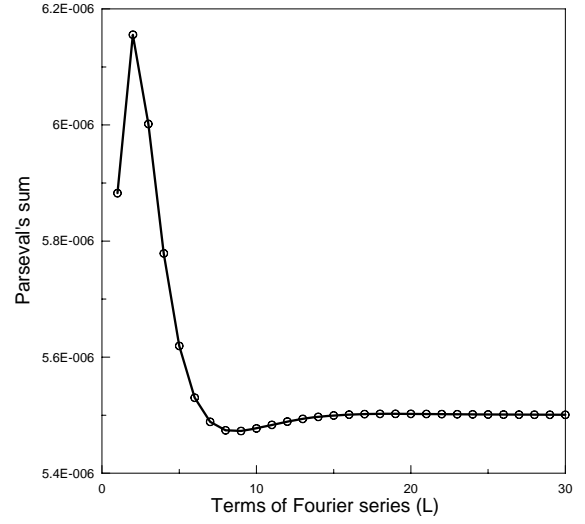
Figure 3-9 (b) Parseval's sum for w_2^M with $e_{15}^M / e_{15}^I = -5.0$ and $d / r_1 = 0.01$
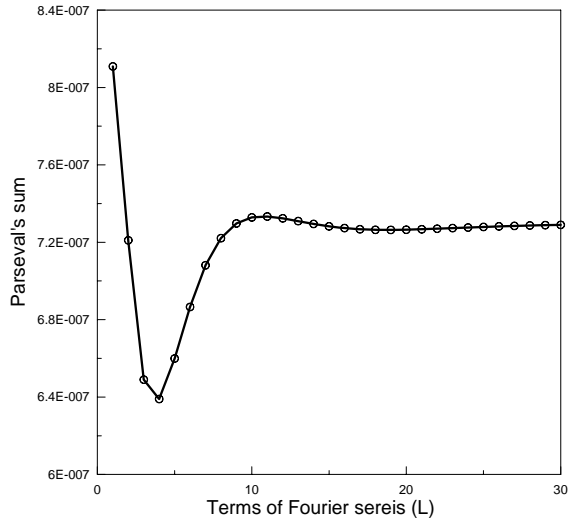
Figure 3-9 (c) Parseval's sum for t_1^M with $e_{15}^M / e_{15}^I = -5.0$ and $d / r_1 = 0.01$
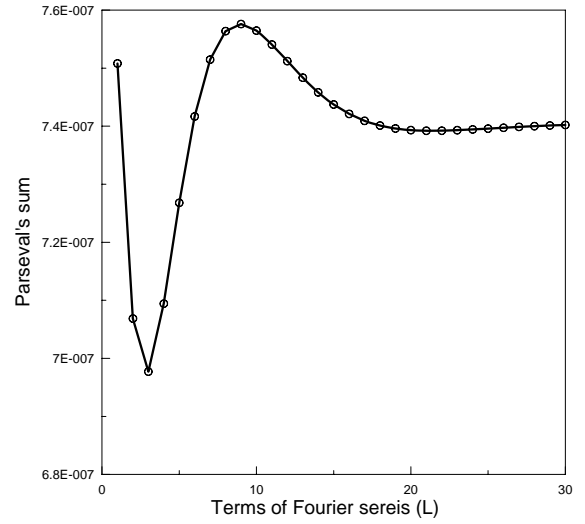
Figure 3-9 (d) Parseval's sum for t_2^M with $e_{15}^M / e_{15}^I = -5.0$ and $d / r_1 = 0.01$
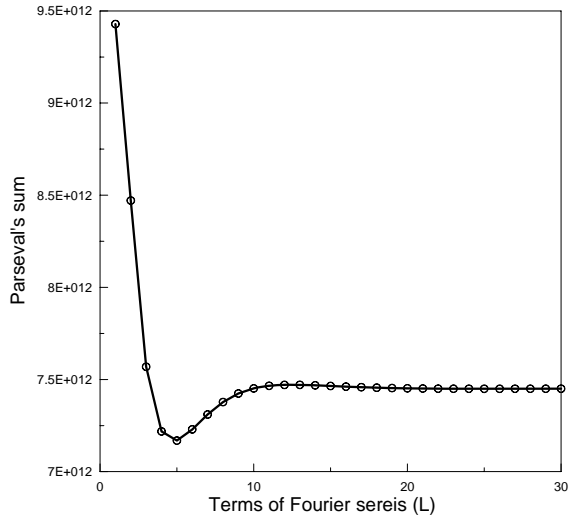
Figure 3-9 (e) Parseval's sum for Φ_1^M with $e_{15}^M / e_{15}^I = -5.0$ and $d / r_1 = 0.01$
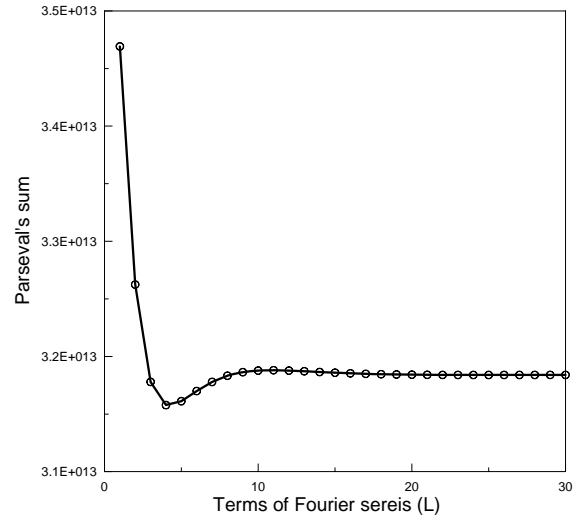
Figure 3-9 (f) Parseval's sum for Φ_2^M with $e_{15}^M / e_{15}^I = -5.0$ and $d / r_1 = 0.01$
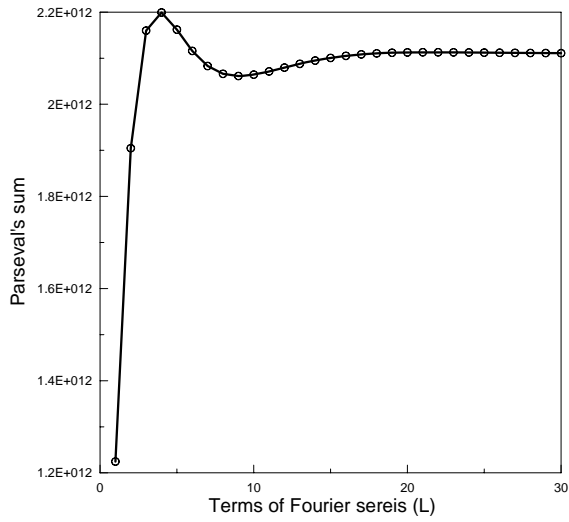
Figure 3-9 (g) Parseval's sum for Ψ_1^M with $e_{15}^M / e_{15}^I = -5.0$ and $d / r_1 = 0.01$
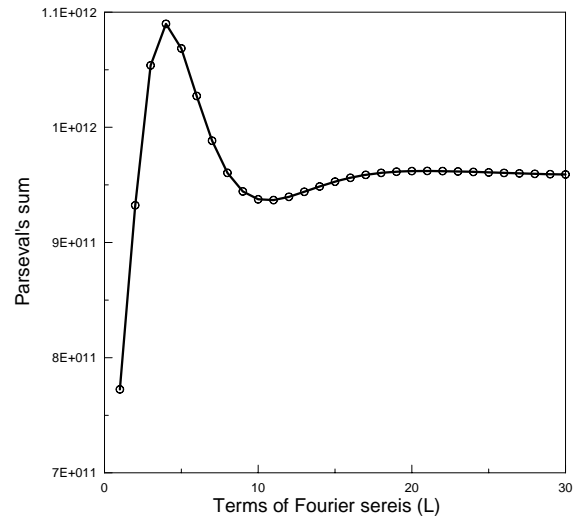
Figure 3-9 (h) Parseval's sum for Ψ_2^M with $e_{15}^M / e_{15}^I = -5.0$ and $d / r_1 = 0.01$
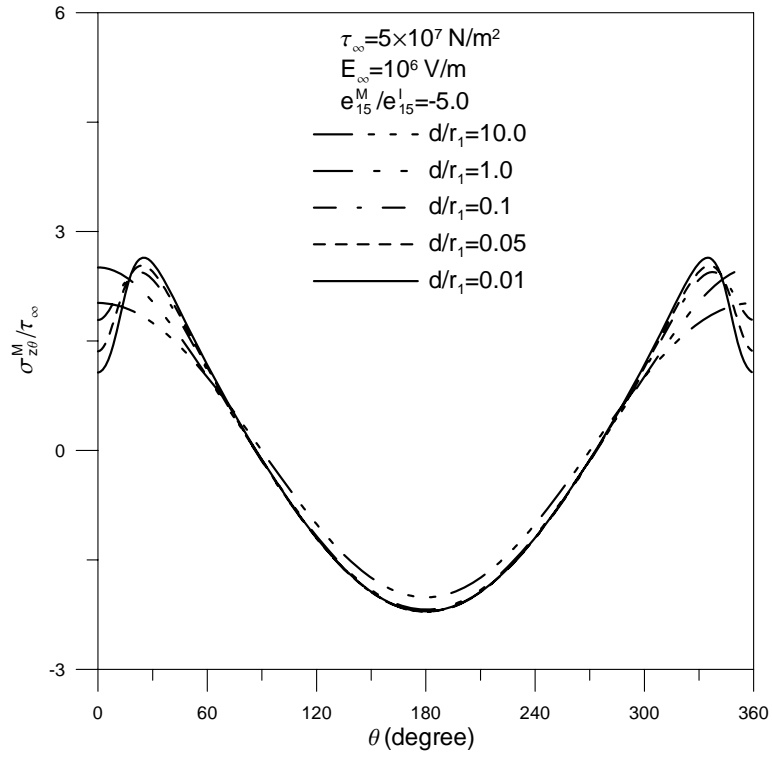
Figure 3-10 (a) Tangential stress distributions for different ratios d/r_1 with $e_{15}^M / e_{15}^I = -5.0$ and $\beta = 0°$
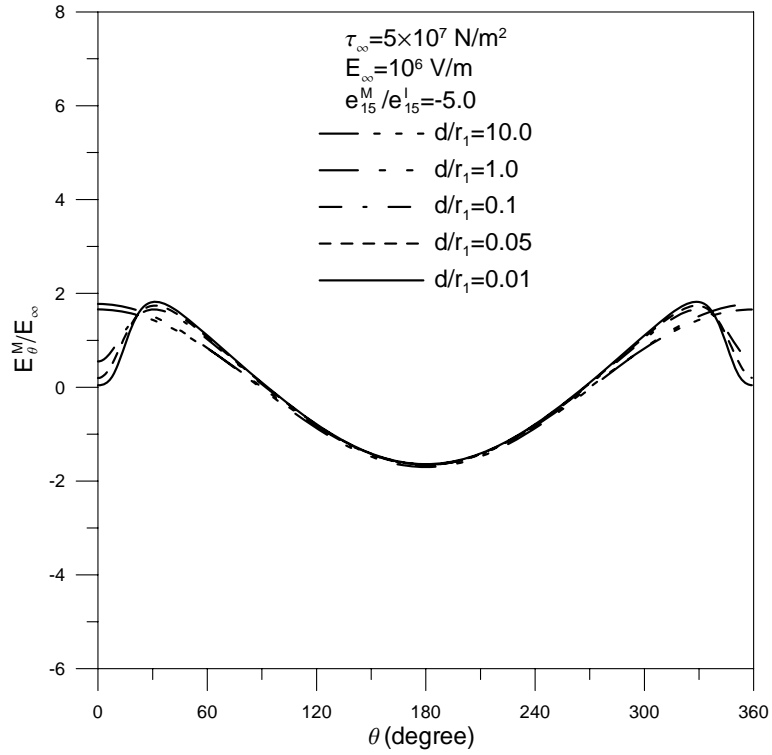
Figure 3-10 (b) Tangential electric field distributions for different ratios d/r_1 with $e_{15}^M / e_{15}^I = -5.0$ and $\beta = 0°$

Figure 3-11 (a) Stress concentrations as a function of the ratio of piezoelectric constants with $\beta = 0°$

Figure 3-11 (b) Electric field concentrations as a function of the ratio of piezoelectric constants with $\beta = 0°$
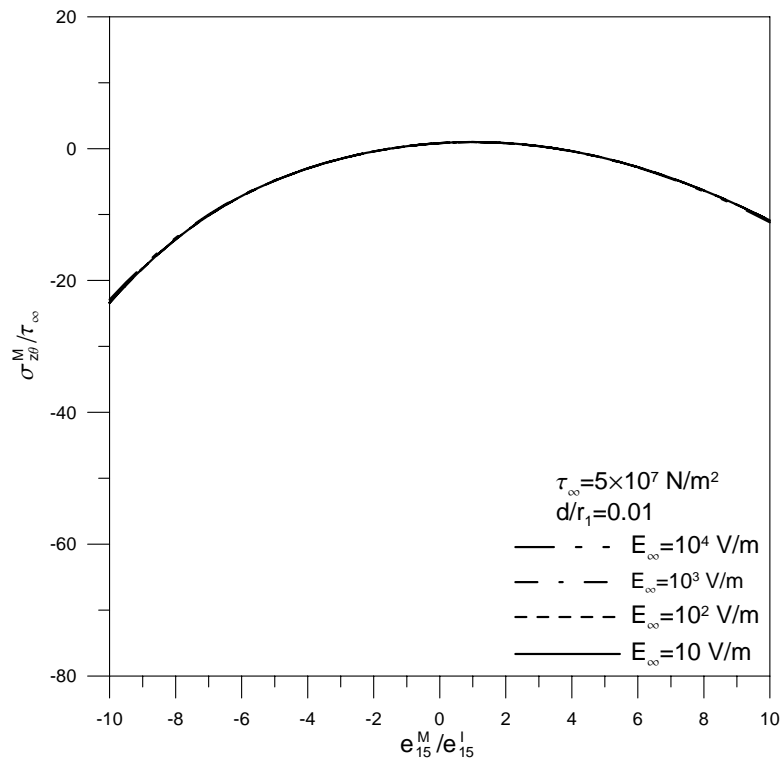
Figure 3-12 (a) Stress concentrations as a function of the ratio of piezoelectric constants with $\beta = 0°$
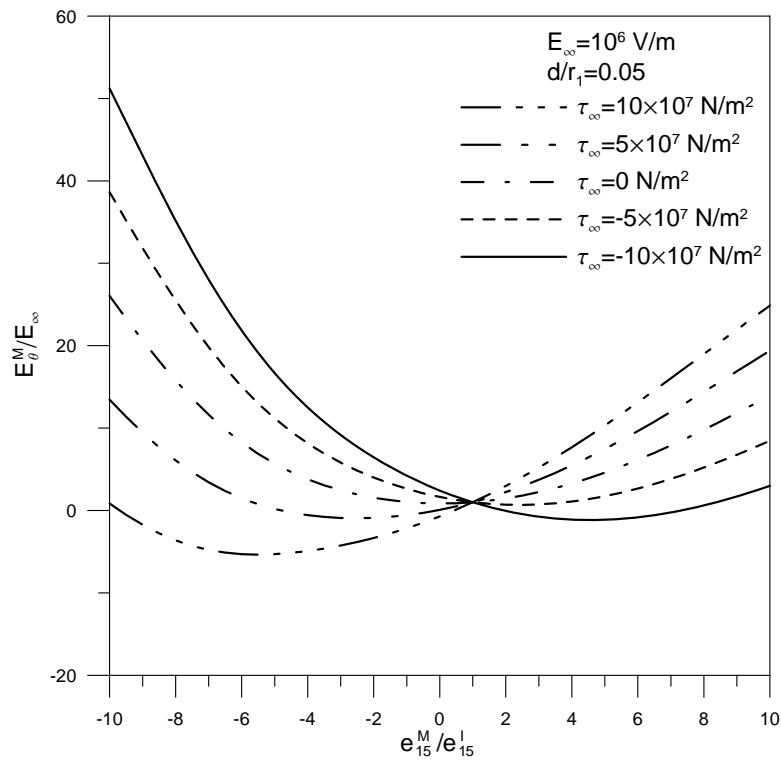
Figure 3-12 (b) Electric field concentrations as a function of the ratio of piezoelectric constants with $\beta = 0°$
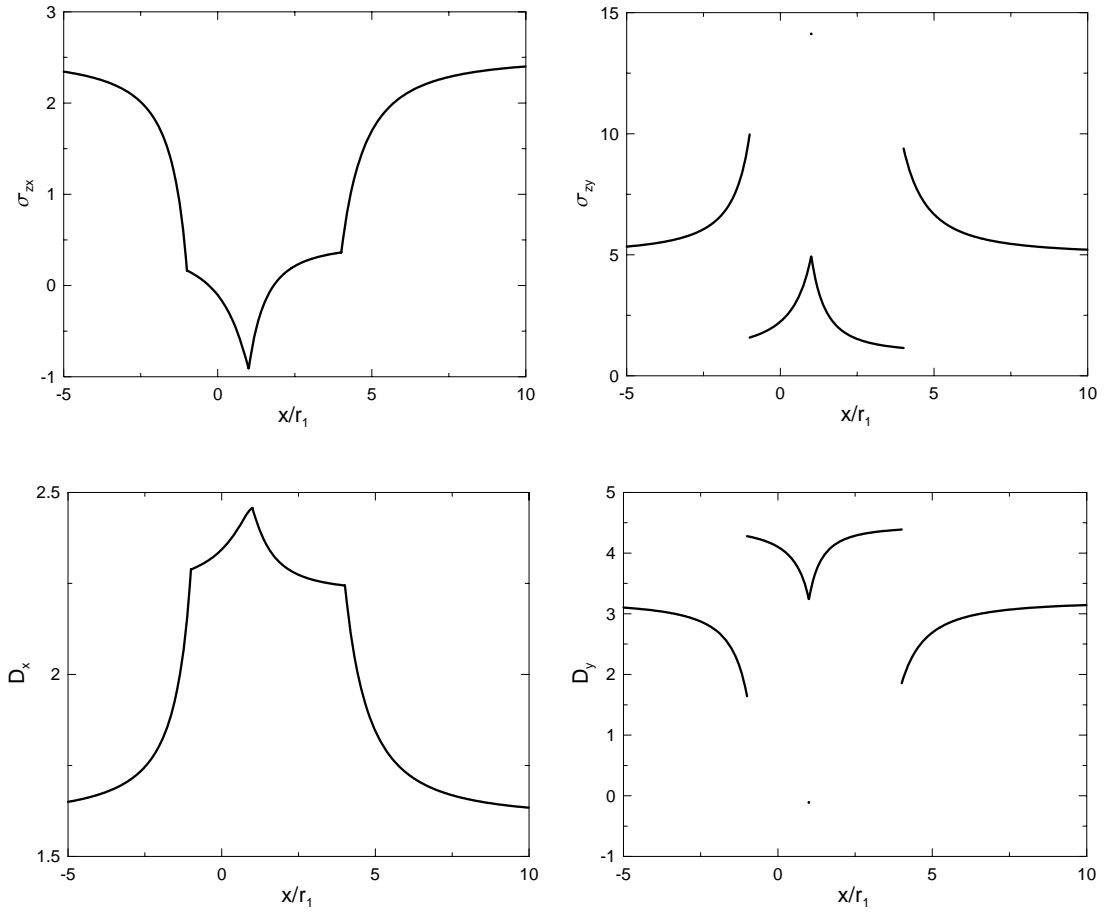
Figure 3-13 Stress and electric displacement distributions along the x axis
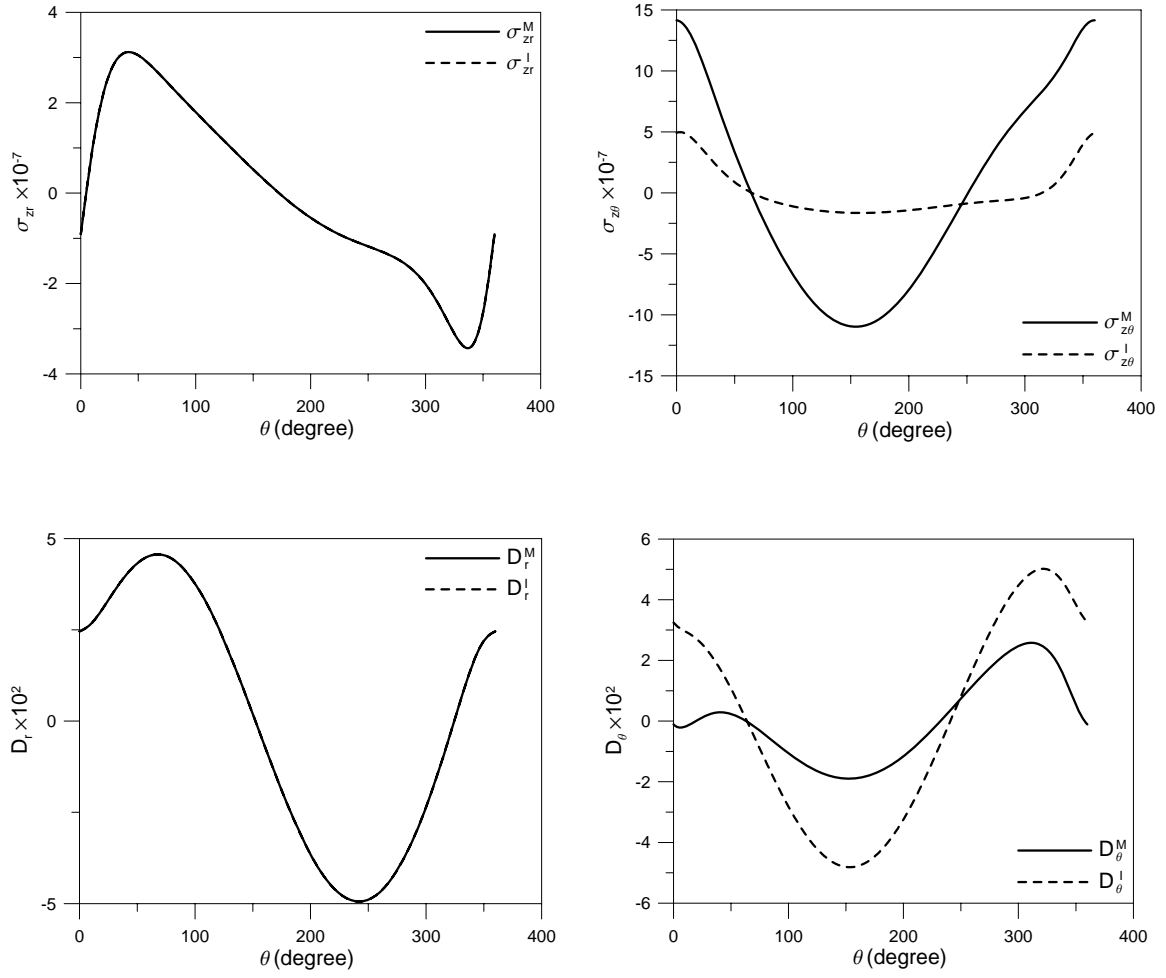
Figure 3-14 Stress and electric displacement distributions along the interface between the matrix and the smaller inclusion
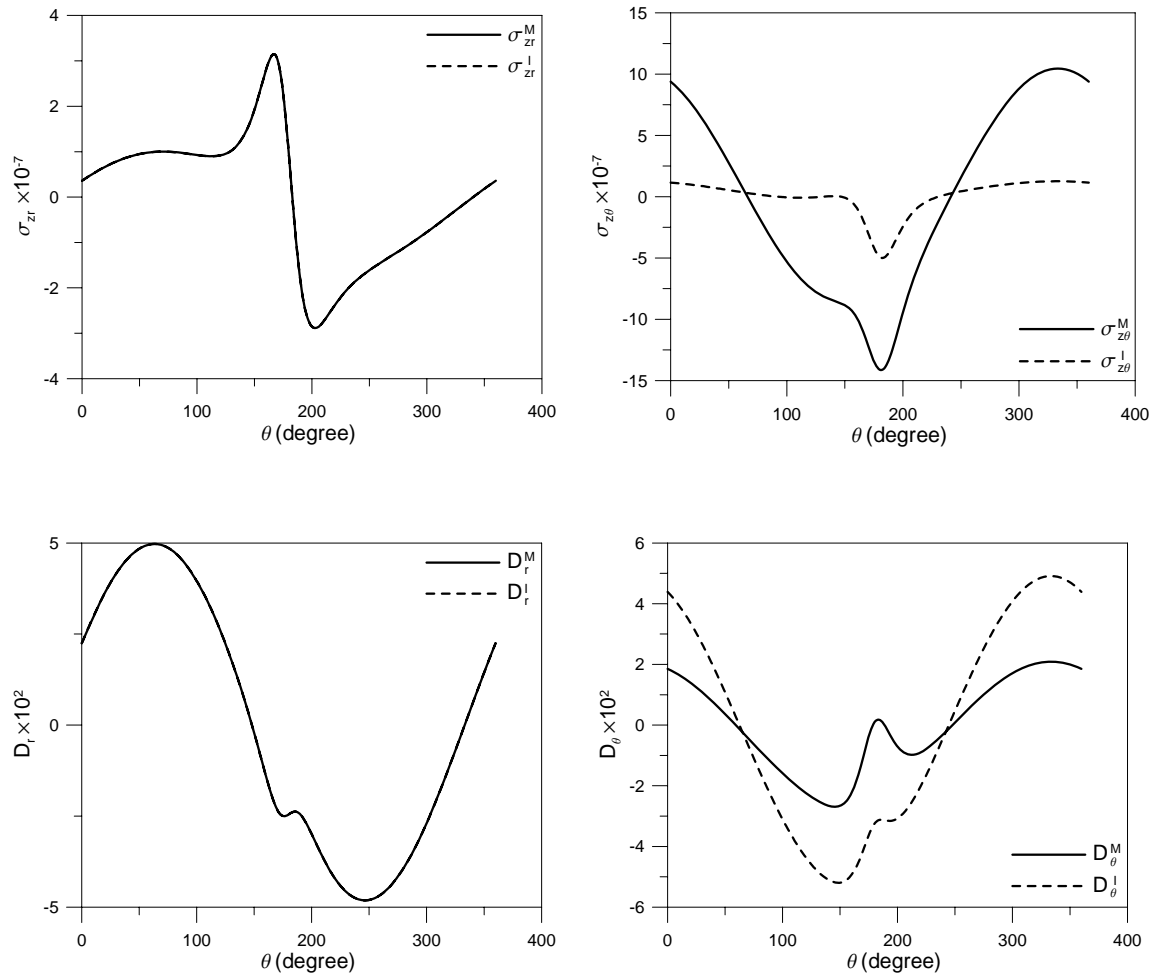
Figure 3-15 Stress and electric displacement distributions along the interface between the matrix and the larger inclusion
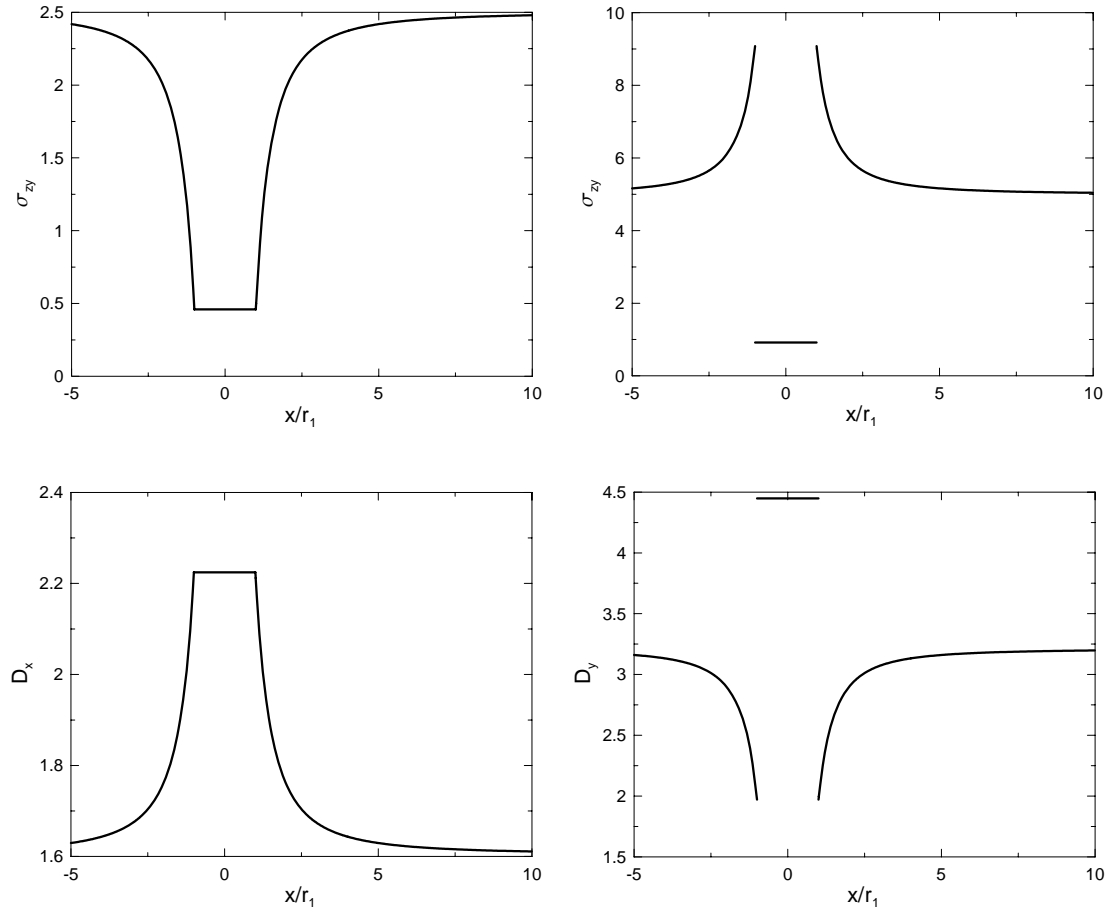
Figure 3-16 Stress and electric displacement distributions along the x axis for the case when the larger inclusion and the matrix have the same material property
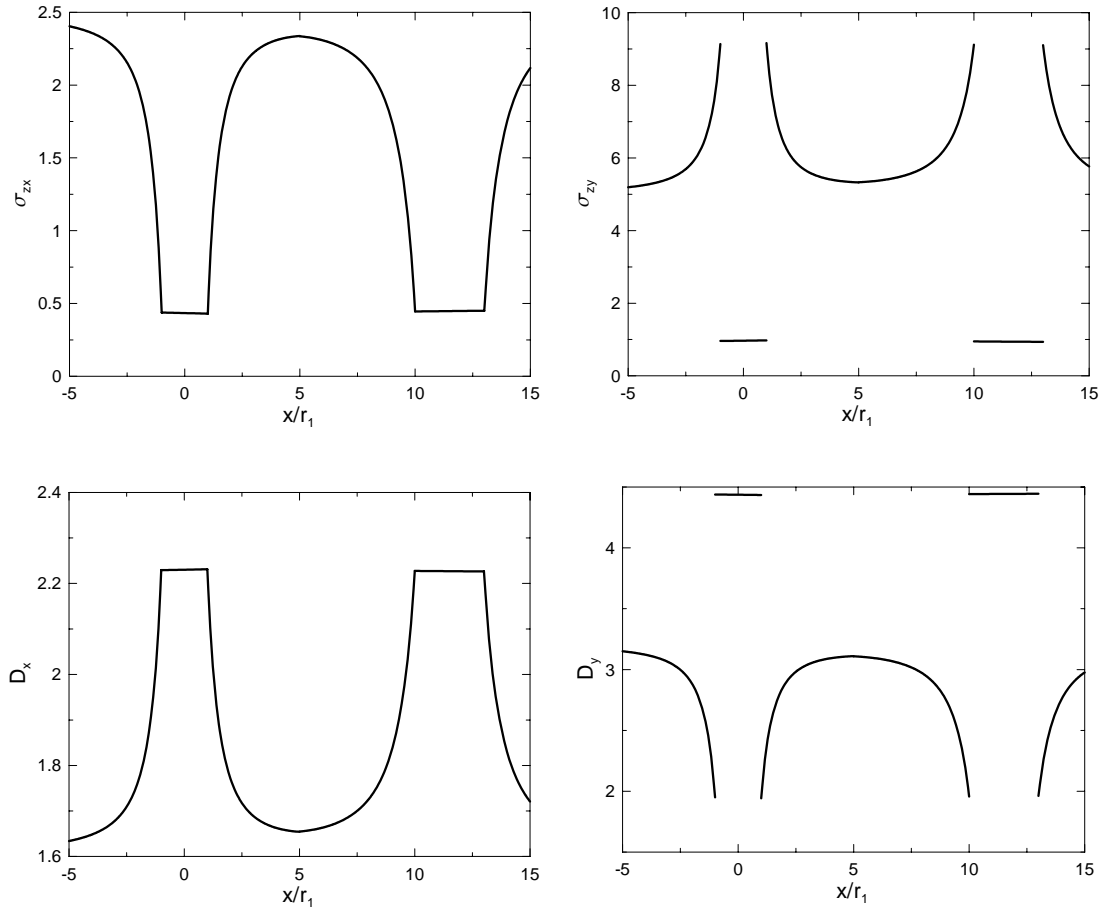
Figure 3-17 Stress and electric displacement distributions along the x axis for the case when the two inclusions are separated far away ($d/r_1 = 10$)
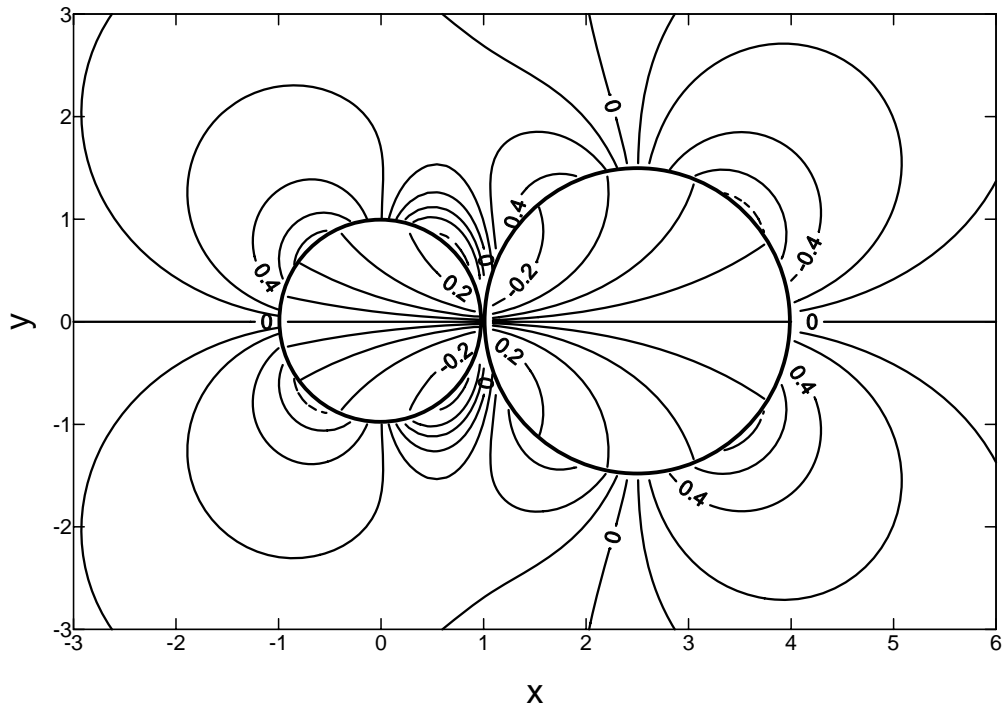
Figure 3-18 (a) Contour of shear stress σ_{zx}/τ_∞ when $d/r_1 = 0.01$
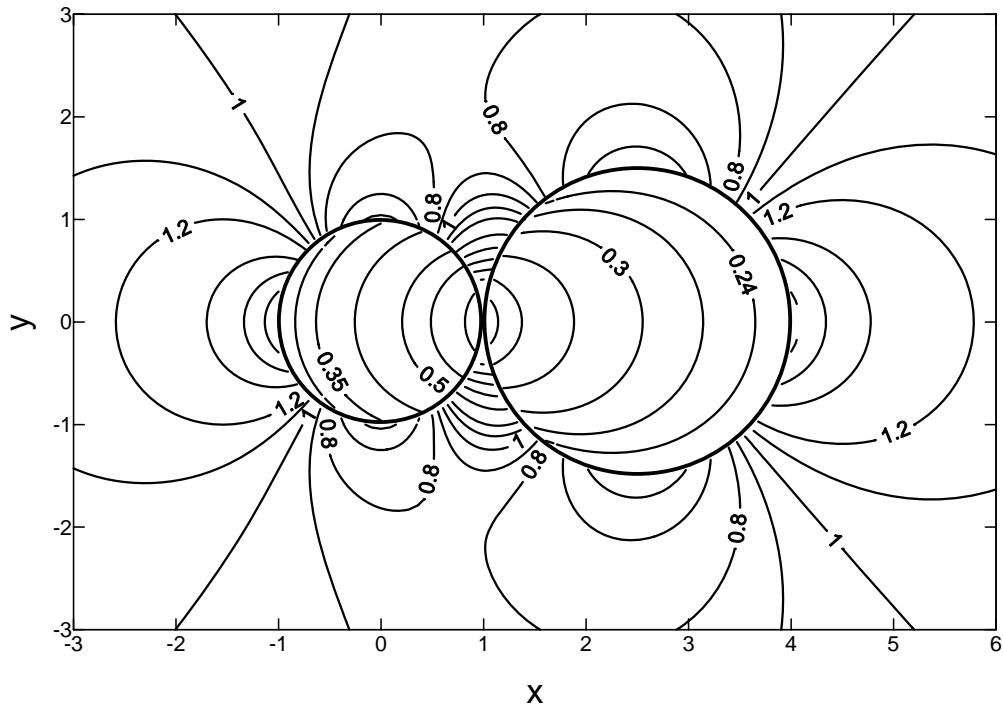
Figure 3-18 (b) Contour of shear stress σ_{zy}/τ_∞ when $d/r_1 = 0.01$
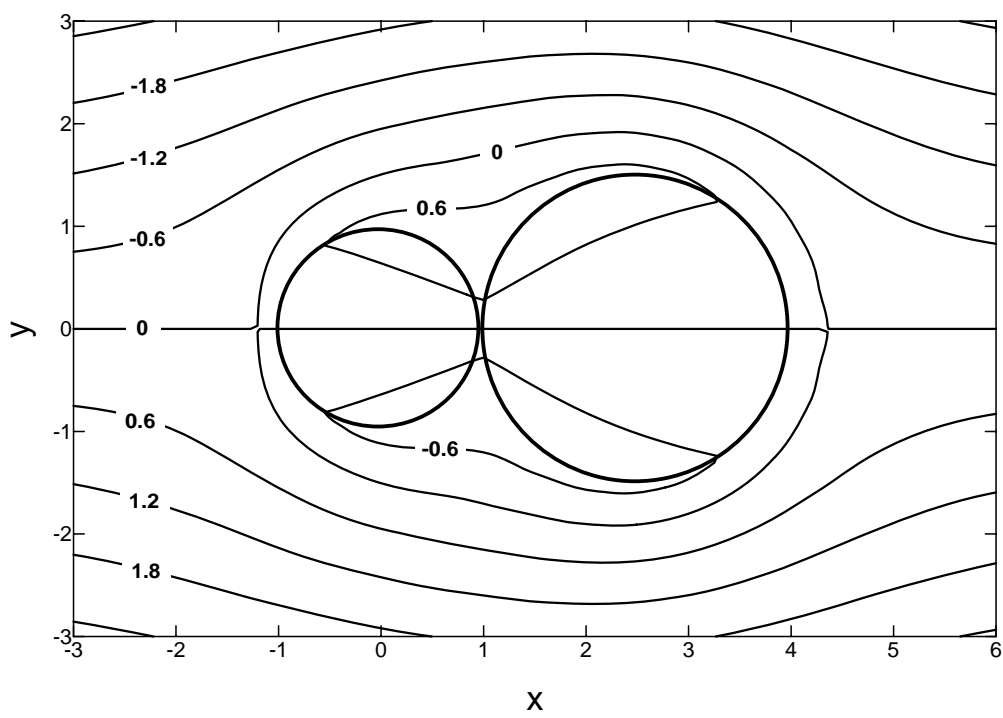
Figure 3-18 (c) Contour of electric potential Φ / E_∞ when $d / r_1 = 0.01$
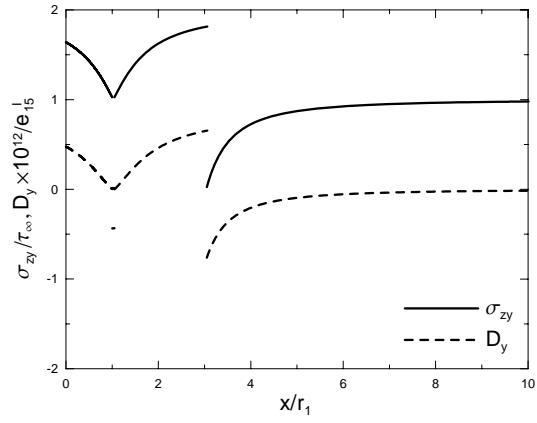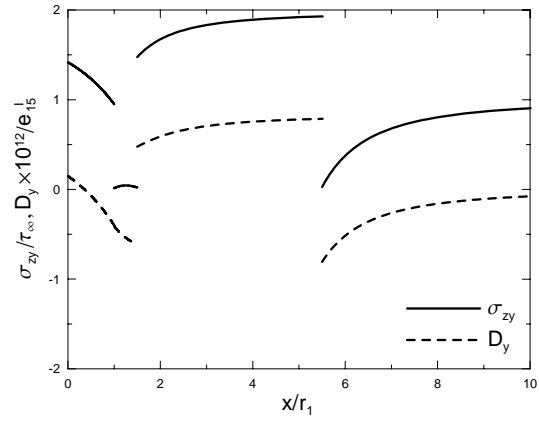
Figure 3-19 (a) Stress and electric displacement distributions along the x axis when $r_1 = r_2$ and $d = 0.05r_1$
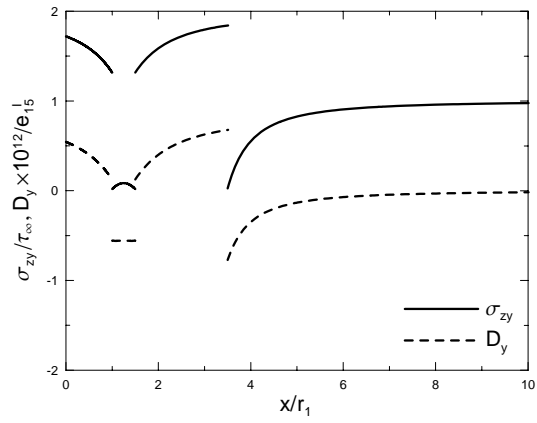
Figure 3-19 (b) Stress and electric displacement distributions along the x axis when $r_1 = r_2$ and $d = 0.5r_1$
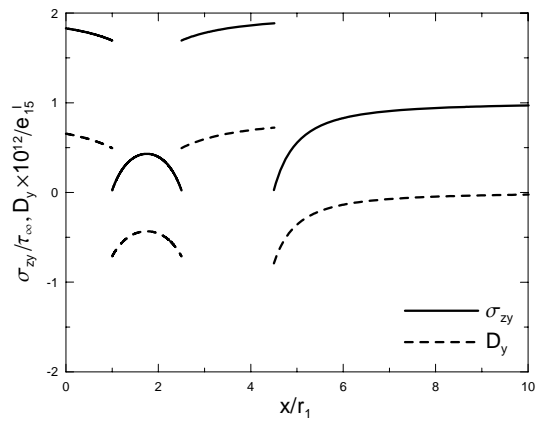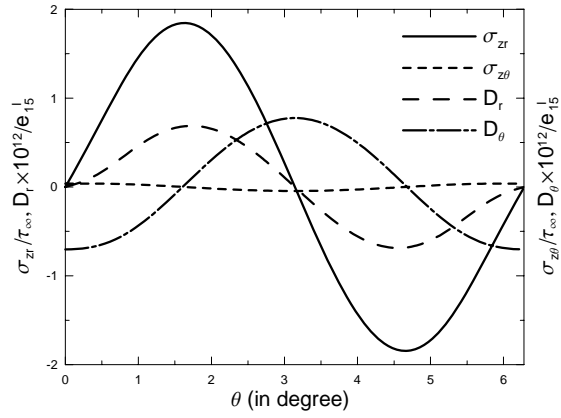

Figure 3-19 (c) Stress and electric displacement distributions along the x axis when $r_1 = r_2$ and $d = 1.5r_1$

Figure 3-20 (a) Stress and electric displacement distributions along the x axis when $r_2 = 2r_1$ and $d = 0.5r_1$

Figure 3-20 (b) Stress and electric displacement distributions along the contour $(1.01, \theta)$ when $r_1 = r_2$ and $d = 1.5r_1$
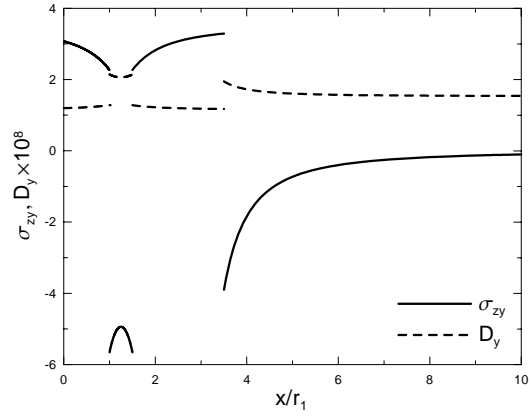
Figure 3-21 (a) Stress and electric displacement distributions along the x axis when $E_y^\infty = E_\infty$, $r_1 = r_2$ and $d = 0.5r_1$
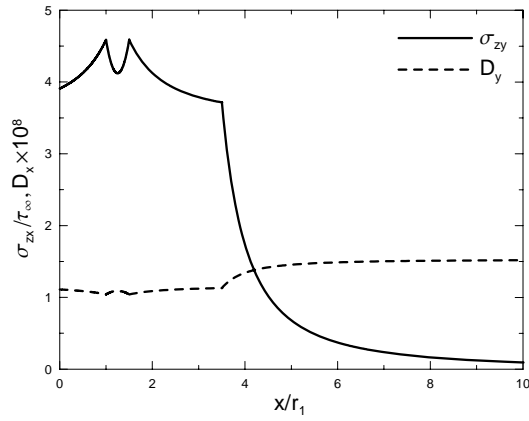

Figure 3-21 (b) Stress and electric displacement distributions along the x axis when $E_x^\infty = E_\infty$, $r_1 = r_2$ and $d = 0.5r_1$
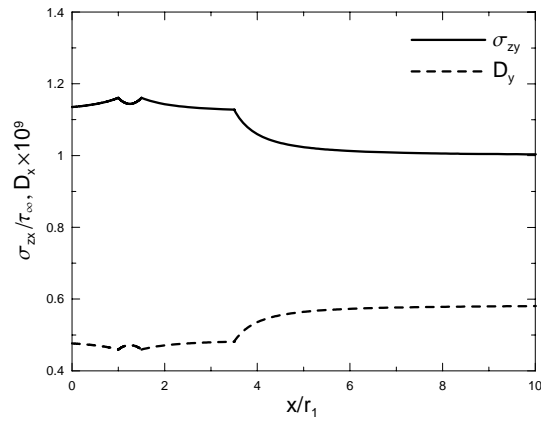

Figure 3-21 (c) Stress and electric displacement distributions along the x axis when $\sigma_{zx}^\infty = \tau_\infty$, $r_1 = r_2$ and $d = 0.5r_1$
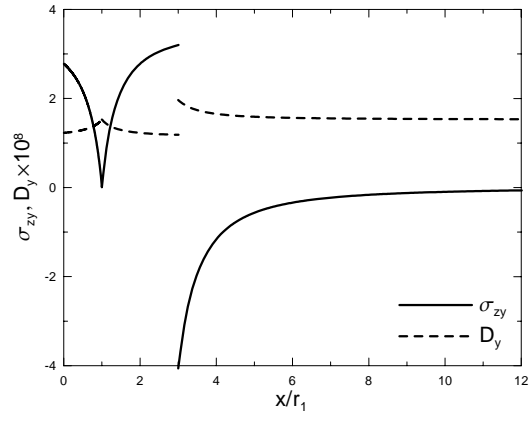
Figure 3-22 (a) Stress and electric displacement distributions along the x axis when two inclusions touch each other and $E_y^\infty = E_\infty$, $r_1 = r_2$
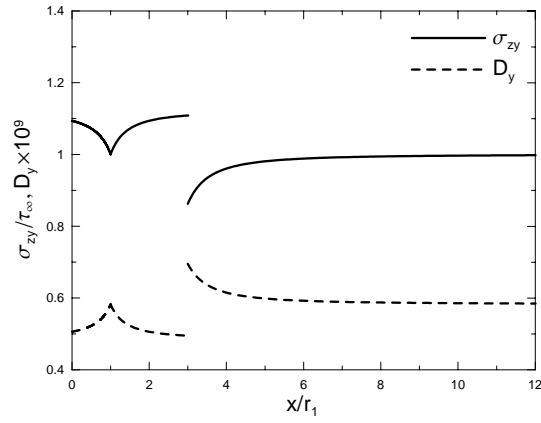

Figure 3-22 (b) Stress and electric displacement distributions along the x axis when two inclusions touch each other and $\sigma_{zy}^\infty = \tau_\infty$, $r_1 = r_2$
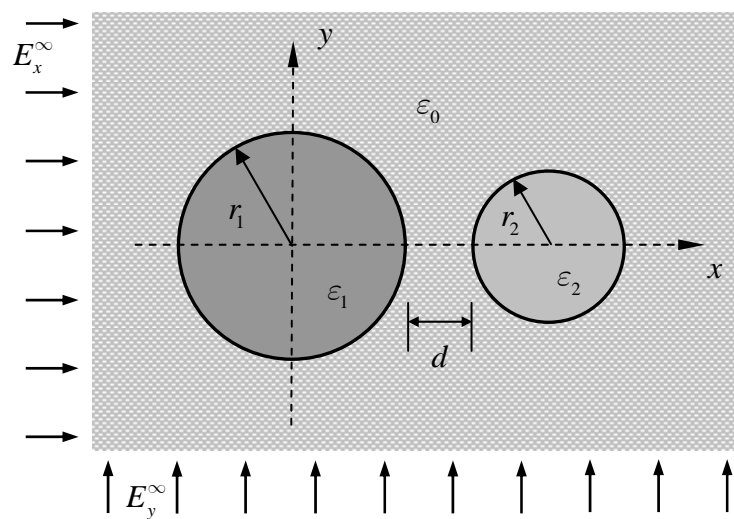
Figure 3-23 The dielectric system of two inclusions in the applied electric field

$$E_x^\infty = E_\infty$$

$$E_x^\infty = E_\infty \cos 45° \quad \text{and} \quad E_y^\infty = E_\infty \sin 45°$$
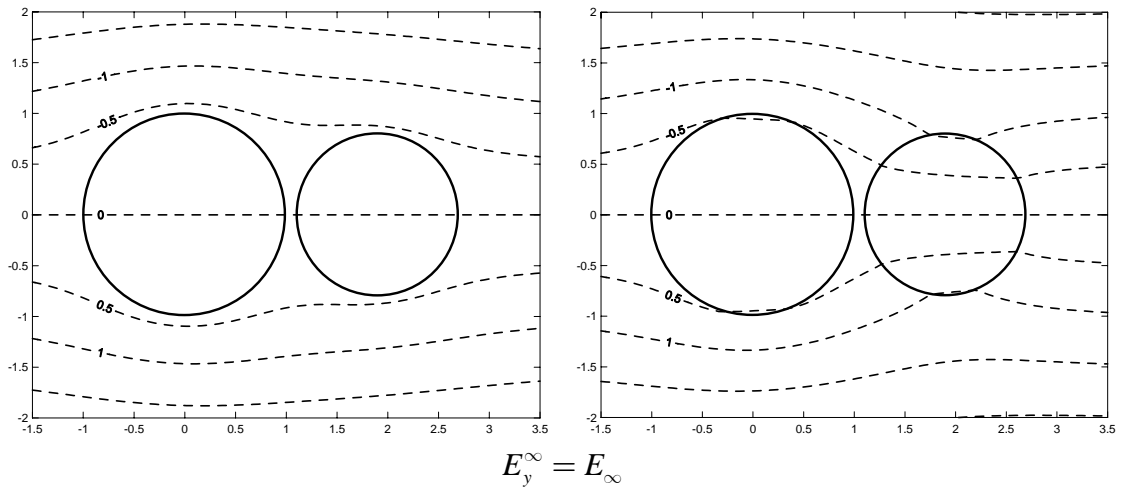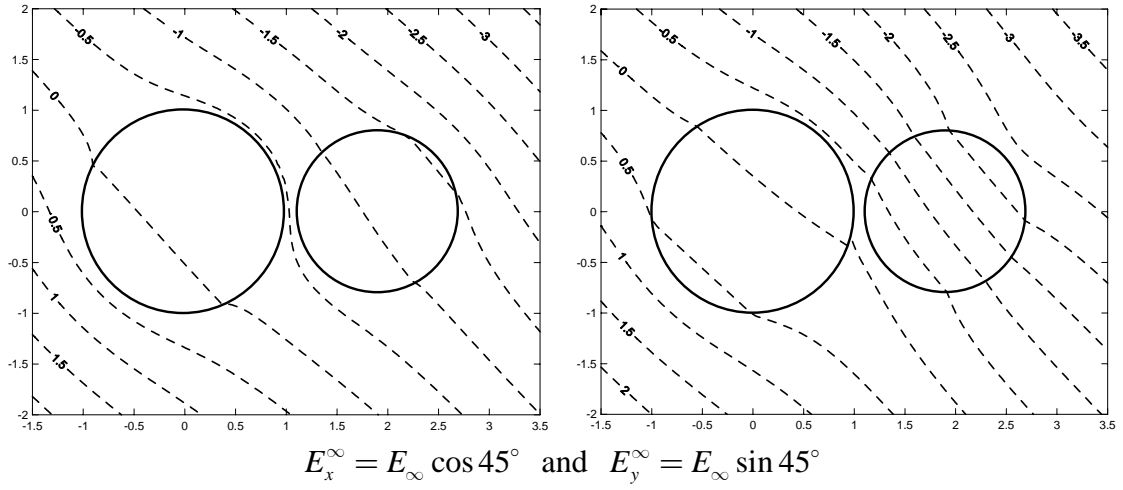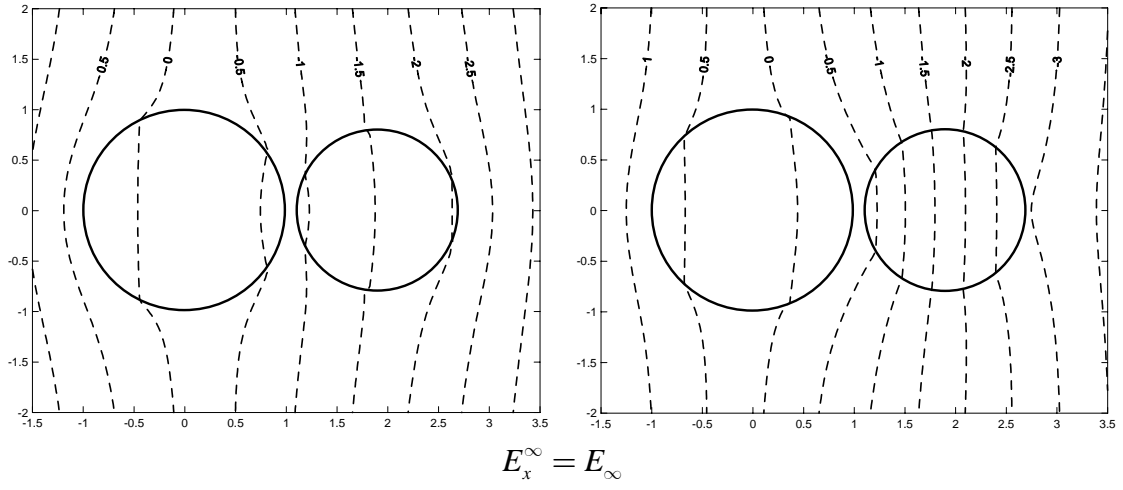

$$E_y^\infty = E_\infty$$

Figure 3-24 (a) Patterns of the electric field for $\varepsilon_0 = 2$, $\varepsilon_1 = 9$ and $\varepsilon_2 = 5$

Figure 3-24 (b) Patterns of the electric field for $\varepsilon_0 = 3$, $\varepsilon_1 = 9$ and $\varepsilon_2 = 1$

Chapter 4 Applications to anti-plane elasticity problems with circular inclusions

Summary

In this chapter, we apply the null-field integral equation to solve an infinite medium containing circular holes and/or inclusions with arbitrary radii and positions under the remote anti-plane shear. The method is basically a numerical method, and because of its semi-analytical nature, it possesses certain advantages over the conventional boundary element method. The exact solution for a single inclusion is revisited using the present formulation and matches well with the Honein *et al.*'s solution by using the complex-variable formulation. Several problems of two holes, two inclusions, one cavity surrounded by two inclusions and three inclusions are examined to demonstrate the validity of our method. Besides, the convergence test and boundary-layer effect for the present method and conventional boundary element method are also addressed to show the validity of the present approach. The proposed formulation can be generalized to multiple circular inclusions and cavities in a straightforward way without any difficulty.

4.1 Introduction

The distribution of stress in an infinite medium containing circular holes and/or inclusions under the remote anti-plane shear has been studied by many investigators. However, analytical solutions are rather limited except for simple cases. To the author's best knowledge, an exact solution of a single inclusion was derived by Honein *et al.* [56] using the complex potential formulation. Besides, analytical solutions for two identical holes and inclusions were obtained by Stief [82] and by Budiansky and Carrier [15], respectively. Zimmerman [98] employed the Schwartz alternative method for plane problems with two holes or inclusions to obtain a closed-form solution. In addition, Sendeckyj [76] proposed an iterative scheme for solving problems of multiple inclusions. However, the approach is rather complicated and explicit solutions were not

provided. Numerical solutions for problems with two unequal holes and/or inclusions were provided by Honein *et al.* [56] using the Möbius transformations involving the complex potential. Not only anti-plane shears but also screw dislocations were considered. Numerical results were presented by Goree and Wilson [50] for an infinite medium containing two inclusions under the remote shear. Bird and Steele [12] used a Fourier series procedure to revisit the anti-plane elasticity problems of Honein *et al.*'s paper [56]. To approximate the Honein *et al.*'s problem of infinite domain, an equivalent bounded-domain approach with the stress applied on the outer boundary was utilized. A shear stress σ_{zr} on the outer boundary is used in place of a stress σ_{zy} at infinity to approach the Honein *et al.*'s results as the radius becomes large. Wu [94] solved the analytical solution for two inclusions under the remote shear in two directions by using the conformal mapping and the theorem of analytic continuation. Based on the technique of analytical continuity and the method of successive approximation, Chao and Young [22] studied the stress concentration on a hole surrounded by two inclusions. For a triangle pattern of three inclusions, Gong [48] employed the complex potential and Laurent series expansion to calculate the stress concentration. Complex variable boundary element method (CVBEM) was utilized to deal with the problem of two circular holes by Chou [43] and Ang and Kang [1], independently. To provide a general solution to the anti-plane interaction among multiple circular inclusions with arbitrary radii, shear moduli and location is not trivial. Mathematically speaking, only circular boundaries in an infinite domain are concerned here. Mogilevskaya and Crouch [71] have also employed Fourier series expansion technique and used the Galerkin method instead of collocation technique to solve the problem of circular inclusions in 2-D elasticity. The advantage of their method is that one can tackle a lot of inclusions even inclusions touching one another. However, they did not expand a fundamental solution into a degenerate kernel in the polar coordinate. Another disadvantage is that their method can not reduce to cavity problems using the formulation for inclusions, as quoted by Mogilevskaya's Group, "*This approach, however, could not simply treat a hole as a limiting case of an inclusion with zero elastic properties. This is because, for the problem of a hole, the tractions are usually*

prescribed on the hole boundary and, *this problem is therefore governed by a different boundary integral equation - a complex hypersingular equation written in terms of unknown displacement*." Our formulation can treat cavity problems as a limiting case of inclusion problems with zero elastic properties. Chen and his coworkers [36, 38] have successfully solved the anti-plane problem with circular holes and/or inclusions using the null-field integral equation in conjunction with the degenerate kernel and Fourier series. The extension to biharmonic problems was also implemented [29].

By introducing a multi-domain approach, an inclusion problem can be decomposed into two parts. One is the infinite medium with circular holes and the other is the problem with each circular inclusion. After considering the continuity and equilibrium conditions on the interface between the matrix and inclusion, a linear algebraic system is obtained and the unknown Fourier coefficients can be determined. Then, the field potential and stress are easily obtained. Furthermore, an arbitrary number of circular inclusions can be treated by using the present method without any difficulty. One must take care the vector decomposition in using the adaptive observer system for the nonconfocal case. Also, the boundary stress is easily determined by using series sums instead of employing the sense of Hadamard principal value. A general-purpose program for arbitrary number of circular inclusions with various radii, arbitrary positions and shear moduli was developed. The infinite medium with multiple circular holes [36] can be solved as a limiting case of zero shear modulus of inclusions by using the developed program. Several examples solved previously by other researchers [15, 22, 48, 50, 56, 82, 94] were revisited to see the accuracy and efficiency of the present formulation. In addition, the test of convergence is done and the boundary-layer effect for the calculations of stresses is also addressed.

4.2 Problem statements and mathematical formulation

The displacement field of the anti-plane deformation is defined as:

$$u = v = 0, \quad w = w(x, y), \tag{4-1}$$

where w is the only nonvanishing component of displacement with respect to the Cartesian coordinate which is a function of x and y. For a linear elastic body, the

stress components are

$$\sigma_{zx} = \mu \frac{\partial w}{\partial x}, \tag{4-2}$$

$$\sigma_{zy} = \mu \frac{\partial w}{\partial y}, \tag{4-3}$$

where μ is the shear modulus. The equilibrium equation can be simplified to

$$\frac{\partial \sigma_{zx}}{\partial x} + \frac{\partial \sigma_{zy}}{\partial y} = 0. \tag{4-4}$$

Thus, we have

$$\frac{\partial^2 w}{\partial x^2} + \frac{\partial^2 w}{\partial y^2} = \nabla^2 w = 0. \tag{4-5}$$

Equation (4-5) indicates that the governing equation of this problem is the Laplace equation. For the stress field described in the polar coordinate, it also follows the anti-plane shear deformation in Table 3-1 or can be superimposed by σ_{zx} and σ_{zy} in Eqs. (4-2) and (4-3) as

$$\sigma_{zr} = \sigma_{zx} \cos\phi + \sigma_{zy} \sin\phi, \tag{4-6}$$

$$\sigma_{z\theta} = -\sigma_{zx} \sin\phi + \sigma_{zy} \cos\phi, \tag{4-7}$$

where σ_{zr} and $\sigma_{z\theta}$ are the normal and tangential stresses, respectively. Here, we consider an infinite medium subject to N circular inclusions bounded by the B_k contour ($k = 1, 2, \cdots, N$) for either the matrix or inclusions under the anti-plane shear σ_{zx}^{∞} and σ_{zy}^{∞} at infinity or equivalently under the displacement $w^{\infty} = \sigma_{zx}^{\infty} x / \mu + \sigma_{zy}^{\infty} y / \mu$ at infinity as shown in Fig. 4-1 (a). By taking the free body along the interface between the matrix and inclusions, the problem can be decomposed into two systems. One is an infinite medium with N circular holes under the remote shear and the other is N circular inclusions bounded by the B_k contour which satisfies the Laplace equation as shown in Figs. 4-1 (b) and 4-1 (c), respectively. From the numerical point of view, this is the so-called multi-domain approach. For the problem in Fig. 4-1 (b), it can be superimposed by two parts. One is an infinite medium under the remote shear and the other is an infinite medium with N circular holes which satisfies the Laplace equation as shown in Figs. 4-1 (d) and 4-1 (e), respectively.

This part was solved efficiently by Chen *et al.* [36] using the null-field equation approach which is adapted here again. Therefore, one exterior problem for the matrix is shown in Fig. 4-1 (e) and several interior problems for nonoverlapping inclusions are shown in Fig. 4-1 (c). According to the null-field integral formulation, the two problems in Figs. 4-1 (e) and 4-1 (c) can be solved in a unified manner since they both satisfy the Laplace equation.

4.3 Matching of interface conditions and solution procedures

After decomposing the inclusion problems into two parts, we employ the null-field approach to handle one exterior Laplace problem for the matrix as shown in Fig. 4-1 (e) and several interior Laplace problems for nonoverlapping inclusions as shown in Fig. 4-1 (c). By collocating the null-field point on the boundary, the linear algebraic system is obtained from Eq. (2-22).

For the exterior problem of matrix in Fig. 4-1 (e), we have

$$\left[\mathbf{U}^M\right]\left\{\mathbf{t}^M - \mathbf{t}^\infty\right\} = \left[\mathbf{T}^M\right]\left\{\mathbf{w}^M - \mathbf{w}^\infty\right\}. \tag{4-8}$$

For the interior problem of each inclusion in Fig. 4-1 (c), we have

$$\left[\mathbf{U}^I\right]\left\{\mathbf{t}^I\right\} = \left[\mathbf{T}^I\right]\left\{\mathbf{w}^I\right\}, \tag{4-9}$$

where the superscripts "M" and "I" denote the matrix and inclusion, respectively. The degenerate kernels $\left[\mathbf{U}^M\right]$, $\left[\mathbf{T}^M\right]$, $\left[\mathbf{U}^I\right]$ and $\left[\mathbf{T}^I\right]$ and Fourier series $\left\{\mathbf{w}^M\right\}$, $\left\{\mathbf{t}^M\right\}$, $\left\{\mathbf{w}^\infty\right\}$, $\left\{\mathbf{t}^\infty\right\}$, $\left\{\mathbf{w}^I\right\}$ and $\left\{\mathbf{t}^I\right\}$ employed in the null-field equation can be found in Chapter 2. It is noted that $\left\{\mathbf{w}^\infty\right\}$ and $\left\{\mathbf{t}^\infty\right\}$ in Fig. 4-1 (d) are the displacement and traction field due to the remote shear, respectively.

According to the continuity of displacement and equilibrium of traction along the *kth* interface, we have the two constraints

$$\left\{\mathbf{w}^M\right\} = \left\{\mathbf{w}^I\right\} \quad \text{on} \quad B_k, \tag{4-10}$$

$$\left[\boldsymbol{\mu}_0\right]\left\{\mathbf{t}^M\right\} = -\left[\boldsymbol{\mu}_k\right]\left\{\mathbf{t}^I\right\} \quad \text{on} \quad B_k, \tag{4-11}$$

where $\left[\boldsymbol{\mu}_0\right]$ and $\left[\boldsymbol{\mu}_k\right]$ are defined as follows:

$$
[\boldsymbol{\mu}_0] = \begin{bmatrix} \mu_0 & 0 & \cdots & 0 \\ 0 & \mu_0 & \cdots & 0 \\ \vdots & \vdots & \ddots & \vdots \\ 0 & 0 & \cdots & \mu_0 \end{bmatrix}, \quad [\boldsymbol{\mu}_k] = \begin{bmatrix} \mu_k & 0 & \cdots & 0 \\ 0 & \mu_k & \cdots & 0 \\ \vdots & \vdots & \ddots & \vdots \\ 0 & 0 & \cdots & \mu_k \end{bmatrix}, \tag{4-12}
$$

where μ_0 and μ_k denote the shear modulus of the matrix and the *kth* inclusion, respectively. By assembling the matrices in Eqs. (4-8) ~(4-11), we have

$$
\begin{bmatrix} \mathbf{T}^M & -\mathbf{U}^M & \mathbf{0} & \mathbf{0} \\ \mathbf{0} & \mathbf{0} & \mathbf{T}^I & -\mathbf{U}^I \\ \mathbf{I} & \mathbf{0} & -\mathbf{I} & \mathbf{0} \\ \mathbf{0} & \boldsymbol{\mu}_0 & \mathbf{0} & \boldsymbol{\mu}_k \end{bmatrix} \begin{Bmatrix} \mathbf{w}^M \\ \mathbf{t}^M \\ \mathbf{w}^I \\ \mathbf{t}^I \end{Bmatrix} = \begin{Bmatrix} \mathbf{c} \\ \mathbf{0} \\ \mathbf{0} \\ \mathbf{0} \end{Bmatrix}, \tag{4-13}
$$

where $\{\mathbf{c}\}$ is the forcing term due to the remote shear stress and $[\mathbf{I}]$ is the identity matrix. The calculation for the vector $\{\mathbf{c}\}$ is elaborated on later in Appendix 2. After obtaining the unknown Fourier coefficients in Eq. (4-13), the origin of observer system is set to c_k in the B_k integration as shown in Fig. 2-4 (b) to obtain the field potential by employing Eq. (2-11). In determining the stress and electric fields, the gradient of potential should be determined with care as shown in Section 2.4.3. The flowchart of the present method for anti-plane elasticity problems is shown in Table 4-1.

Except the foregoing formulation, one can also treat the anti-plane shear deformation as a limiting case of the anti-plane piezoelectricity problems when the coupled effect between the mechanical and electrical fields is absent or the piezoelectric constant are equal to zero. It is obvious to observe that the resulted linear algebraic system in Eq. (4-13) can be obtained from Eq. (3-19) after taking off the influence terms of the coupling parts.

4.4 Illustrative examples and discussions

First, we derive an exact solution for a single inclusion using the present formulation in Appendix 3. Symbolic software of Mathematica is employed to solve a $2L+1$ by $2L+1$ sparse matrix by using the induction concept. Then, seven problems solved by previous scholars are revisited by using the present method to show the generality and

85

validity of our formulation. Besides, we demonstrate the problem of interaction of two cavities in Case 1 to compare the present method with the conventional BEM.

Case 1: Two equal-sized holes lying on the x axis (a limiting case)

Figure 4-2 (a) shows the geometry of two equal-sized holes in the infinite medium under the remote shear $\sigma_{zy}^{\infty} = \tau_{\infty}$. The stress concentration of the problem is illustrated in Fig. 4-2 (b). It indicates that the present result agrees well with the analytical solution of Steif [82] and those obtained by Chao and Young [22] even though the two holes approach each other. Figure 4-2 (c) shows that only few terms of Fourier series can obtain good results. However, more nodes are required by using the conventional BEM to achieve convergence. Our formulation is free of boundary-layer effect instead of appearance by using the conventional BEM when the stress $\sigma_{z\theta}$ near the boundary as shown in Fig. 4-2 (d). Stress concentration factors and errors for various distances between two holes by using the present method and the conventional BEM are listed in Table 4-2. These results show that the present method is more accurate and effective than those of the conventional BEM. Under the same error tolerance, the CPU time of the present method is fewer than that of the conventional BEM. Besides, it is noted that more terms of Fourier series are required to capture the singular behavior when the two holes approach each other.

Case 2: Two identical inclusions locating on the x axis

We consider two identical elastic inclusions of radii $r_1 = r_2$ and shear moduli $\mu_1 = \mu_2$ embedded in an infinite medium subjected to the remote shear $\sigma_{zx}^{\infty} = \tau_{\infty}$ at infinity [15] as shown in Fig. 4-3 (a). Figure 4-3 (b) shows that stress concentration factor diminishes when the inclusion spacing increases. We note that the mathematical model of rigid-inclusion problem is equivalent to that of uniform potential flow past two parallel cylinders with no circulation around either cylinder. The remote shear $\sigma_{zx}^{\infty} = \tau_{\infty}$ is similar to the velocity V_{∞} in the x direction at infinity and the velocity field is similar to the stress field [66].

Case 3: Two circular inclusions locating on the x axis

Two inclusions with radii of r_1 and r_2 under the remote shear are considered in Fig. 4-4 (a). The stress distributions in the matrix including the radial component σ_{zr} and the tangential component $\sigma_{z\theta}$ around the circular boundary of radius r_1 are plotted in Figs. 4-4 (b) and 4-4 (c) for various inclusion spacings when the two inclusion radii are equal-sized ($r_1 = r_2$). Two limiting cases are considered for rigid inclusions ($\mu_1 / \mu_0 = \mu_2 / \mu_0 = \infty$, 10^6 in the real computation) and for cavities ($\mu_1 / \mu_0 = \mu_2 / \mu_0 = 0.0$). It can be found that $\sigma_{z\theta} = 0$ or $\sigma_{zr} = 0$ for rigid inclusions or cavities as predicted for the single inclusion or cavity, respectively. Moreover, the nonzero stress components for these two cases are identical when the stress components at infinity are interchanged, *i.e.* the stresses around the circular boundary σ_{zr} in one case equals to $\sigma_{z\theta}$ for the other case due to the analogy of mathematical model. It can be seen from Figs. 4-4 (b) and 4-4 (c) that unbounded stress apparently occurs at $\theta = 180°$ under the condition of $\sigma_{zx}^\infty = \tau_\infty$ for rigid inclusions or $\sigma_{zy}^\infty = \tau_\infty$ for cavities when two inclusions approach closely or even touch each other. In Figs. 4-4 (d) and 4-4 (e), the variation of stresses around the circular boundary of radius r_1 is shown versus radius r_2 for a fixed separation of $d = 0.1 r_1$. More terms of Fourier series are required to capture the singular behavior when the two inclusions approach each other as well as the two radii of inclusions are quite different. The present results match very well with those by Goree and Wilson [50].

Case 4: Two circular inclusions locating on the y axis

The infinite medium with two elastic inclusions is under the uniform remote shear $\sigma_{zy}^\infty = \tau_\infty$. The first inclusion centered at the origin of radius r_1 with the shear modulus $\mu_1 = 2\mu_0 / 3$ and the other inclusion of radius $r_2 = 2r_1$ centered on y axis at $r_1 + r_2 + d$ ($d = 0.1 r_1$) with the shear modulus $\mu_2 = 13\mu_0 / 7$ are shown in Fig. 4-5 (a). In order to be compared with the Honein *et al.*'s data obtained by using the Möbius transformations [56], the stresses along the boundary of radius r_1 is shown in Fig. 4-5 (b). It satisfies the equilibrium traction along the interface of circular boundary. The stress concentration factor reaches maximum at $\theta = 0°$ in the matrix. Figure 4-5 (c)

shows that only few terms of Fourier series can also yield acceptable results. Figures 4-5(d) and 4-5 (e) indicates that our formulation is free of boundary-layer effect since stresses σ_{zr} and $\sigma_{z\theta}$ near the boundary can be smoothly predicted, respectively. The key to eliminate the boundary-layer effect is that we introduce the degenerate kernel to describe the jump behavior for potential in interior and exterior regions as shown in Table 2-2.

Case 5: Two inclusions locating on the x axis under the two-direction shears

In Fig. 4-6 (a), the parameters used in the calculation are taken as $r_1 = r_2$, $\sigma_{zx}^\infty = \sigma_{zy}^\infty = \tau_\infty$, $\mu_0 = 0.185$ and $\mu_1 = \mu_2 = 4.344$. Figure 4-6 (b) shows stress distributions σ_{zx} and σ_{zy} along the x axis when $d = 0.1$. It can be seen that the stress component σ_{zx} is continuous across the interface between two different materials and has a peak value between two inclusions. The stress component σ_{zy} is discontinuous across the interface of two different materials. Figures 4-6 (c) and 4-6 (d) illustrate stress distributions of σ_{zx} and σ_{zy} along the x axis when $d = 0.4$ and $d = 1.0$, respectively. Both figures indicate that stress components of σ_{zx} and σ_{zy} have similar changing curves to those of Fig. 4-6 (b). However, it should be noted that the maximum value of stress component σ_{zx} drops when the distance d between the two inclusions increases. Figure 4-6 (e) illustrates the normal stress distributions σ_{zr} along the contour $(1.001, \theta)$ for various cases of $d = 0.1$, 0.5 and 1.0. It shows that the shear stress σ_{zr} increases as the distance d between the two inclusions decreases at the point where two inclusions approach each other. However, the distance d has a slight effect on σ_{zr} when the angle is in the range of $90° < \theta < 320°$. Figure 4-6 (f) illustrates the tangential stress $\sigma_{z\theta}$ distributions along the contour $(1.001, \theta)$ for various distances of $d = 0.1$, 0.5 and 1.0. It should be noted that the absolute value of tangential stress $\sigma_{z\theta}$ is very small in comparison with that of σ_{zr}. Figure 4-6 (g) illustrates the variation of stress components σ_{zx} and σ_{zy} in the matrix at the point $(1.001, 0°)$ versus the distance d between the two inclusions. From the figure, it can be seen that stress components σ_{zx} and σ_{zy} become larger when the two inclusions approach each other. However, stress components σ_{zx} and σ_{zy} tend smoothly to the

constant when the two inclusions separate away. Figure 4-6 (h) shows stress distributions σ_{zx} and σ_{zy} along the x axis when the two inclusions touch each other. It can be seen that the shear stress σ_{zx} has a peak value at the touched point. For the increasing value of x, σ_{zx} tends to match the remote shear τ_{∞}. Besides, the stress component σ_{zy} is continuous at the tangent point ($x/r_1 = 1.0$) and has a discontinuous jump on the interface between the matrix and inclusion ($x/r_1 = 3.0$). The present results in Figs. 4-6 (b) ~4-6 (h) agree very well with the Wu's data [94]. Only the stress component σ_{zx} at the touched point is lower than the Wu's data as shown in Fig. 4-6 (h), since separate Fourier expansions on the two boundaries are described for the touched inclusions in our formulation.

Case 6: One hole surrounded by two circular inclusions

Figure 4-7 (a) shows that a circular hole centered at the origin of radius r_1 is surrounded by two circular inclusions ($d/r_1 = 1.0$) with the equal radius $r_2 = r_3 = 2r_1$ and equal shear modulus $\mu_2 = \mu_3$ under the remote shear $\sigma_{zx}^{\infty} = \tau_{\infty}$. We solved the distribution of the tangential stress along the circular hole influenced by the surrounding inclusions when they are arrayed in parallel ($\beta = 0°$) or perpendicular ($\beta = 90°$) to the direction of uniform shear as shown in Figs. 4-7 (b) and 4-7 (c). It is found that, when a hole and two inclusions are arrayed parallel to the applied load ($\beta = 0°$), the stress concentration factor, reaching maximum at $\theta = 90°$ along a circular hole, increases (or decreases) as the neighboring hard (or soft) inclusions approach a circular hole as shown in Figs. 4-7 (b) and 4-7 (d). On the contrary, when a hole and two inclusions are perpendicular to the applied load ($\beta = 90°$), the stress concentration factor, reaching maximum at $\theta = 90°$, decreases (or increases) as the neighboring hard (or soft) inclusions approach a circular hole as shown in Figs. 4-7 (c) and 4-7 (e). Our numerical results match very well with those of Chao and Young's [22].

Case 7: Three identical inclusions forming an equilateral triangle

Figure 4-8 (a) shows that three identical inclusions ($r_1 = r_2 = r_3$) subjected to the uniform shear stress $\sigma_{zy}^{\infty} = \tau_{\infty}$ at infinity. The three inclusions form an equilateral

triangle and are placed at a distance $4r_1$ apart. Besides, the distance between each two inclusions is $d = 2r_1$. We evaluate the hoop stress $\sigma_{z\theta}$ in the matrix around the boundary of the inclusion located at the origin as shown in Fig. 4-8 (b). Good agreement is obtained between the Gong's results [48] and ours. It is obvious that the limiting case of circular holes ($\mu_1/\mu_0 = \mu_2/\mu_0 = \mu_3/\mu_0 = 0.0$) leads to the maximum stress concentration at $\theta = 0°$, which is larger than 2 of a single hole due to the interaction effect. It is also interesting to note that the stress component $\sigma_{z\theta}$ vanishes in the case of rigid inclusions ($\mu_1/\mu_0 = \mu_2/\mu_0 = \mu_3/\mu_0 = \infty$, 10^6 in the real computation), which can be explained by a general analogy between solutions for traction-free holes and those involving rigid inclusions.

4.5 Concluding remarks

A semi-analytical formulation for multiple circular inclusions with arbitrary radii, moduli and locations using degenerate kernels and Fourier series in the adaptive observer system was developed to ensure the exponential convergence. Generally speaking, only ten terms of Fourier series ($L = 10$) can yield the acceptable and accurate results. More terms of Fourier series are required to capture the singular behavior when the two inclusions approach each other as well as the two radii of inclusions are quite different. The singularity and hypersingularity were avoided after introducing the concept of degenerate kernels for interior and exterior regions. Besides, the boundary-layer effect for the stress calculation near the boundary is eliminated since the degenerate kernel can clearly describe the jump behavior from interior to exterior domains. The exact solution for a single inclusion was also re-derived by using the present formulation. Several examples investigated by Steif, Budiansky and Carrier, Goree and Wilson, Honein *et al.*, Wu, Chao and Young, and Gong were revisited, respectively. Good agreements were made after comparing with the previous results. Regardless of the number, size and the position of circular inclusions and cavities, the proposed method can offer good results. This "semi-analytical" result may provide a datum for comparison when other numerical methods are used.

Table 4-1 Flowchart of the present method for anti-plane elasticity problems

```
┌──────────────────────────────────────────────────────┐
│          Laplace problem with circular boundaries      │
└──────────────────────────────────────────────────────┘
                            │
Analytical                  ▼
┌──────────────────────────────────────────────────────┐
│          Null-field integral equation in Eq. (2-22)    │
└──────────────────────────────────────────────────────┘
                            │
              ┌─────────────┴─────────────┐
              ▼                           ▼
┌──────────────────────────┐  ┌──────────────────────────┐
│   Fundamental solution    │  │   Boundary densities for   │
│  [Degenerate kernels are  │  │    circular boundaries     │
│   listed in Table 2-2]    │  │   [Fourier series in Eqs.  │
│                           │  │    (2-20) and (2-21)]      │
└──────────────────────────┘  └──────────────────────────┘
              └─────────────┬─────────────┘
                            ▼
┌──────────────────────────────────────────────────────┐
│     Adaptive observer system in the boundary integration │
└──────────────────────────────────────────────────────┘
                            │
                            ▼
┌──────────────────────────────────────────────────────┐
│  Collocating the null-field point to construct the compatible │
│  relationship among boundary data in Eqs. (4-8) and (4-9)     │
└──────────────────────────────────────────────────────┘
                            │
                            ▼
┌──────────────────────────────────────────────────────┐
│     Constructing influence coefficients in Table 2-2   │
└──────────────────────────────────────────────────────┘
                            │
                            ▼
┌──────────────────────────────────────────────────────┐
│  Assembling Eqs. (4-10) and (4-11) by using the continuity of │
│  displacement and equilibrium of traction along the interface │
└──────────────────────────────────────────────────────┘
                            │
Numerical                   ▼
┌──────────────────────────────────────────────────────┐
│          Linear algebraic system in Eq. (4-13)         │
└──────────────────────────────────────────────────────┘
                            │
                            ▼
┌──────────────────────────────────────────────────────┐
│     Obtain the unknown Fourier coefficients in Eq. (4-13) │
└──────────────────────────────────────────────────────┘
                            │
                            ▼
┌──────────────────────────────────────────────────────┐
│  Boundary integral equation for domain point in Eq. (2-11) │
└──────────────────────────────────────────────────────┘
                            │
                            ▼
┌──────────────────────────────────────────────────────┐
│              Vector decomposition technique            │
└──────────────────────────────────────────────────────┘
                            │
                            ▼
┌──────────────────────────────────────────────────────┐
│        Potential gradient for the stress field         │
└──────────────────────────────────────────────────────┘
```

Table 4-2 Stress concentration factors and errors for various distances between two holes using the present approach and BEM

		d / r_1	0.01	0.2	0.4	0.6	0.8	1.0
Stress concentration factor		Analytical solution [82]	14.2247	3.5349	2.7667	2.4758	2.3274	2.2400
	Present method	$L = 10$	10.5096 (26.12%)	3.5306 (0.12%)	2.7664 (0.01%)	2.4758 (0.00%)	2.3274 (0.00%)	2.2400 (0.00%)
		$L = 20$	13.3275 (6.31%)	3.5349 (0.00%)	2.7667 (0.00%)	2.4758 (0.00%)	2.3274 (0.00%)	2.2400 (0.00%)
	BEM BEPO2D	$node = 21$	7.2500 (49.03%)	3.4532 (2.31%)	2.738 (1.04%)	2.4639 (0.48%)	2.3168 (0.46%)	2.2366 (0.15%)
		$node = 41$	10.2008 (28.29%)	3.5188 (0.46%)	2.7619 (0.17%)	2.4747 (0.04%)	2.3312 (0.16%)	2.2398 (0.01%)

Data in parentheses denote error.
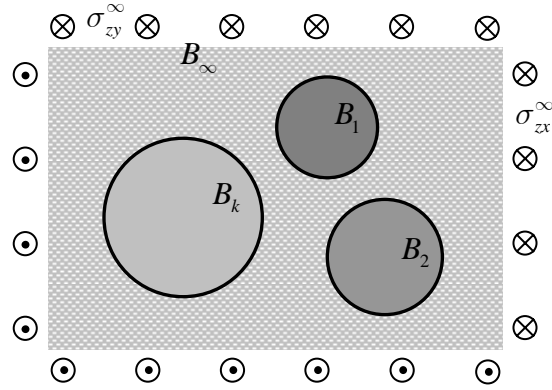
Figure 4-1 (a) Infinite anti-plane problem with arbitrary number of circular inclusions under the remote shear
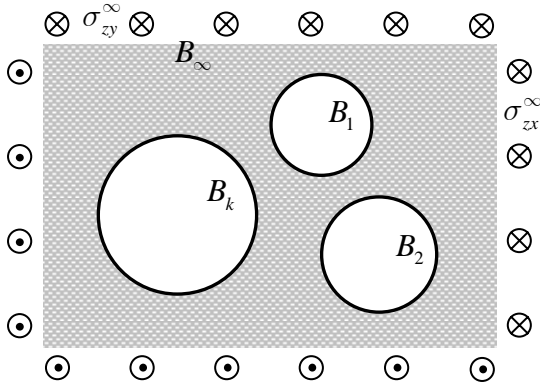
Figure 4-1 (b) Infinite medium with circular holes under the remote shear
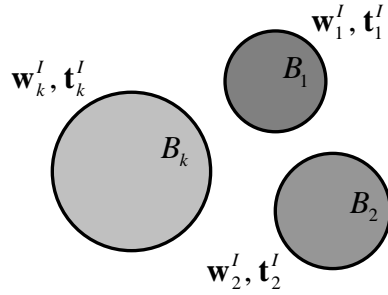
Figure 4-1 (c) Interior Laplace problems for each inclusion
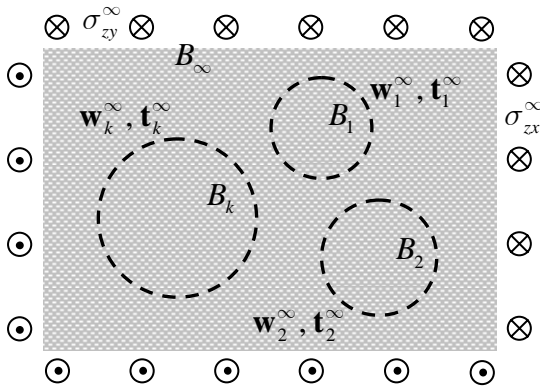
Figure 4-1 (d) Infinite medium under the remote shear
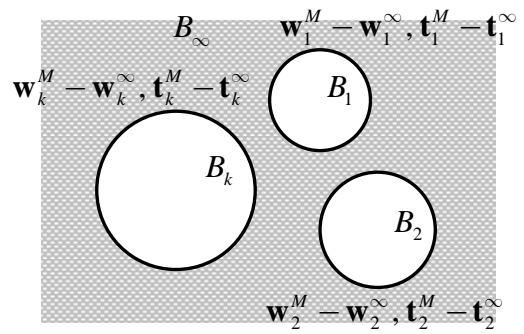
Figure 4-1 (e) Exterior Laplace problems for the matrix
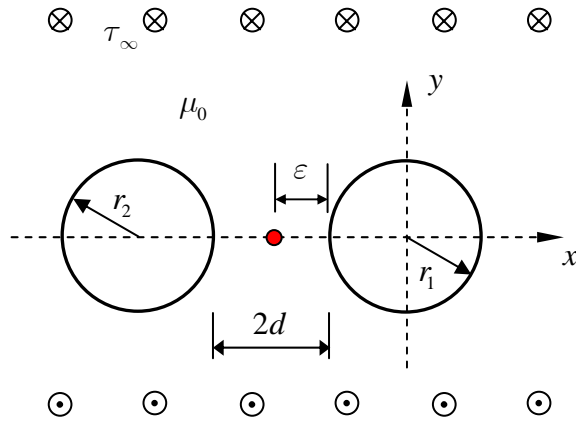
Figure 4-2 (a) Two equal-sized holes ($r_1 = r_2$) with centers on the x axis
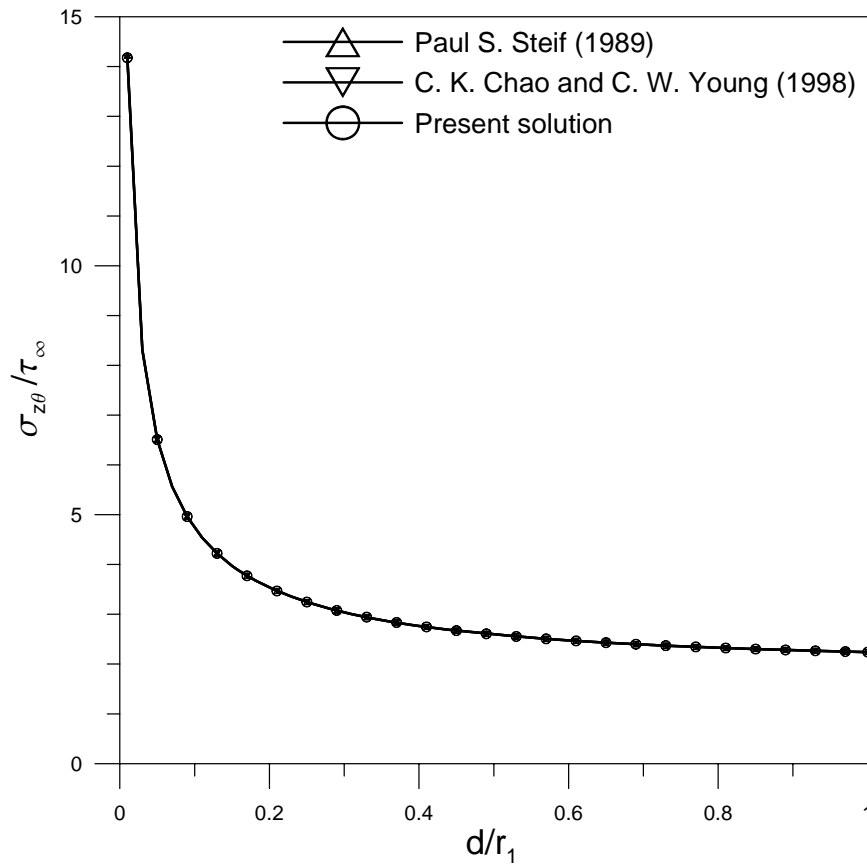
Figure 4-2 (b) Stress concentration of the problem containing two equal-sized holes
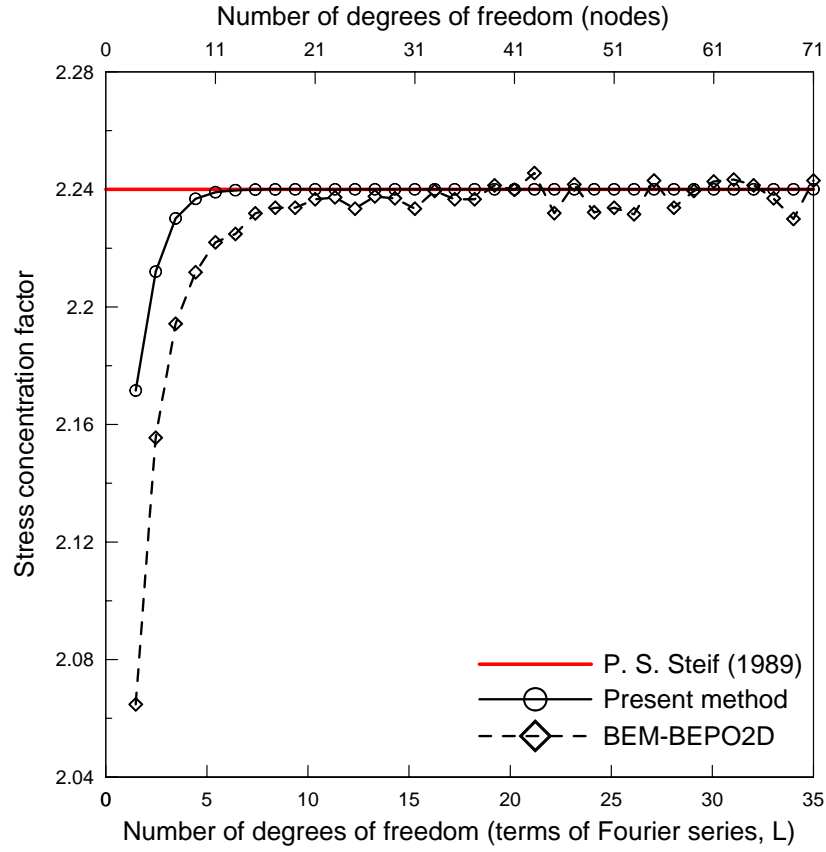
Figure 4-2 (c) Convergence test of the two equal-sized holes problem ($d = 1.0$)
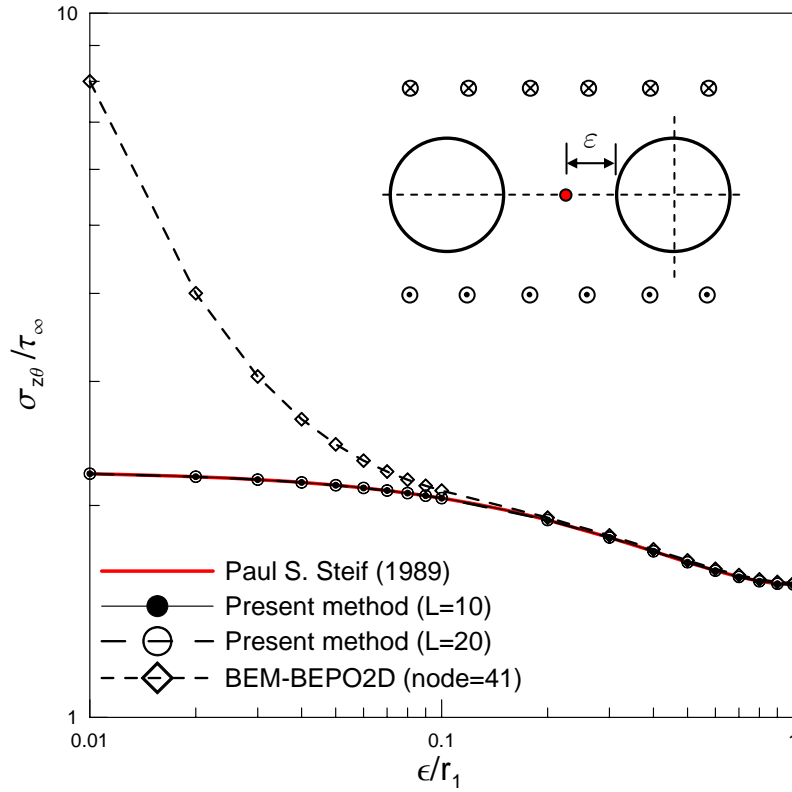
Figure 4-2 (d) Tangential stress in the matrix near the boundary ($d = 1.0$)
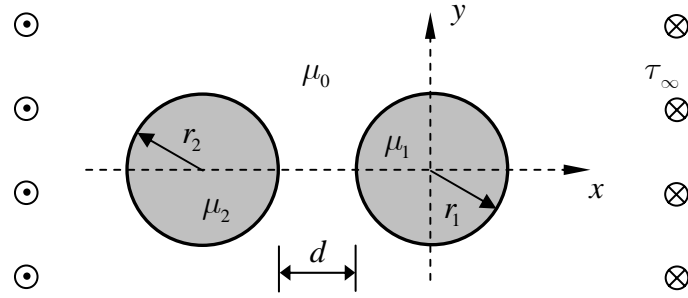
Figure 4-3 (a) Two identical inclusions with centers on the x axis
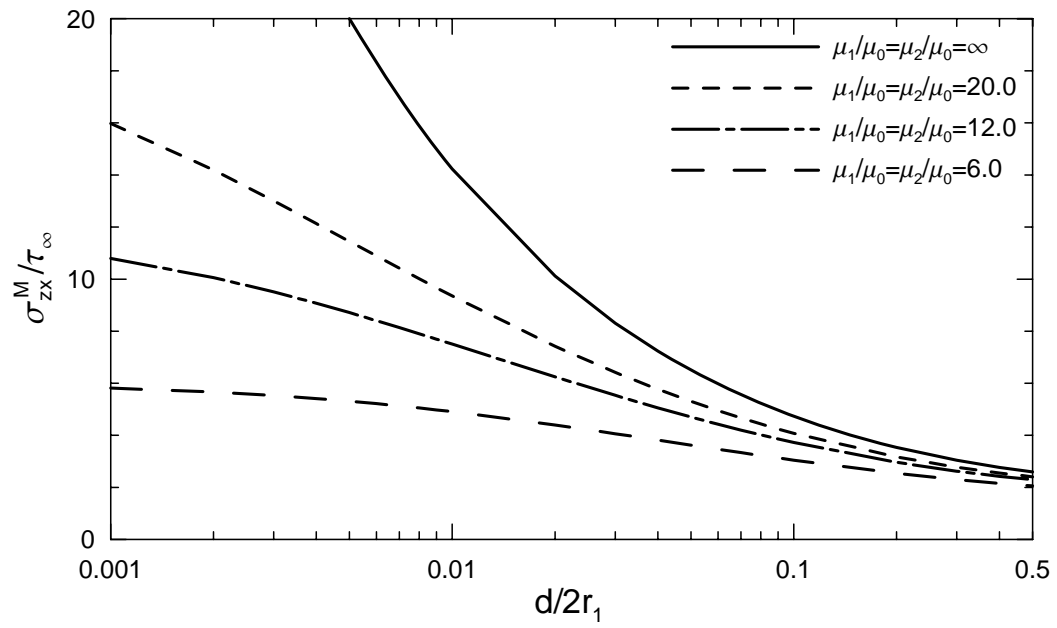
Figure 4-3 (b) Stress concentration factor of inclusion versus inclusion spacing
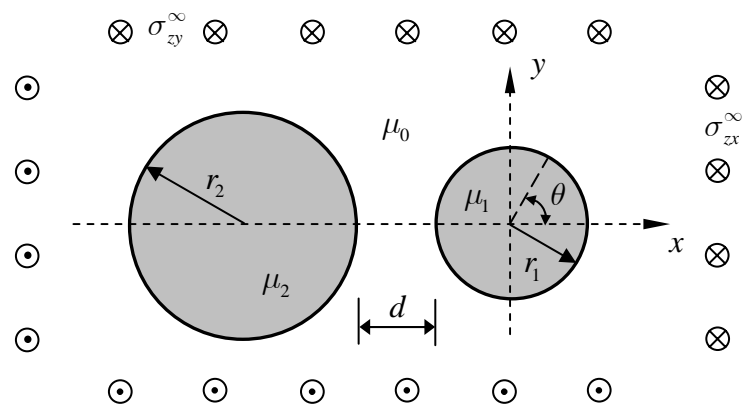
Figure 4-4 (a) Two circular inclusions with centers on the x axis
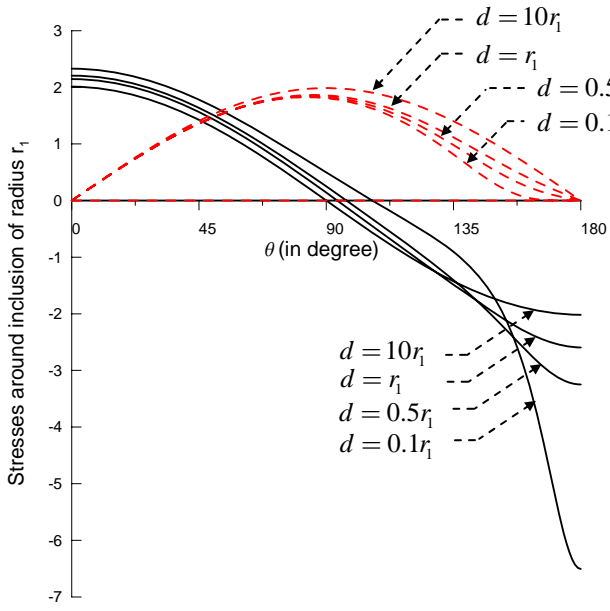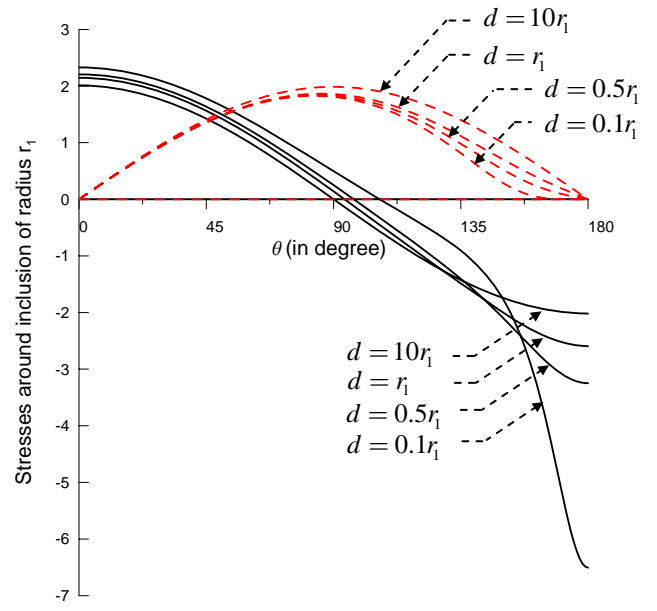
Figure 4-4 Effects of spacing on the stresses around the boundary of radius r_1 for two equal-sized inclusions (b) $L = 20$, (c) $L = 40$
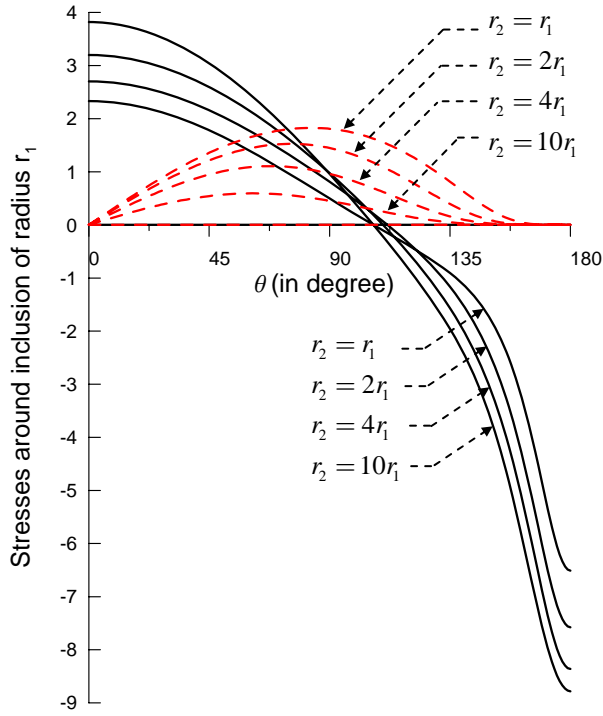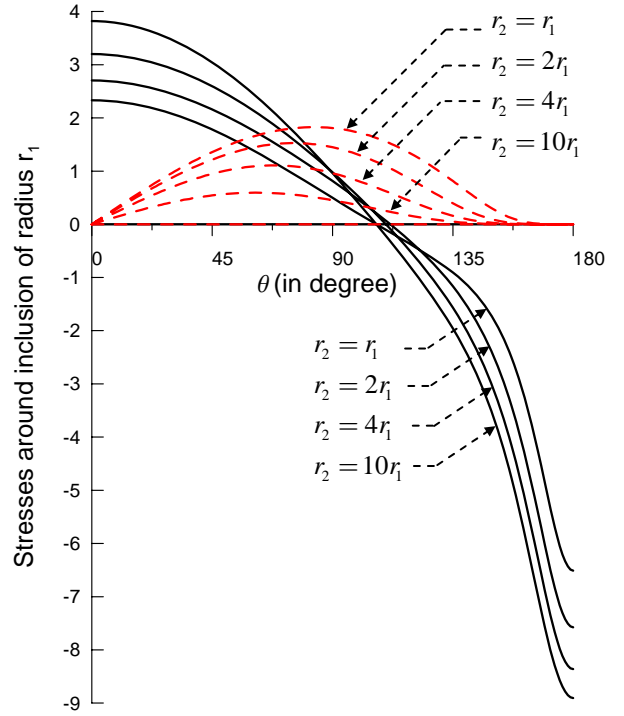
Figure 4-4 Effects of the size of neighboring inclusion on the stresses around the boundary of radius r_1 with $d = 0.1r_1$ (d) $L = 80$, (e) $L = 100$
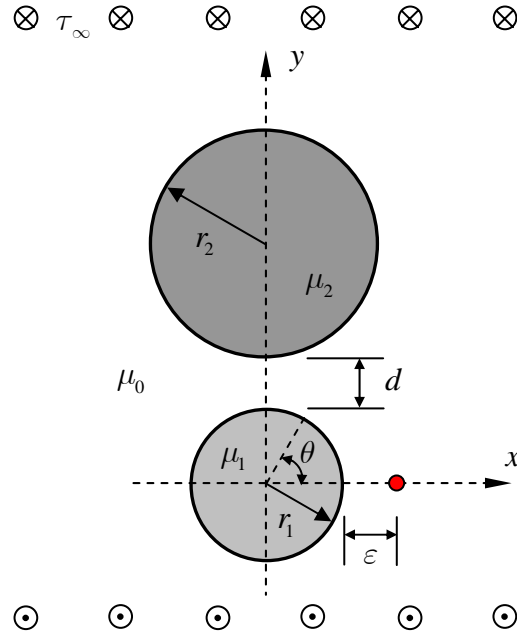
Figure 4-5 (a) Two circular inclusions with centers on the y axis
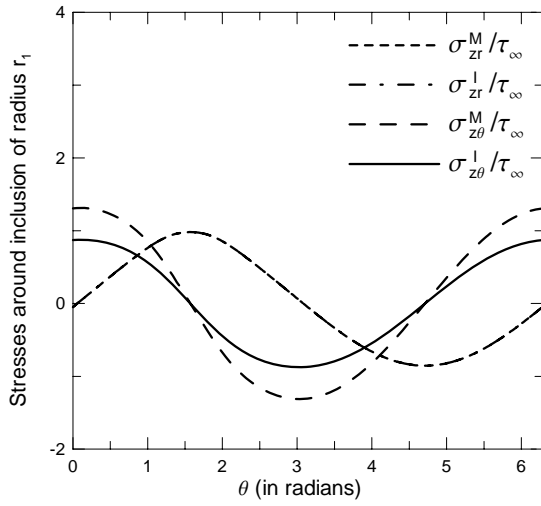
Figure 4-5 (b) Stresses around the circular boundary of radius r_1
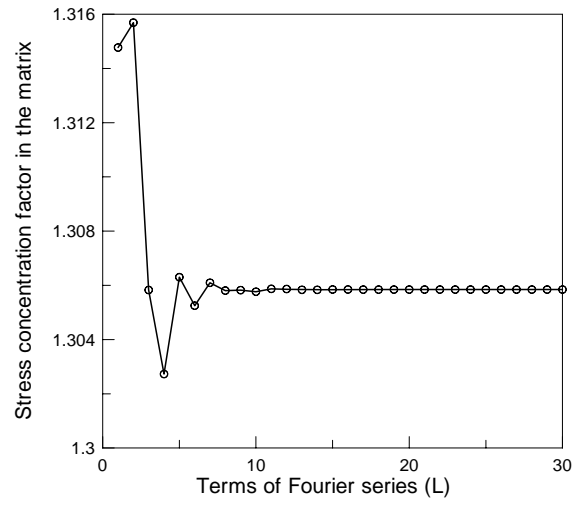
Figure 4-5 (c) Convergence test of the two-inclusions problem
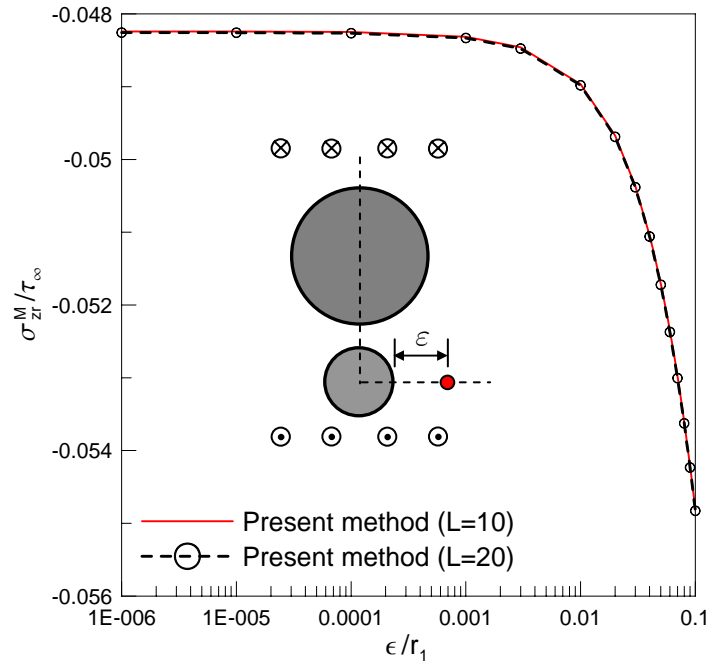
Figure 4-5 (d) Radial stress in the matrix near the boundary
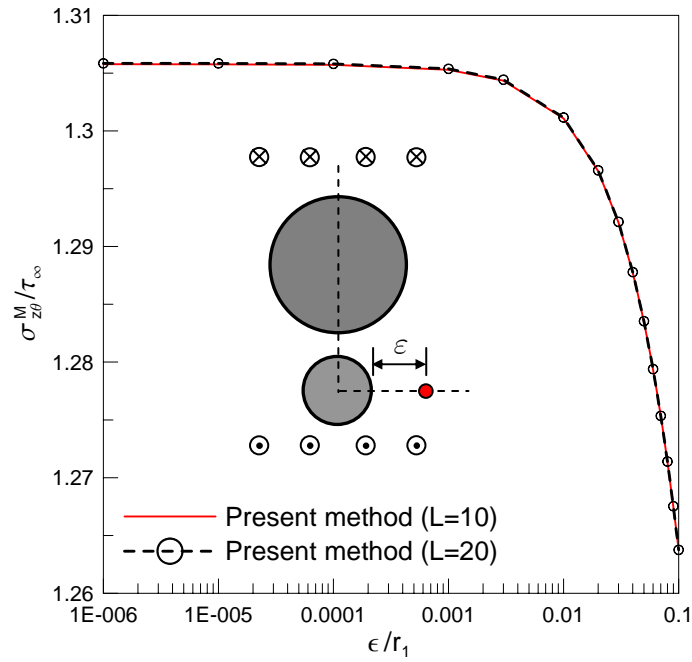
Figure 4-5 (e) Tangential stress in the matrix near the boundary
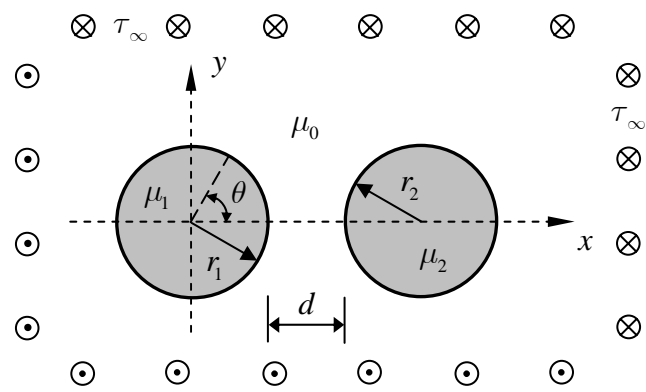
Figure 4-6 (a) Two circular inclusions embedded in a matrix under the remote anti-plane shear in two directions
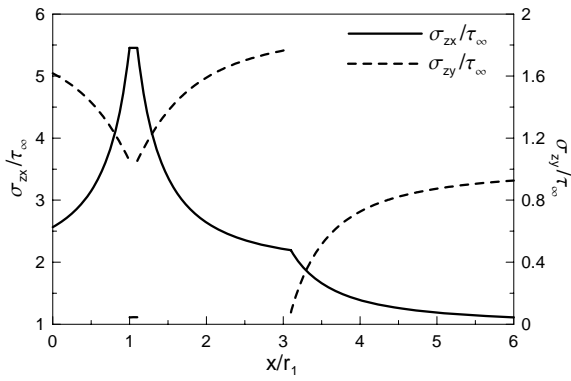
Figure 4-6 (b) Stress distributions along the
x axis when $d = 0.1$
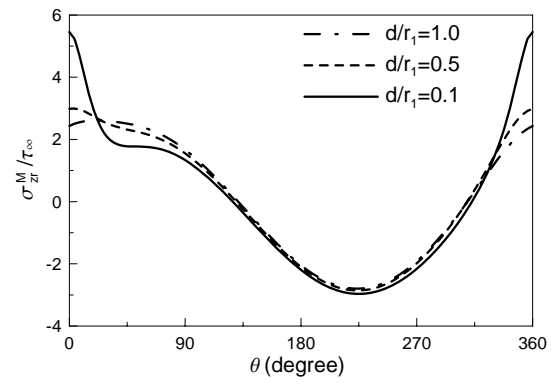
Figure 4-6 (e) Normal stress distributions
along the contour $(1.001, \theta)$
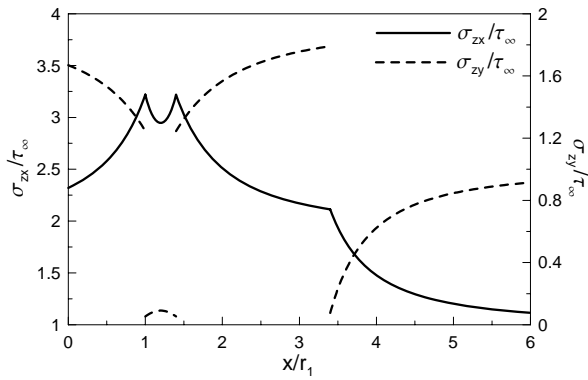
Figure 4-6 (c) Stress distributions along the
x axis when $d = 0.4$
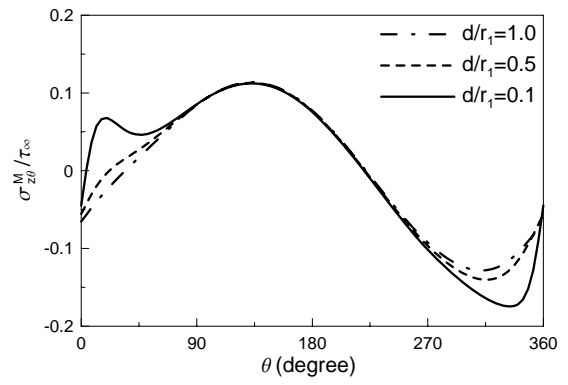
Figure 4-6 (f) Tangential stress distributions
along the contour $(1.001, \theta)$
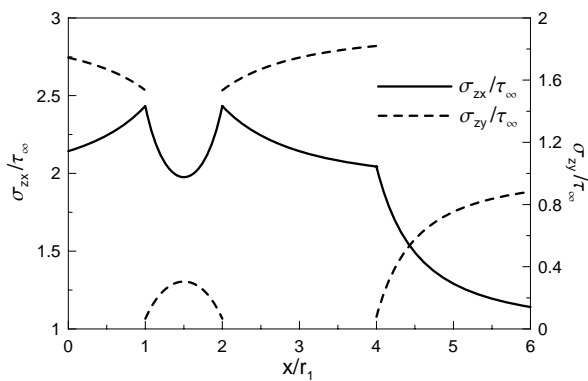
Figure 4-6 (d) Stress distributions along the
x axis when $d = 1.0$
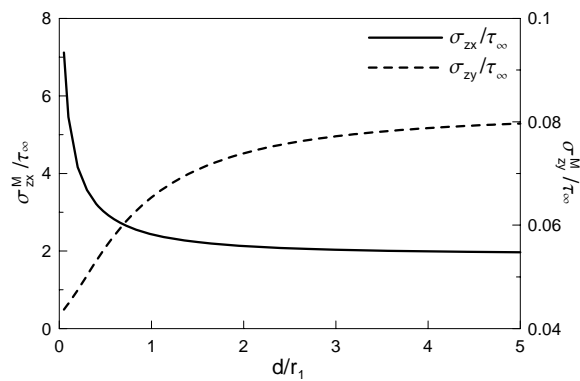
Figure 4-6 (g) Variations of stresses at the
point $(1.001, 0°)$
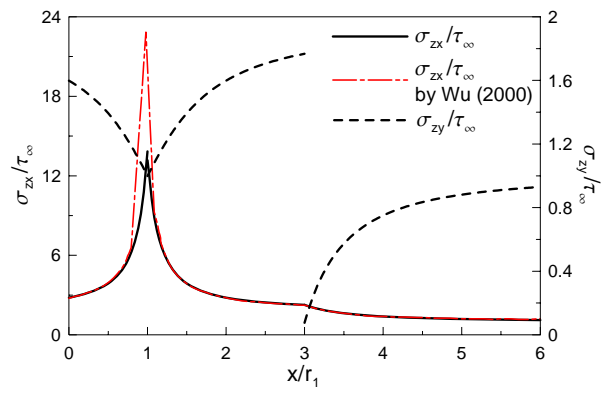
Figure 4-6 (h) Stress distributions along the x axis when the two inclusions touch each other
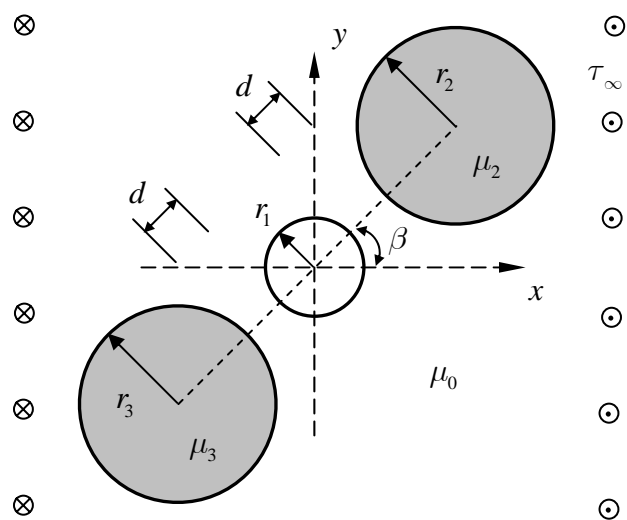
Figure 4-7 (a) One hole surrounded by two circular inclusions
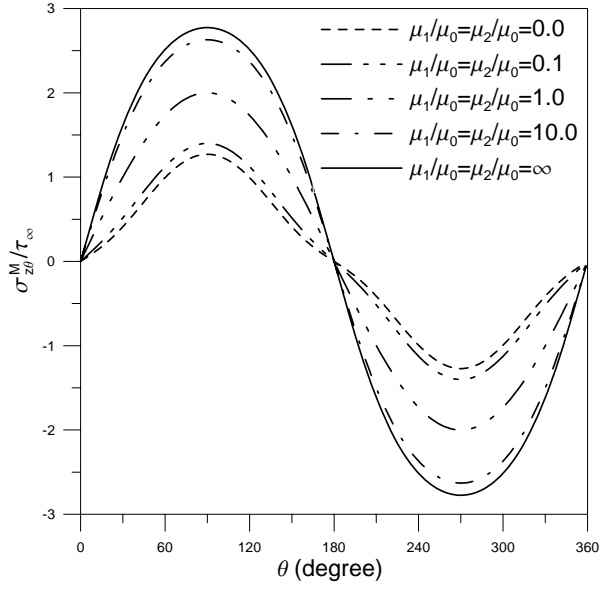
Figure 4-7 (b) Tangential stress distribution along the hole boundary with $\beta = 0°$
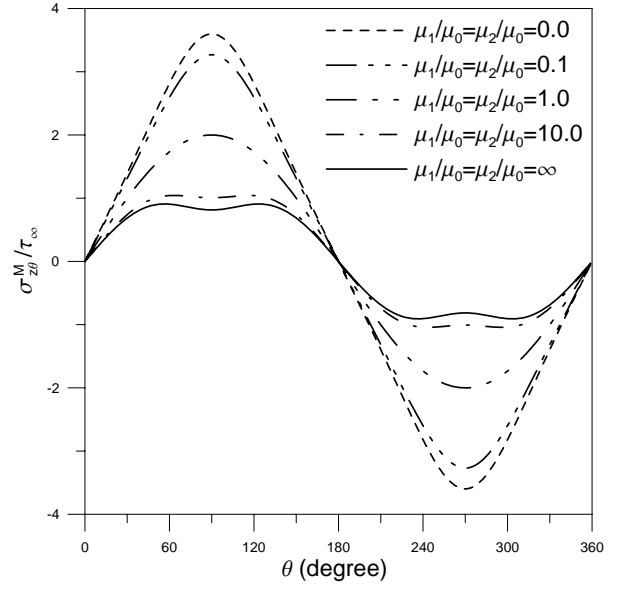
Figure 4-7 (c) Tangential stress distribution along the hole boundary with $\beta = 90°$
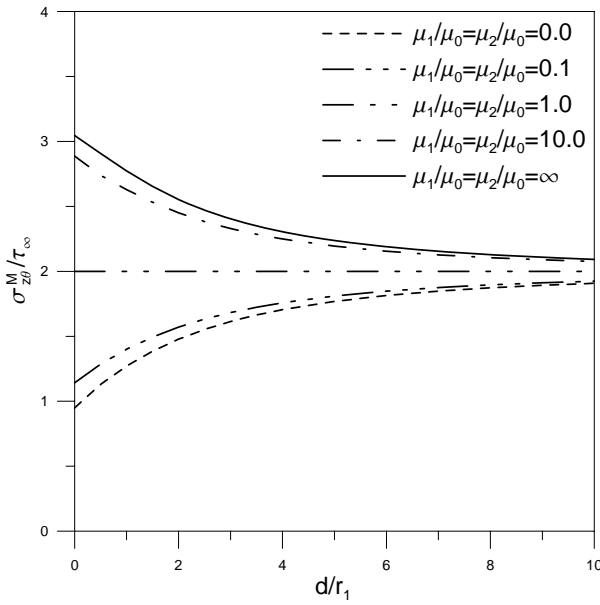
Figure 4-7 (d) Stress concentration as a function of the spacing d / r_1 with $\beta = 0°$
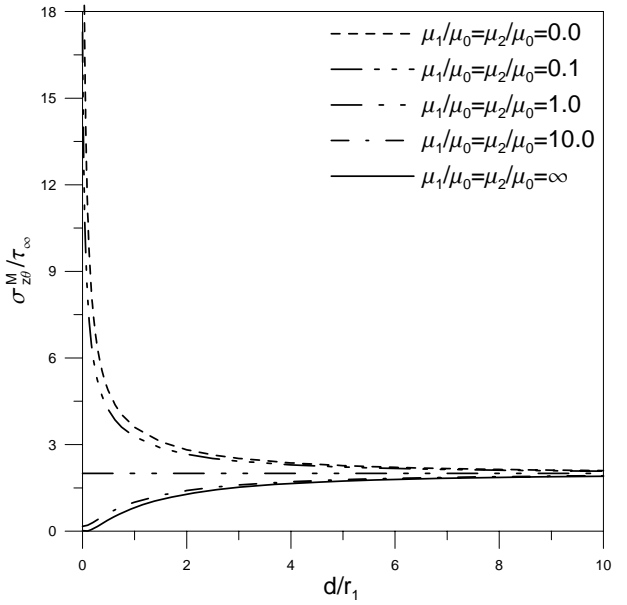
Figure 4-7 (e) Stress concentration as a function of the spacing d / r_1 with $\beta = 90°$
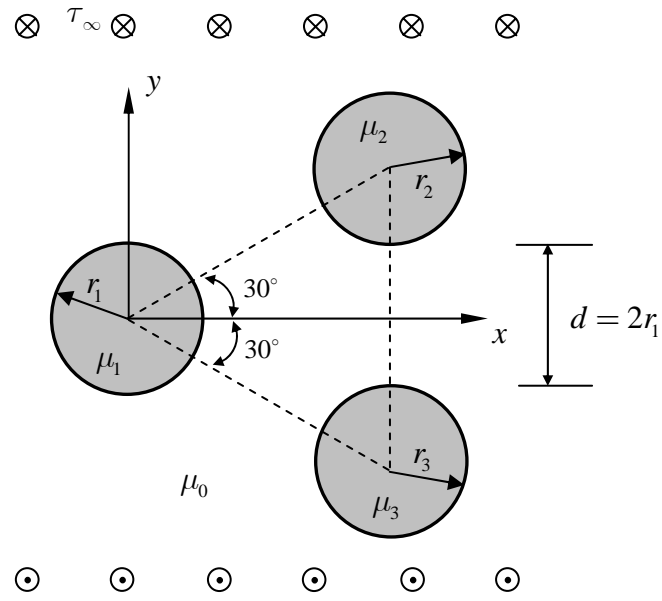
Figure 4-8 (a) Three identical inclusions forming an equilateral triangle
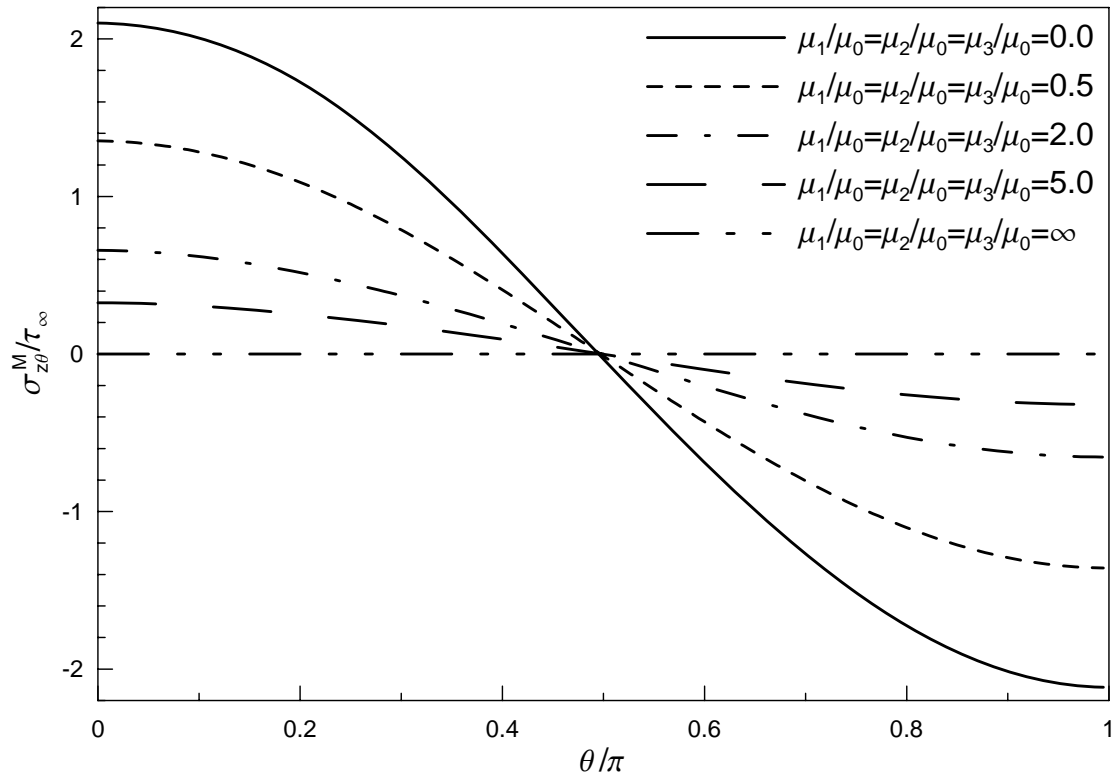
Figure 4-8 (b) Tangential stress distribution around the inclusion located at the origin

Chapter 5 Conclusions and further research

5.1 Conclusions

In this thesis, we proposed a null-field integral equation approach for piezoelectricity problems with circular inclusions under anti-plane condition. Apparently, this is a very useful, semi-analytical and numerical method, and it can provide accurate solutions for multi-inclusion interaction problems. Based on the proposed formulation for solving boundary value problems involving circular holes and/or inclusions, some concluding remarks are itemized as follows:

1. A unified formulation for solving boundary value problems with circular holes and/or inclusions was proposed successfully in this thesis although our main applications are limited to Laplace problems. Regarding the null-field approach, degenerate kernels for fundamental solutions and Fourier expansions for boundary densities were adopted in the adaptive observer system. Piezoelectricity problems with circular inclusions as well as the uncoupling cases, in-plane electrostatic and anti-plane elastic problems, were examined to verify the accuracy of the present formulation for various sizes, locations, material constants and magnitudes of applied loadings. All the numerical results match well with those of other approaches and analytical solutions.

2. The singularity and hypersingularity were avoided due to the introduction of degenerate kernels for interior and exterior regions separated by the circular boundary. Instead of directly calculating principal values, all the boundary integrals can be performed analytically by using the degenerate kernel and Fourier expansion. Therefore, the present approach is seen as a "semi-analytical" approach since error only ascribes to the truncated Fourier series.

3. Boundary-layer effect for the calculation of stress near the boundary was eliminated since degenerate kernels can clearly describe the jump behavior of

potential from interior to exterior domains, respectively. Numerical results indicate that the stress across the near boundary stress can be described smoothly by using the present approach without any treatments of regularization, transformation or other techniques. Boundary-layer effect free is inherent in the present approach.

4. The convergence study shows that only a few terms of Fourier series can yield acceptable results and the convergence rate is fast. It is because that the use of degenerate kernels for fundamental solutions and Fourier expansions for boundary densities leads to the exponential convergence.

5. The influence matrix in the linear algebraic system using the present formulation is well-posed since the jump behavior of potential distribution was separately described in different regions by using the degenerate kernels for the representation of fundamental solutions.

6. Four goals of singularity free, boundary-layer effect free, exponential convergence and well-posed model are achieved.

7. Adaptive observer system and vector decomposition technique were employed to efficiently calculate the invariant of direction derivative of potential gradient using the hypersingular formulation.

8. To the author's best knowledge, the studies of more than "two" circular inclusion problems are very few. We have presented an approach for solving problems with multiple circular inclusions. Since analytical solutions are not available, our semi-analytical results may provide a datum for other researchers' reference.

9. The results of two equal-sized holes, *e.g.* convergence test, boundary-layer effect detection and error analysis, demonstrate the superiority of present method over the conventional boundary element method on the basis of the same number of

degrees of freedom.

10. A general-purpose program for solving Laplace problems involving an infinite domain with multiple circular inclusions of various radii, arbitrary positions and different material constants was developed. Its possible applications in engineering are very broad, not only limited in this thesis.

5.2 Further studies

In this thesis, our formulation has been applied to solve anti-plane piezoelectricity problems with circular inclusions as well as in-plane electrostatic and anti-plane elastic problems by using the degenerate kernels for representing fundamental solutions and Fourier expansions for expanding boundary densities in the null-field integral equation. However, several issues are worth to be further investigated as follows:

1. Although it seems that the applications is limited for circular holes and/or inclusions, the idea and algorithm of the thesis can be extended to problems of general boundaries. Once the degenerate kernel and expansion of boundary densities are available. Therefore, three-dimensional problems with spherical cavities and/or inclusions can be solved in a similar way.

2. For problems with straight (crack and regular) boundaries, our method can also be applied by changing the dummy variable θ into R. How to expand the boundary density along the line is a challenge to ensure the orthogonal property with respect to bases of degenerate kernels.

3. We have demonstrated our formulation through several engineering applications which satisfy the Laplace equation. Engineering problems involving multiple inclusions under various loading types, *e.g.* concentrated forces, screw dislocations, edge dislocations, torques, in-plane shears and in-plane tensions, and with other inhomogeneous types, *e.g.* coated fibers, inclusions with imperfect interfaces and

110

composite bars, may be considered. The main difficulty of screw dislocation is that the Green's third identity can not be directly applied. On the other hand, we may apply the same procedure to other fields, *e.g.* the heat transfer in finite tissue with blood vessels in biomechanics.

4. The asymptotic behavior of $1/\sqrt{\varepsilon}$ for stresses near two approaching inclusions can be numerically studied using the present formulation with higher number of terms in Fourier series.

5. It is well known that the Green's function can be derived by various methods. Null-field approach also provides an alternative way to construct the Green's function.

6. Half plane and half space problems with multiple inclusions can be solved by using the present approach in a straightforward way after introducing the image concept to match our model.

7. The fundamental solution was expanded to degenerate kernels with respect to a single center for the eccentric case by the separable technique. Hence, the adaptive observer system was required to fully capture the geometry of each circle. The bi-center expansion technique for the source and field systems may be suitable for the eccentric case in a straightforward way such that adaptive observer system is not required.

8. Mogilevskaya and Crouch have used the Galerkin method instead of collocation technique for multiple circular elastic inclusions. The present approach can be extended to the Galerkin formulation only for circular and annular cases. If bi-center expansion is feasible, the Galerkin formulation can be directly applied.

9. According to the limit of computer hardware, it may be difficult for solving large

scale problems. After employing the fast algorithm technique, large scale problems can be solved easily. This is the hot topic of BEM research in recent years.

10. The phenomenon of degenerate scale using the proposed formulation for solving Laplace problems containing multiple circular holes has been studies by Chen and Shen. Whether the degenerate scale exists for Laplace problems containing multiple circular inclusions needs further study. To deal with the problem of degenerate scale, possible remedies including the method of adding a rigid body term, dual formulation and SVD updating technique may be alternatives to overcome the rank-deficiency problem.

References

[1]   Ang WT and Kang I, 2000, A complex variable boundary element method for elliptic partial differential equations in a multiply-connected region, *International Journal of Computer Mathematics*, Vol. **75**, pp. 515-525.

[2]   Balcerzak MJ and Raynor S, 1961, Steady state temperature distribution and heat flow in prismatic bars with isothermal boundary conditions, *International Journal of Heat and Mass Transfer*, Vol. **3**, pp. 113-125.

[3]   Barnes R and Jankovic I, 1999, Two-dimensional flow through large numbers of circular inhomogeneities, *Journal of Hydrology*, Vol. **226**, pp. 204-210.

[4]   Barone MR and Caulk DA, 1981, Special boundary integral equations for approximate solution of Laplace's equation in two-dimensional regions with circular holes, *Quarterly Journal of Mechanics and Applied Mathematics*, Vol. **34**, pp. 265-286.

[5]   Barone MR and Caulk DA, 1982, Optimal arrangement of holes in a two-dimensional heat conductor by a special boundary integral method, *International Journal for Numerical Methods in Engineering*, Vol. **18**, pp. 675-685.

[6]   Barone MR and Caulk DA, 1985, Special boundary integral equations for approximate solution of potential problems in three-dimensional regions with slender cavities of circular cross-section, *IMA Journal of Applied Mathematics*, Vol. **35**, pp. 311-325.

[7]   Barone MR and Caulk DA, 2000, Analysis of liquid metal flow in die casting, *International Journal of Engineering Science*, Vol. **38**, pp. 1279-1302.

[8]   Bates RHT, 1968, Modal expansions for electromagnetic scattering from perfectly conducting cylinders of arbitrary cross-section, *Proceedings of the Institution of Electrical Engineers*, Vol. **115**, pp. 1443-1445.

[9]   Bates RHT and Wall DJN, 1977, Null field approach to scalar diffraction, I. General method, *Philosophical Transactions of the Royal Society of London*, Vol. **287**, pp. 45-78.

[10] Benveniste Y, Dvorak GJ and Chen T, 1989, Stress fields in composites with coated inclusions, *Mechanics of Materials*, Vol. **7**, pp. 305-317.

[11] Bird MD and Steele CR, 1991, Separated solution procedure for bending of circular plates with circular holes, *ASME Applied Mechanics Reviews*, Vol. **44**, pp. 27-35.

[12] Bird MD and Steele CR, 1992, A solution procedure for Laplace's equation on multiply-connected circular domains, *ASME Journal of Applied Mechanics*, Vol. **59**, pp. 398-404.

[13] Bleustein JL, 1968, New surface wave in piezoelectric materials, *Applied Physics Letters*, Vol. **13**, pp. 412-143.

[14] Boström A, 1982, Time-dependent scattering by a bounded obstacle in three dimensions, *Journal of Mathematical Physics*, Vol. **23**, pp. 1444-1450.

[15] Budiansky B and Carrier GF, 1984, High shear stresses in stiff-fiber composites, *ASME Journal of Applied Mechanics*, Vol. **51**, pp. 733-735.

[16] Caulk DA, 1983, Analysis of elastic torsion in a bar with circular holes by a special boundary integral method, *ASME Journal of Applied Mechanics*, Vol. **50**, pp. 101-108.

[17] Caulk DA, 1983, Analysis of steady heat conduction in regions with circular holes by a special boundary integral method, *IMA Journal of Applied Mathematics*, Vol. **30**, pp. 231-246.

[18] Caulk DA, 1983, Steady heat conduction from an infinite row of holes in a half-space or a uniform slab, *International Journal of Heat and Mass Transfer*, Vol. **26**, pp. 1509-1513.

[19] Caulk DA, 1984, Special boundary integral equations for potential problems in regions with circular holes, *ASME Journal of Applied Mechanics*, Vol. **51**, pp. 713-716.

[20] Chao CK and Chang KJ, 1999, Interacting circular inclusions in antiplane piezoelectricity, *International Journal of Solids and Structures*, Vol. **36**, pp. 3349-3373.

[21] Chao CK, Chen FM and Shen MH, 2006, Circularly cylindrical layered media in

plane elasticity, *International Journal of Solids and Structures*, Vol. **43**, pp. 4739-4756.

[22] Chao CK and Young CW, 1998, On the general treatment of multiple inclusions in antiplane elastostatics, *International Journal of Solids and Structures*, Vol. **35**, pp. 3573-3593.

[23] Chen CT, 2005, Null-field integral equation approach for Helmholtz (interior and exterior acoustic) problems with circular boundaries, Master Thesis, *Department of Harbor and River Engineering*, *National Taiwan Ocean University*, Keelung, Taiwan.

[24] Chen HB, Lu P and Schnack E, 2001, Regularized algorithms for the calculation of values on and near boundaries in 2D elastic BEM, *Engineering Analysis with Boundary Elements*, Vol. **25**, pp. 851-876.

[25] Chen JT and Chiu YP, 2002, On the pseudo-differential operators in the dual boundary integral equations using degenerate kernels and circulants, *Engineering Analysis with Boundary Elements*, Vol. **26**, pp. 41-35.

[26] Chen JT and Hong H-K, 1994, Dual boundary integral equations at a corner using contour approach around singularity, *Advances in Engineering Software*, Vol. **21**, pp. 169-178.

[27] Chen JT and Hong H-K, 1999, Review of dual boundary element methods with emphasis on hypersingular integrals and divergent series, *ASME Applied Mechanics Reviews*, Vol. **52**, pp. 17-33.

[28] Chen JT, Hong H-K, Chen IL and Chen KH, 2003, Nonuniqueness and its treatment in the boundary integral equations and boundary element methods, *Computational Mathematics Conference*, Plenary lecture, Hsin-Chu, Taiwan.

[29] Chen JT, Hsiao CC and Leu SY, 2006, Null-field integral equation approach for plate problems with circular boundaries, *ASME Journal of Applied Mechanics*, Vol. **73**, pp. 679-693.

[30] Chen JT and Kuo SR, 2000, On fictitious frequencies using circulants for radiation problems of a cylinder, *Mechanics Research Communications*, Vol. **27**, pp. 49-58.

[31] Chen JT, Kuo SR and Chen KH, 1999, A nonsingular integral formulation for the Helmholtz eigenproblems of a circular domain, *Journal of the Chinese Institute of Engineers*, Vol. **22**, pp. 729-739.

[32] Chen JT, Kuo SR and Lin JH, 2002, Analytical study and numerical experiments for degenerate scale problems in the boundary element method for two-dimensional elasticity, *International Journal for Numerical Methods in Engineering*, Vol. **54**, pp. 1669-1681.

[33] Chen JT and Lin SR, 2002, On the rank-deficiency problems in boundary integral formulation using the Fredholm alternative theorem and singular value decomposition technique, *Fifth World Congress on Computational Mechanics*, Keynote lecture, Vienna, Austria.

[34] Chen JT, Lin SY, Liu LW and Lin JH, 2003, BEM for multiply-connected eigenproblems, *BEM-FEM 20th International Conference Mathematical Modeling in Solids Mechanics*, Plenary lecture, Saint Petersburg, Russia.

[35] Chen JT, Shen WC and Chen PY, 2006, Analysis of circular torsion bar with circular holes using null-field approach, *Computer Modeling in Engineering & Science*, Vol. **12**, pp. 109-119

[36] Chen JT, Shen WC and Wu AC, 2006, Null-field integrals equations for stress field around circular holes under antiplane shear, *Engineering Analysis with Boundary Element*s, Vol. **30**, pp. 205-217.

[37] Chen JT and Wu AC, 2006, Null-field approach for piezoelectricity problems with arbitrary circular inclusions, *Engineering Analysis with Boundary Element*s, **Accepted**

[38] Chen JT and Wu AC, 2006, Null-field approach for the multi-inclusion problem under anti-plane shears, *ASME Journal of Applied Mechanics*, **Accepted**.

[39] Chen JT and Wu CS, 2006, Alternative derivations for the Poisson integral formula, *International Journal of Mathematical Education in Science and Technology*, Vol. **37**, pp. 165-185.

[40] Chen JT, Wu CS, Chen IL and Chen KH, 2005, The equivalence of the Trefftz method and method of fundamental solutions for Laplace and biharmonic

equations, *Computers and Mathematics with Applications*, **Accepted**.

[41] Chen T and Chiang SC, 1997, Electroelastic fields and effective moduli of a medium containing cavities or rigid inclusions of arbitrary shape under anti-plane mechanical and in-plane electric fields, *Acta Mechanica*, Vol. **121**, pp. 79-96.

[42] Chen T and Weng IS, 2001, Torsion of a circular compound bar with imperfect interface, *ASME Journal of Applied Mechanics*, Vol. **68**, pp. 955-958.

[43] Chou SI, 1997, Stress field around holes in antiplane shear using complex variable boundary element method, *ASME Journal of Applied Mechanics*, Vol. **64**, pp. 432-435.

[44] Crouch SL and Mogilevskaya SG, 2003, On the use of Somigliana's formula and Fourier series for elasticity problems with circular boundaries, *International Journal for Numerical Methods in Engineering*, Vol. **58**, pp. 537-578.

[45] Dundurs J and Mura T, 1964, Interaction between an edge dislocation and a circular inclusion, *Journal of the Mechanics and Physics of Solids*, Vol. **12**, pp. 177-189.

[46] Emets YP and Onofrichuk YP, 1996, Interaction forces of dielectric cylinders in electric fields, *IEEE Transactions on Dielectrics and Electrical Insulation*, Vol. **3**, pp. 87-98.

[47] Fan H and Wang GF, 2003, Screw dislocation interacting with imperfect interface, *Mechanics of Materials*, Vol. **35**, pp. 943-953.

[48] Gong SX, 1995, Antiplane interaction among multiple circular inclusions, *Mechanics Research Communications*, Vol. **22**, pp.257-262.

[49] Gong SX and Meguid SA, 1993, Interacting circular inhomogeneities in plane elastostatics, *Acta Mechanica*, Vol. **99**, pp. 49-60.

[50] Goree JG and Wilson HB, 1967, Transverse shear loading in an elastic matrix containing two circular cylindrical inclusions, *ASME Journal of Applied Mechanics*, Vol. **34**, pp. 511-513.

[51] Gray LJ and Manne LL, 1993, Hypersingular integrals at a corner, *Engineering Analysis with Boundary Elements*, Vol. **11**, pp. 327-334.

[52] Greenberg MD, 1971, Applications of Green's function in science and

engineering, *Prentice-Hall*, New Jersey.

[53] Greengard L and Moura M, 1994, On the numerical evaluation of electrostatic field in composite materials, *Acta Numerica*, Vol. **3**, pp. 379-410.

[54] Greenwood JA, 1989, Exact formulae for stresses around circular holes and inclusions, *International Journal of Mechanical Sciences*, Vol. **31**, pp. 219-227.

[55] Guiggiani M, 1995, Hypersingular boundary integral equations have an additional free term, *Computational Mechanics*, Vol. **16**, pp. 245-248.

[56] Honein E, Honein T and Herrmann G, 1992, On two circular inclusions in harmonic problem, *Quarterly of Applied Mathematics*, Vol. **50**, pp. 479-499.

[57] Honein E, Honein T and Herrmann G, 2000, Energetics of two circular inclusions in anti-plane elastostatics, *International Journal of Solids and Structures*, Vol. **37**, pp. 3667-3679.

[58] Honein T, Honein BV, Honein E and Herrmann G, 1995, On the interaction of two piezoelectric fibers embedded in an intelligent material, *Journal of Intelligent Material Systems and Structures*, Vol. **6**, pp. 229-236.

[59] Hsiao CC, 2005, A semi-analytical approach for Stokes flow and plate problems with circular boundaries, Master Thesis, *Department of Harbor and River Engineering*, *National Taiwan Ocean University*, Keelung, Taiwan.

[60] Huang Q and Cruse TA, 1993, Some notes on singular integral techniques in boundary element analysis, *International Journal for Numerical Methods in Engineering*, Vol. **36**, pp. 2643-2659.

[61] Ishihara M and Noda N, 1999, An electroelastic problem of an infinite piezoelectric body with two inhomogeneities, *JSME International Journal Series A*, Vol. **42**, pp. 492-498.

[62] Jiang CP and Cheung YK, 2001, An exact solution for the three-phase piezoelectric cylinder model under antiplane shear and its applications to piezoelectric composites, *International Journal of Solids and Structures*, Vol. **38**, pp. 4777-4796.

[63] Kisu H and Kawahara T, 1988, Boundary element analysis system based on a formulation with relative quantity, Boundary Elements X, Brebbia CA, eds.,

Springer-Verlag, Vol. **1**, pp. 111-121.

[64] Kress R, 1989, Linear integral equations, *Springer-Verlag*, Berlin.

[65] Kutt HR, 1975, Quadrature formulae for finite part integrals, CSIR Special Report WISK 178, *National Research Institute for Mathematical Sciences, CSIR*, S Africa.

[66] Lebedev NN, Skalskaya IP and Uflyand YS, 1979, Worked problem in applied mathematics, *Dover Publications*, New York.

[67] Legros B, Mogilevskaya SG and Crouch SL, 2004, A boundary integral method for multiple circular inclusions in an elastic half-plane, *Engineering Analysis with Boundary Elements*, Vol. **28**, pp. 1083-1098.

[68] Martin PA, 1980, On the null-field equations for the exterior problems of acoustics, *Quarterly Journal of Mechanics and Applied Mathematics*, Vol. **33**, pp. 385-396.

[69] Martin PA, 1981, On the null-field equations for water-wave radiation problems, *Journal of Fluid Mechanics*, Vol. **113**, pp. 315-332.

[70] Melnikov YA and Melnikov MY, 2001, Modified potentials as a tool for computing Green's functions in continuum mechanics, *Computer Modeling in Engineering & Science*, Vol. **2**, pp. 291-305

[71] Mogilevskaya SG and Crouch SL, 2001, A Galerkin boundary integral method for multiple circular elastic inclusions, *International Journal for Numerical Methods in Engineering*, Vol. **52**, pp. 1069-1106.

[72] Muskhelishvili NI, 1953, Some basic problems of the mathematical theory of elasticity, *Noordhoff*, Groningen.

[73] Olsson P, 1984, Elastostatics as a limit of elastodynamics – a matrix formulation, *Applied Scientific Research*, Vol. **41**, pp. 125-151.

[74] Pak YE, 1992, Circular inclusion problem in antiplane piezoelectricity, *International Journal of Solids and Structures*, Vol. **29**, pp. 2403-2419.

[75] Pak YE, 1992, Linear electro-elastic fracture mechanics of piezoelectric materials, *International Journal of Fracture*, Vol. **54**, pp. 79-100.

[76] Sendeckyj GP, 1971, Multiple circular inclusion problems in longitudinal shear

deformation, *Journal of Elasticity*, Vol. **1**, pp. 83-86.

[77] Shen WC, 2005, Null-field approach for Laplace problems with circular boundaries using degenerate kernels, Master Thesis, *Department of Harbor and River Engineering*, *National Taiwan Ocean University*, Keelung, Taiwan.

[78] Sladek V and Sladek J, 1991, Elimination of the boundary layer effect in BEM computation of stresses, *Communications in Applied Numerical Methods*, Vol. **7**, pp. 539-550.

[79] Sladek V, Sladek J and Tanaka M, 1993, Regularization of hypersingular and nearly singular integrals in the potential theory and elasticity, *International Journal for Numerical Methods in Engineering*, Vol. **36**, pp. 1609-1628.

[80] Smith E, 1968, The interaction between dislocations and inhomogeneities-I, *International Journal of Engineering Science*, Vol. **6**, pp. 129-143.

[81] Sokolnikoff IS, 1956, Mathematical theory of elasticity, *McGraw-Hill*, New York.

[82] Steif PS, 1989, Shear stress concentration between holes, *ASME Journal of Applied Mechanics*, Vol. **56**, pp. 719-721.

[83] Sudak LJ, 2002, On the interaction between a dislocation and a circular inhomogeneity with imperfect interface in antiplane shear, *Mechanics Research Communications*, Vol. **30**, pp. 53-59.

[84] Telles JCF, 1987, A self-adaptative coordinate transformation for efficient numerical evaluation of general boundary element integrals, *International Journal for Numerical Methods in Engineering*, Vol. **24**, pp. 959-973.

[85] Varatharajulu V and Pao Y-H, 1976, Scattering matrix for elastic waves, I. Theory, *Journal of Acoustical Society of America*, Vol. **60**, pp. 556-566.

[86] Wang J, Crouch SL and Mogilevskaya SG, 2005, A fast and accurate algorithm for a Galerkin boundary integral method, *Computational Mechanics*, Vol. **37**, pp. 96-109.

[87] Wang J, Mogilevskaya SG and Crouch SL, 2002, A numerical procedure for multiple circular holes and elastic inclusions in a finite domain with a circular boundary, *Computational Mechanics*, Vol. **32**, pp. 250-258.

[88] Wang X and Shen Y-P, 2001, On double circular inclusion problem in antiplane

piezoelectricity, *International Journal of Solids and Structures*, Vol. **38**, pp. 4439-4461.

[89] Wang X and Zhong Z, 2003, A circular inclusion with a nonuniform interphase layer in anti-plane shear, *International Journal of Solids and Structures*, Vol. **40**, pp. 881-897.

[90] Waterman PC, 1965, Matrix formulation of electromagnetic scattering, *Proceedings of the IEEE*, Vol. **53**, pp. 805-812.

[91] Waterman PC, 1969, New formulation of acoustic scattering, *Journal of Acoustical Society of America*, Vol. **45**, pp. 1417-1429.

[92] Waterman PC, 1976, Matrix theory of elastic wave scattering, *Journal of Acoustical Society of America*, Vol. **60**, pp. 567-580.

[93] Wu KC, 2004, A new boundary integral equation method for analysis of cracked linear elastic bodies, *Journal of the Chinese Institute of Engineers*, Vol. **27**, pp. 935-939.

[94] Wu LZ, 2000, Interaction of two circular cylindrical inhomogeneities under anti-plane shear, *Composites Science and Technology*, Vol. **60**, pp. 2609-2615.

[95] Wu LZ and Funami K, 2002, The electro-elastic field of the infinite piezoelectric medium with two piezoelectric circular cylindrical inclusions, *Acta Mechanica Sinica*, Vol. **18**, pp. 368-385.

[96] Xiao ZM, Yan J and Chen BJ, 2004, Electro-elastic stress analysis for a screw dislocation interacting with a coated inclusion in piezoelectric solid, *Acta Mechanica*, Vol. **172**, pp. 237-249.

[97] Zhong Z and Meguid SA, 1997, Interfacial debonding of a circular inhomogeneity in piezoelectric materials, *International Journal of Solids and Structures*, Vol. **34**, pp.1965-1984.

[98] Zimmerman RW, 1988, Second-Order approximation for the compression of an elastic plate containing a pair of circular holes, *Zeitschrift fur Angewandte Mathematik und Mechanik*, Vol. **68**, pp. 575-577.

[99] 陳正宗與洪宏基，1992，邊界元素法，新世界出版社，台北，台灣。

[100] 汤任基，1996，裂纹柱的扭转理论，上海交通大學出版社，上海，中國。

Appendix 1 Calculation for the forcing term in the anti-plane piezoelectricity formulation

According to the constitutive equation due to the coupling behavior in Eq. (3-4), the displacement and traction fields in the infinite medium due to the far-field shear σ_{zx}^{∞}, σ_{zy}^{∞} and electric field E_x^{∞}, E_y^{∞} in Fig. 3-2 (c) yield

$$w^{\infty} = \frac{\sigma_{zx}^{\infty} + e_{15}^M E_x^{\infty}}{c_{44}^M} x + \frac{\sigma_{zy}^{\infty} + e_{15}^M E_y^{\infty}}{c_{44}^M} y \,, \tag{A1-1}$$

$$t^{\infty} = \frac{\partial w^{\infty}}{\partial \mathrm{n}} = -(\frac{\sigma_{zx}^{\infty} + e_{15}^M E_x^{\infty}}{c_{44}^M} n_x + \frac{\sigma_{zy}^{\infty} + e_{15}^M E_y^{\infty}}{c_{44}^M} n_y) \,, \tag{A1-2}$$

where the unit outward normal vector on the boundary is $\mathrm{n} = (n_x, n_y)$. By comparing Eq. (3-11) with the first row of Eq. (3-19), we have

$$\{\mathbf{a}\} = \left[\mathbf{T}^M\right]\{\mathbf{w}^{\infty}\} - \left[\mathbf{U}^M\right]\{\mathbf{t}^{\infty}\}. \tag{A1-3}$$

For the circular boundary where the original system is located, the boundary conditions due to the far-field shear and electric field are

$$w_1^{\infty} = \frac{\sigma_{zx}^{\infty} + e_{15}^M E_x^{\infty}}{c_{44}^M} r_1 \cos\theta_1 + \frac{\sigma_{zy}^{\infty} + e_{15}^M E_y^{\infty}}{c_{44}^M} r_1 \sin\theta_1 \,, \tag{A1-4}$$

$$t_1^{\infty} = -(\frac{\sigma_{zx}^{\infty} + e_{15}^M E_x^{\infty}}{c_{44}^M} \cos\theta_1 + \frac{\sigma_{zy}^{\infty} + e_{15}^M E_y^{\infty}}{c_{44}^M} \sin\theta_1) \,. \tag{A1-5}$$

Considering the boundary condition, due to the far-field shear and electric field, on the *kth* circular boundary with respect to the observer system, we have

$$w_k^{\infty} = \frac{\sigma_{zx}^{\infty} + e_{15}^M E_x^{\infty}}{c_{44}^M} (e_x + r_k \cos\theta_k) + \frac{\sigma_{zy}^{\infty} + e_{15}^M E_y^{\infty}}{c_{44}^M} (e_y + r_k \sin\theta_k) \,, \tag{A1-6}$$

$$t_k^{\infty} = -(\frac{\sigma_{zx}^{\infty} + e_{15}^M E_x^{\infty}}{c_{44}^M} \cos\theta_k + \frac{\sigma_{zy}^{\infty} + e_{15}^M E_y^{\infty}}{c_{44}^M} \sin\theta_k) \,, \tag{A1-7}$$

where e_x and e_y respectively denote the eccentric distance of *kth* inclusion in the x and y direction. By comparing Eq. (A1-5) with Eq. (A1-7), we find that t^{∞} can

be described in any observer system without any change, where θ_k denotes the polar angle in the adaptive observer coordinate system. For the forcing term $\{\mathbf{b}\}$ due to the far-field electric field without the coupling behavior, it can be obtained in a similar way as the forcing term $\{\mathbf{a}\}$.

Appendix 2 Calculation for the forcing term in the anti-plane elasticity formulation

According to Eqs. (4-2) and (4-3), the displacement and traction fields in the infinite medium due to the remote shear σ_{zx}^{∞} and σ_{zy}^{∞} in Fig. 4-1 (d) are

$$w^{\infty} = \frac{\sigma_{zx}^{\infty}}{\mu_0} x + \frac{\sigma_{zy}^{\infty}}{\mu_0} y, \tag{A2-1}$$

$$t^{\infty} = \frac{\partial w^{\infty}}{\partial n} = -(\frac{\sigma_{zx}^{\infty}}{\mu_0} n_x + \frac{\sigma_{zy}^{\infty}}{\mu_0} n_y), \tag{A2-2}$$

where the unit outward normal vector on the boundary is $n = (n_x, n_y)$. By comparing Eq. (4-8) with the first low of Eq. (4-13), we have

$$\{c\} = [T^M]\{w^{\infty}\} - [U^M]\{t^{\infty}\}. \tag{A2-3}$$

For the circular boundary where the original system is located, the boundary conditions due to the remote shear are

$$w_1^{\infty} = \frac{\sigma_{zx}^{\infty}}{\mu_0} r_1 \cos\theta_1 + \frac{\sigma_{zy}^{\infty}}{\mu_0} r_1 \sin\theta_1, \tag{A2-4}$$

$$t_1^{\infty} = -(\frac{\sigma_{zx}^{\infty}}{\mu_0} \cos\theta_1 + \frac{\sigma_{zy}^{\infty}}{\mu_0} \sin\theta_1). \tag{A2-5}$$

Considering the boundary condition, due to the remote shear, on the *kth* circular boundary with respect to the observer system, we have

$$w_k^{\infty} = \frac{\sigma_{zx}^{\infty}}{\mu_0}(e_x + r_k \cos\theta_k) + \frac{\sigma_{zy}^{\infty}}{\mu_0}(e_y + r_k \sin\theta_k), \tag{A2-6}$$

$$t_k^{\infty} = -(\frac{\sigma_{zx}^{\infty}}{\mu_0} \cos\theta_k + \frac{\sigma_{zy}^{\infty}}{\mu_0} \sin\theta_k), \tag{A2-7}$$

where e_x and e_y respectively denote the eccentric distance of *kth* inclusion in the x and y direction, and θ_k is the polar angle in the adaptive observer coordinate system. It is found that t^{∞} can be described in any observer system without changes.

Appendix 3 Derivation of the exact solution for a single elastic inclusion

We derive the exact solution for anti-plane problem with a single elastic inclusion under the remote shear using the present formulation. The infinite medium under the shear stress $\sigma_{zx}^{\infty} = 0$ and $\sigma_{zy}^{\infty} = \tau_{\infty}$ at infinity is considered. The Fourier coefficients in Eq. (4-8) can be written as

$$\{\mathbf{w}^{\infty}\} = \begin{Bmatrix} 0 \\ 0 \\ \dfrac{\tau_{\infty} r_1}{\mu_0} \\ \vdots \\ 0 \\ 0 \end{Bmatrix}_{(2L+1)\times 1} , \quad \{\mathbf{t}^{\infty}\} = \begin{Bmatrix} 0 \\ 0 \\ -\dfrac{\tau_{\infty}}{\mu_0} \\ \vdots \\ 0 \\ 0 \end{Bmatrix}_{(2L+1)\times 1} , \tag{A3-1}$$

where r_1 is the radius of the single inclusion. By substituting the appropriate degenerate kernels in Eqs. (2-16) and (2-17) into Eqs. (4-8), (4-9) and employing the continuity of displacement and the equilibrium of traction along the interface in Eqs. (4-10) and (4-11), the unknown boundary data in Eq. (4-13) can be obtained using the symbolic software Mathematica as shown below:

$$\{\mathbf{w}^{M}\} = \begin{Bmatrix} 0 \\ 0 \\ \dfrac{2\tau_{\infty} r_1}{\mu_0 + \mu_1} \\ \vdots \\ 0 \\ 0 \end{Bmatrix}_{(2L+1)\times 1} , \quad \{\mathbf{t}^{M}\} = \begin{Bmatrix} 0 \\ 0 \\ \dfrac{-2\tau_{\infty} \mu_1}{\mu_0(\mu_0 + \mu_1)} \\ \vdots \\ 0 \\ 0 \end{Bmatrix}_{(2L+1)\times 1} , \tag{A3-2}$$

$$\{\mathbf{w}^I\} = \begin{Bmatrix} 0 \\ 0 \\ \dfrac{2\tau_\infty r_1}{\mu_0 + \mu_1} \\ \vdots \\ 0 \\ 0 \end{Bmatrix}_{(2L+1)\times 1} \quad , \quad \{\mathbf{t}^I\} = \begin{Bmatrix} 0 \\ 0 \\ \dfrac{2\tau_\infty}{\mu_0 + \mu_1} \\ \vdots \\ 0 \\ 0 \end{Bmatrix}_{(2L+1)\times 1} . \tag{A3-3}$$

After substituting Eqs. (A3-1) and (A3-2) into the boundary integral equation for the domain point in Eq. (2-11), we obtain the total stress fields in the matrix

$$\sigma_{zx}^M = \mu_0 \frac{\partial w^M}{\partial x} + \sigma_{zx}^\infty = -2\tau_\infty \frac{r_1^2}{\rho^2} \frac{\mu_0 - \mu_1}{\mu_0 + \mu_1} \sin\phi \cos\phi , \tag{A3-4}$$
$$r_1 \le \rho \le \infty, \ \ 0 \le \phi \le 2\pi ,$$

$$\sigma_{zy}^M = \mu_0 \frac{\partial w^M}{\partial y} + \sigma_{zy}^\infty = \tau_\infty \frac{r_1^2}{\rho^2} \frac{\mu_0 - \mu_1}{\mu_0 + \mu_1} (\cos^2\phi - \sin^2\phi) + \tau_\infty , \tag{A3-5}$$
$$r_1 \le \rho \le \infty, \ \ 0 \le \phi \le 2\pi .$$

After substituting Eq. (A3-10) into the boundary integral equation for the domain point in Eq. (2-11), we have the total stress fields in the inclusion

$$\sigma_{zx}^I = \mu_1 \frac{\partial w^I}{\partial x} = 0, \ \ 0 \le \rho \le r_1, \ \ 0 \le \phi \le 2\pi , \tag{A3-6}$$

$$\sigma_{zy}^I = \mu_1 \frac{\partial w^I}{\partial y} = 2\tau_\infty \frac{\mu_1}{\mu_0 + \mu_1}, \ \ 0 \le \rho \le r_1, \ \ 0 \le \phi \le 2\pi . \tag{A3-7}$$

Finally, the stress components σ_{zr} and $\sigma_{z\theta}$ in Eqs. (4-6) and (4-7) can be superimposed by using σ_{zx} and σ_{zy} as shown below:

$$\sigma_{zr}^M = 2\tau_\infty \frac{r_1^2}{\rho^2} \frac{\mu_1}{\mu_0 + \mu_1} \sin\phi, \ \ r_1 \le \rho \le \infty, \ \ 0 \le \phi \le 2\pi , \tag{A3-8}$$

$$\sigma_{z\theta}^M = 2\tau_\infty \frac{r_1^2}{\rho^2} \frac{\mu_0}{\mu_0 + \mu_1} \cos\phi, \ \ r_1 \le \rho \le \infty, \ \ 0 \le \phi \le 2\pi , \tag{A3-9}$$

$$\sigma_{zr}^I = 2\tau_\infty \frac{\mu_1}{\mu_0 + \mu_1} \sin\phi, \ \ 0 \le \rho \le r_1, \ \ 0 \le \phi \le 2\pi , \tag{A3-10}$$

$$\sigma_{z\theta}^I = 2\tau_\infty \frac{\mu_1}{\mu_0 + \mu_1} \cos\phi, \ \ 0 \le \rho \le r_1, \ \ 0 \le \phi \le 2\pi . \tag{A3-11}$$

It is obvious to see that the maximum stress concentration occurs at $\rho = r_1$ and $\phi = 0$. The stress concentration factor is reduced due to the inclusion in comparison with that of cavity ($\mu_1 = 0$) as shown in Eq. (A3-9). Besides, it is noted that σ_{zr}^M coincides with

σ_{zr}^{I} as required by the traction equilibrium on the interface between the matrix and inclusion. The exact solution for a single elastic inclusion using the present formulation matches well with the previous one obtained by employing the complex-variable formulation [56].

Appendix 4 Available results obtained by previous researchers
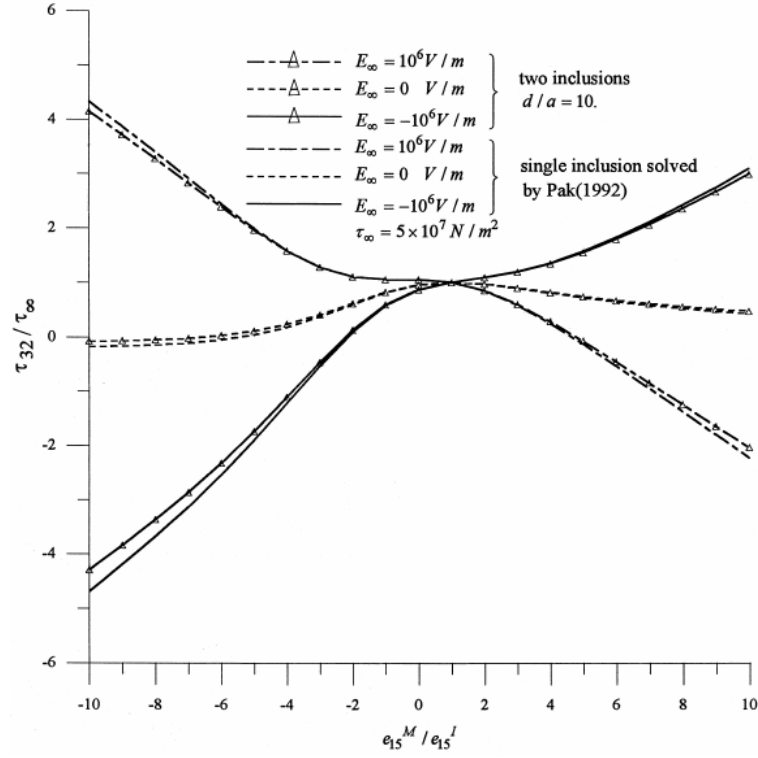
Chao and Chang's data [20] for Figure 3-4 (a)
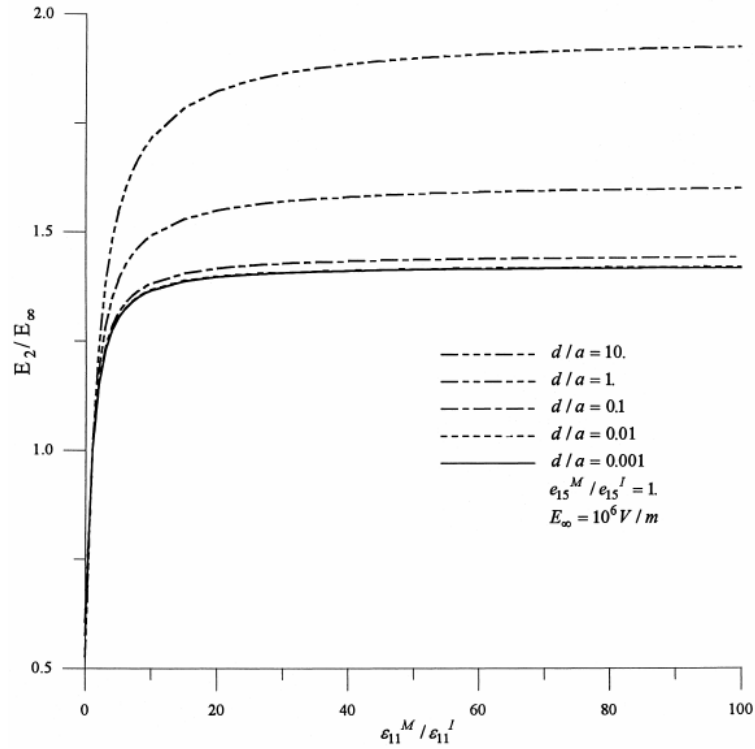
Chao and Chang's data [20] for Figure 3-5
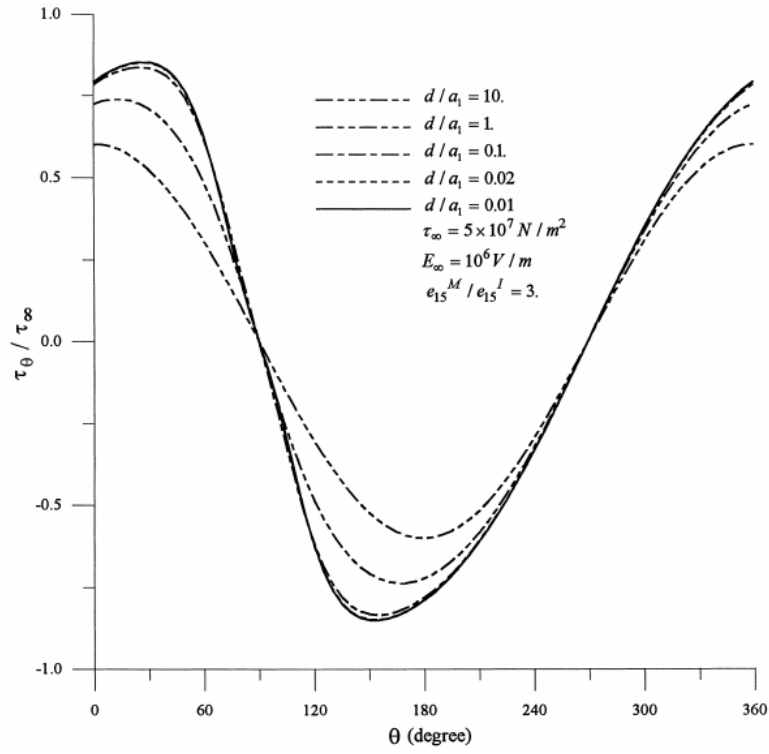
Chao and Chang's data [20] for Figure 3-6 (a)
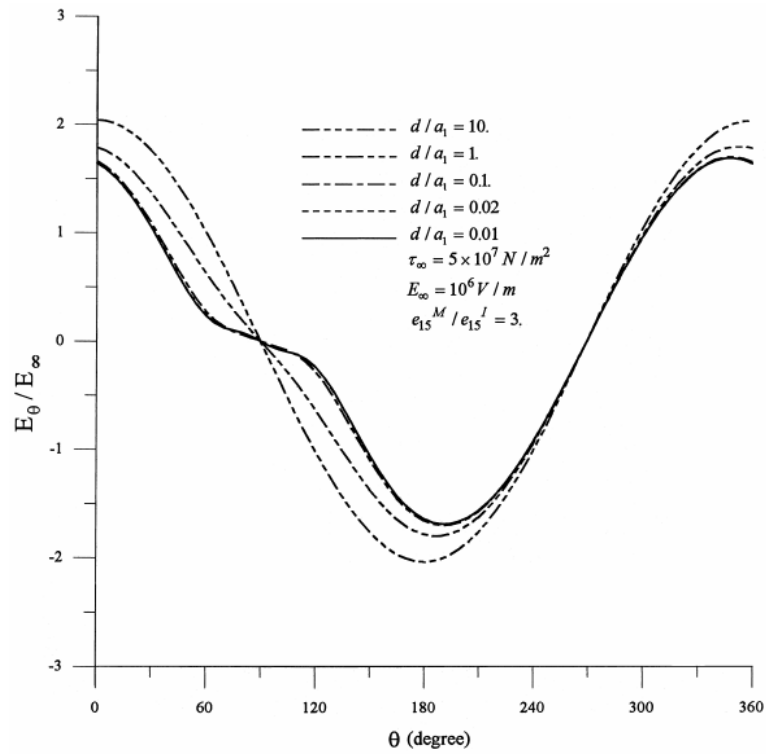
Chao and Chang's data [20] for Figure 3-6 (b)
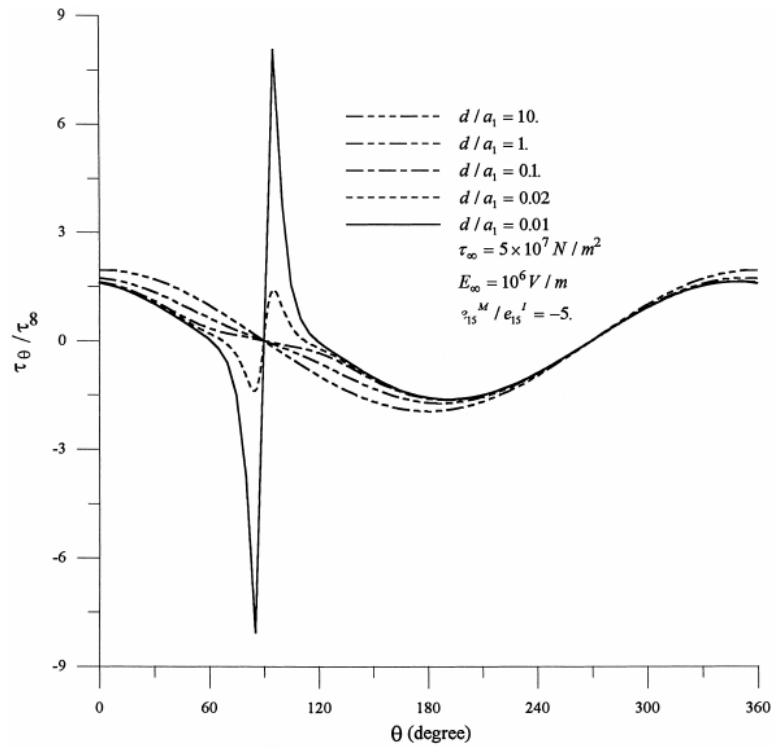
Chao and Chang's data [20] for Figure 3-8 (a)
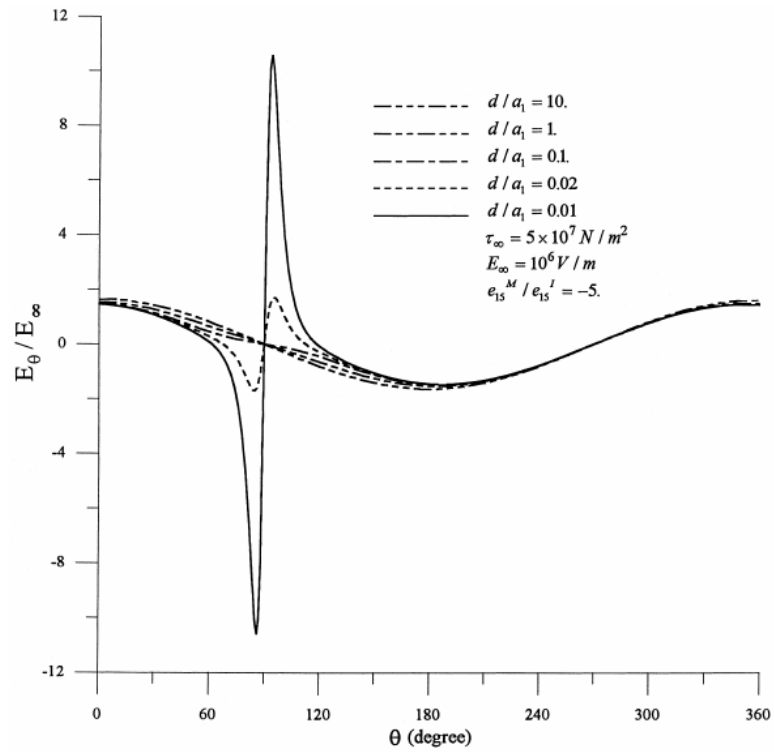
Chao and Chang's data [20] for Figure 3-8 (b)

130
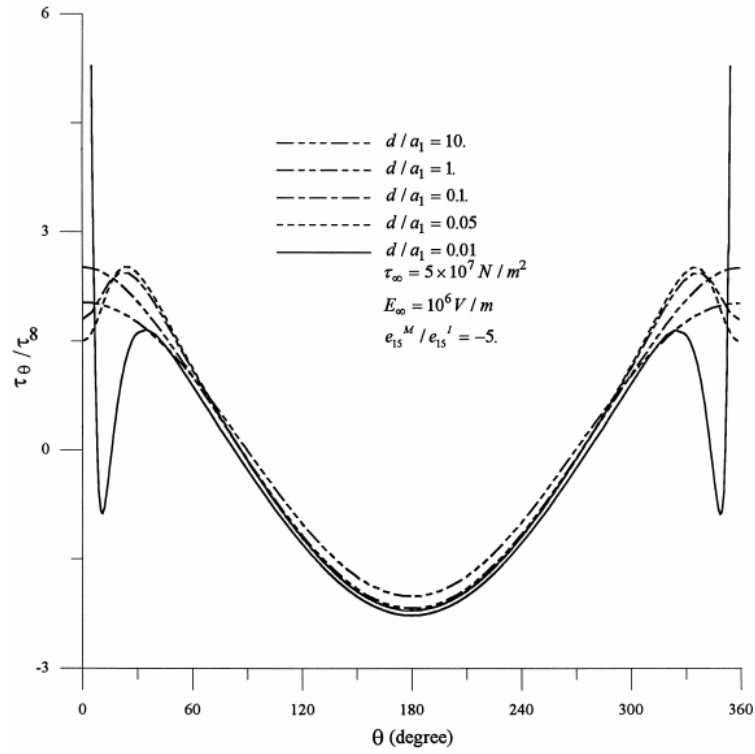
Chao and Chang's data [20] for Figure 3-10 (a)
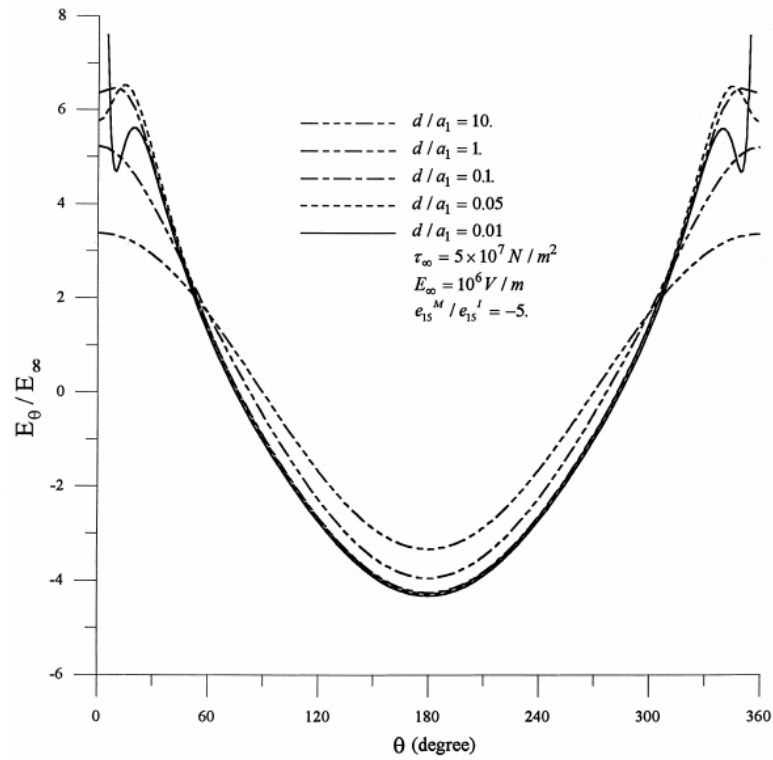
Chao and Chang's data [20] for Figure 3-10 (b)

131
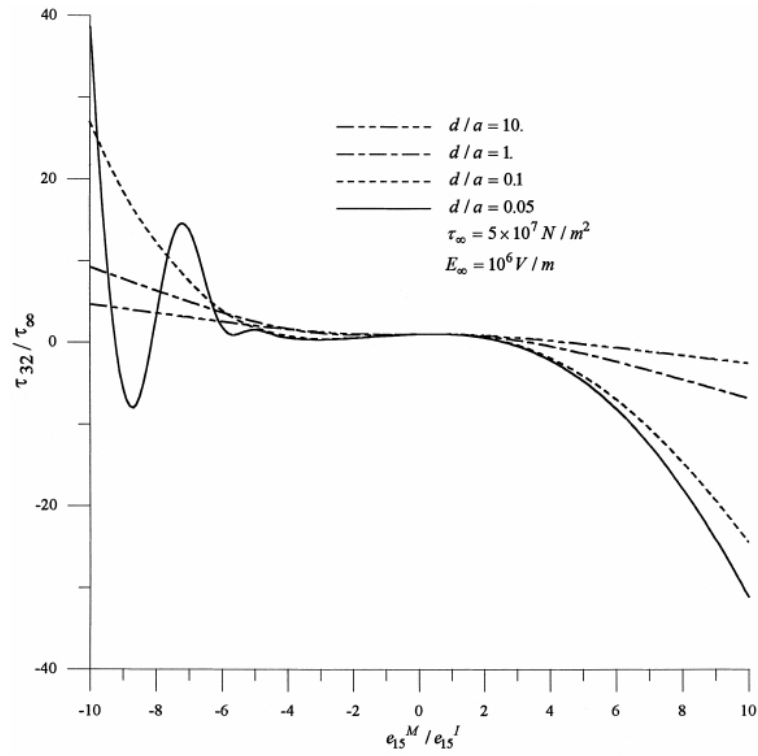
Chao and Chang's data [20] for Figure 3-11 (a)
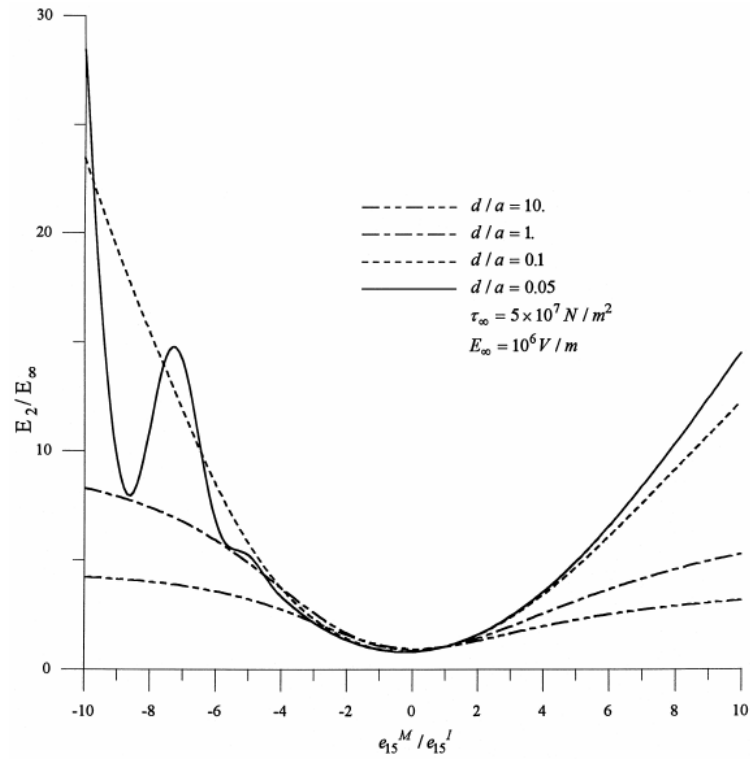
Chao and Chang's data [20] for Figure 3-11 (b)

132
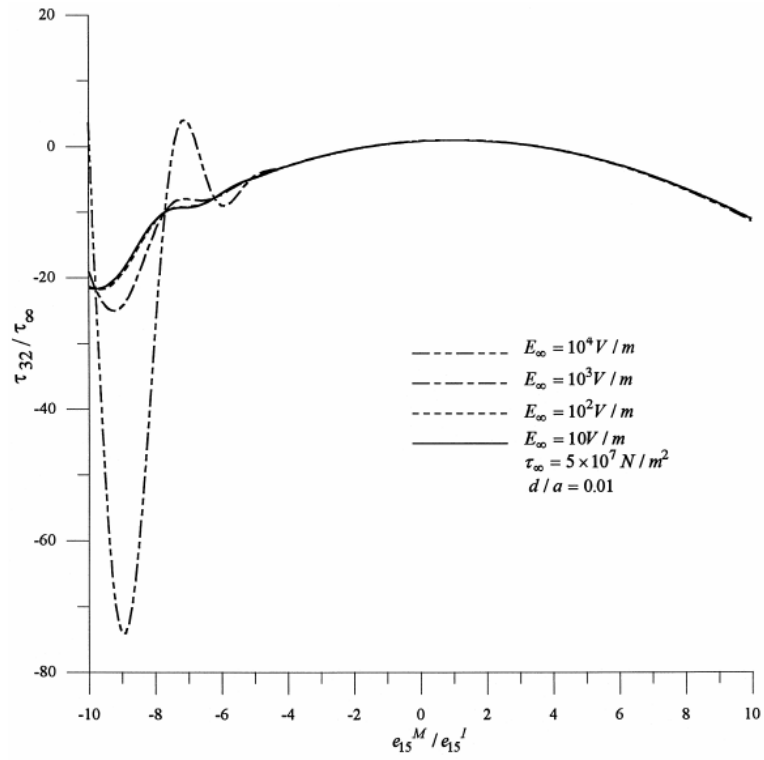
Chao and Chang's data [20] for Figure 3-12 (a)
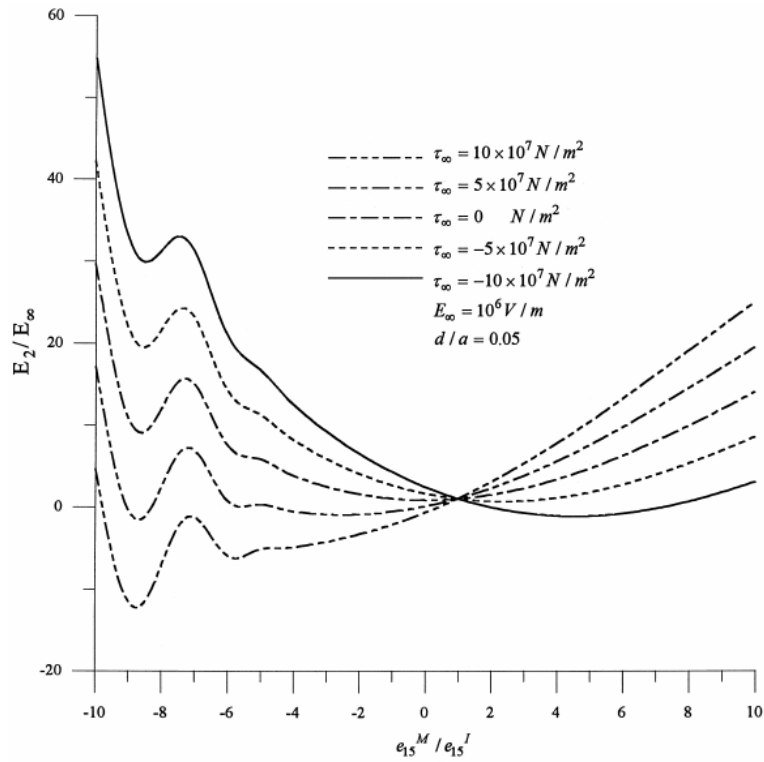
Chao and Chang's data [20] for Figure 3-12 (b)
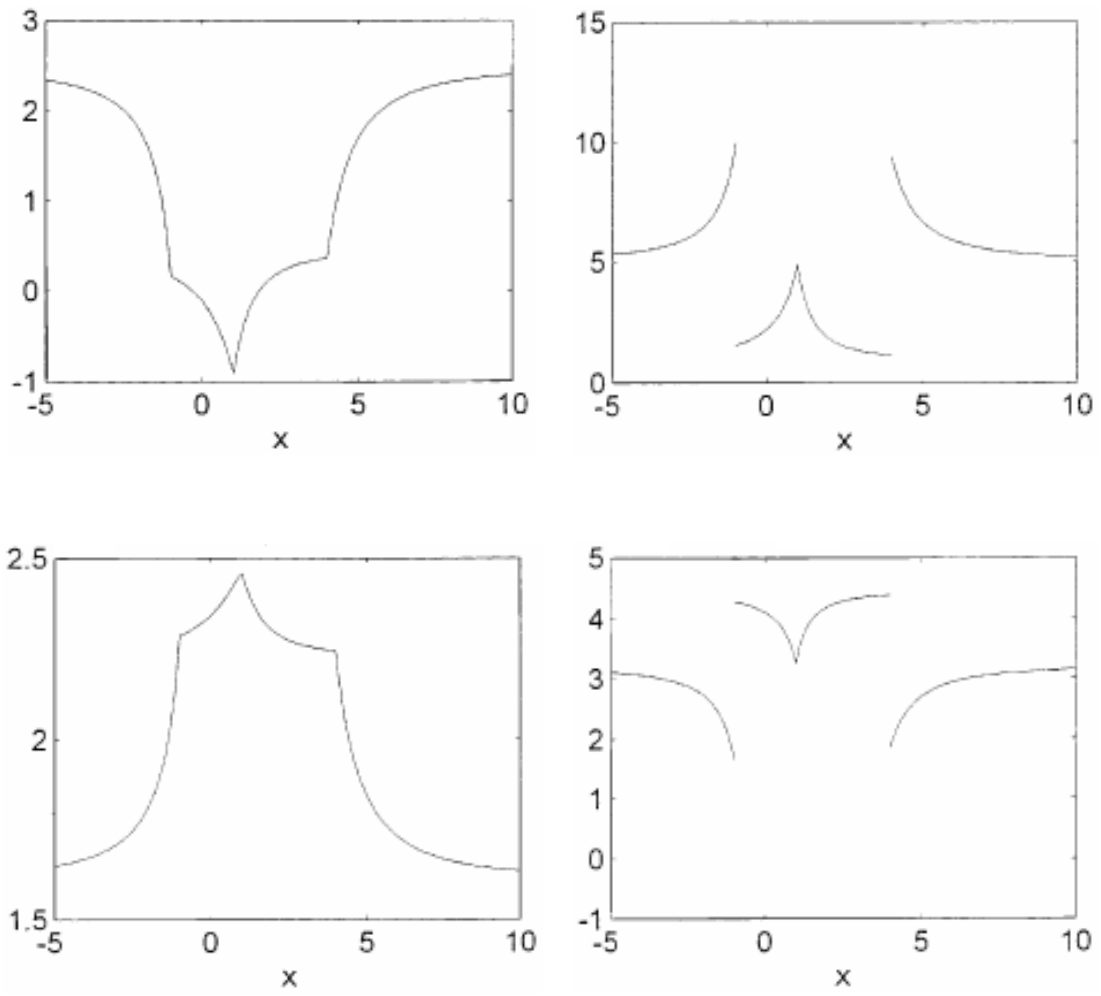
Wang and Shen's data [88] for Figure 3-13
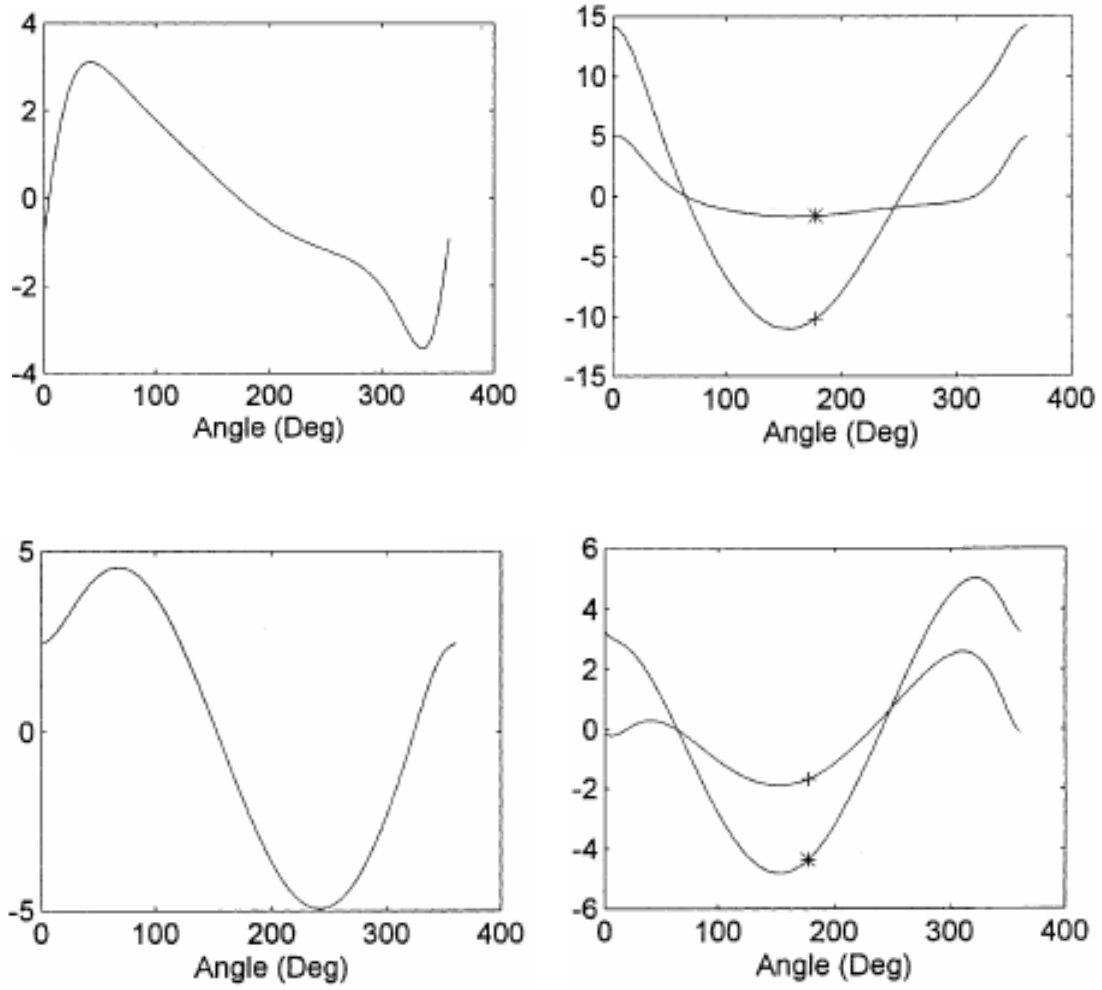
Wang and Shen's data [88] for Figure 3-14

135
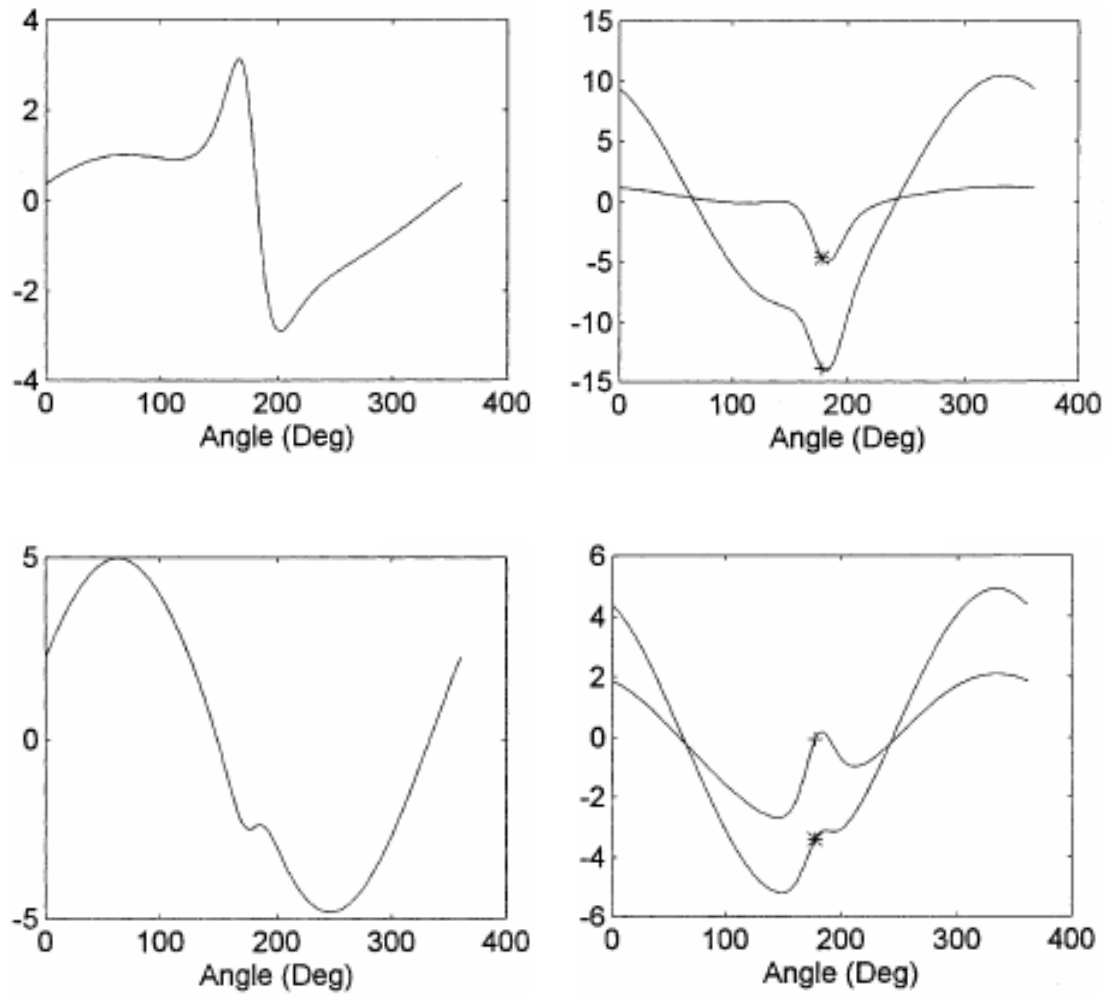
Wang and Shen's data [88] for Figure 3-15

136
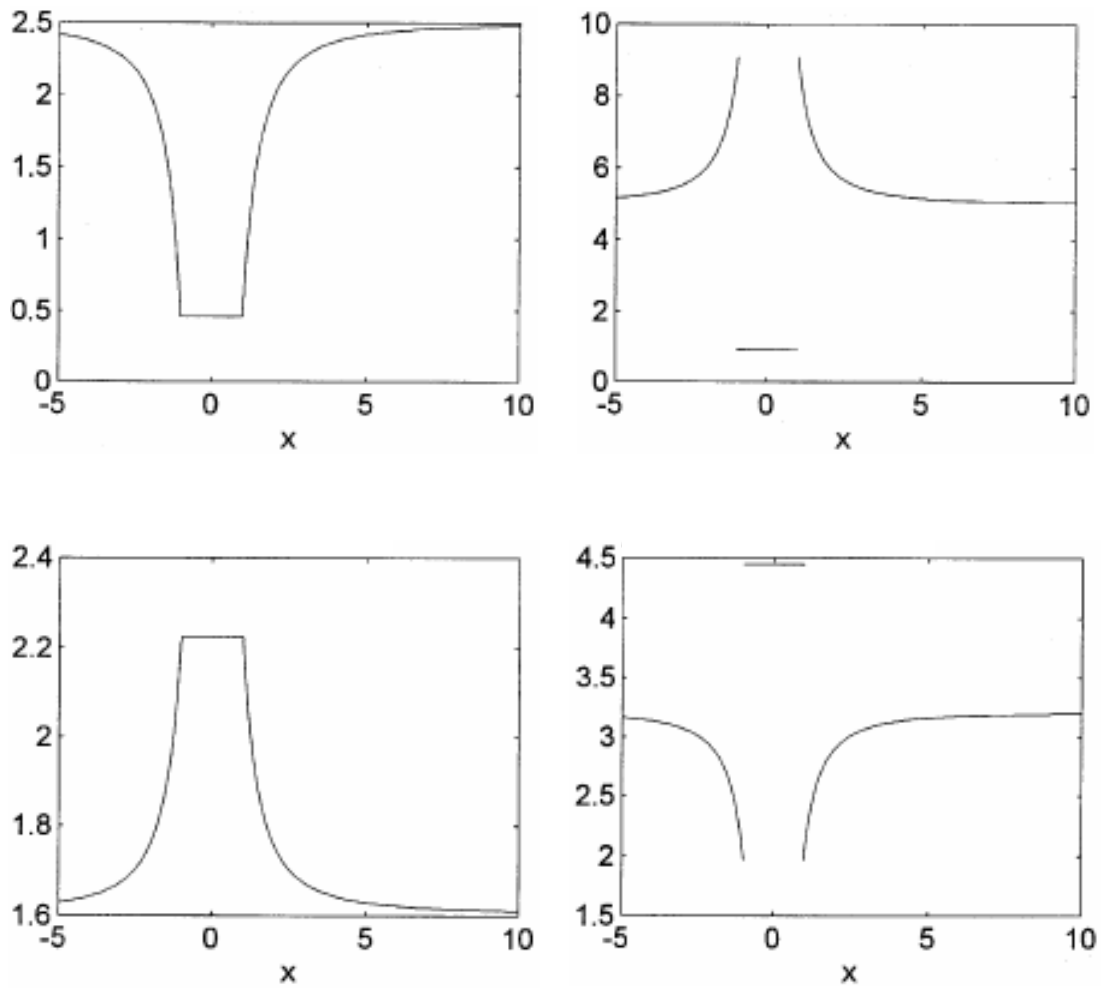
Wang and Shen's data [88] for Figure 3-16

137
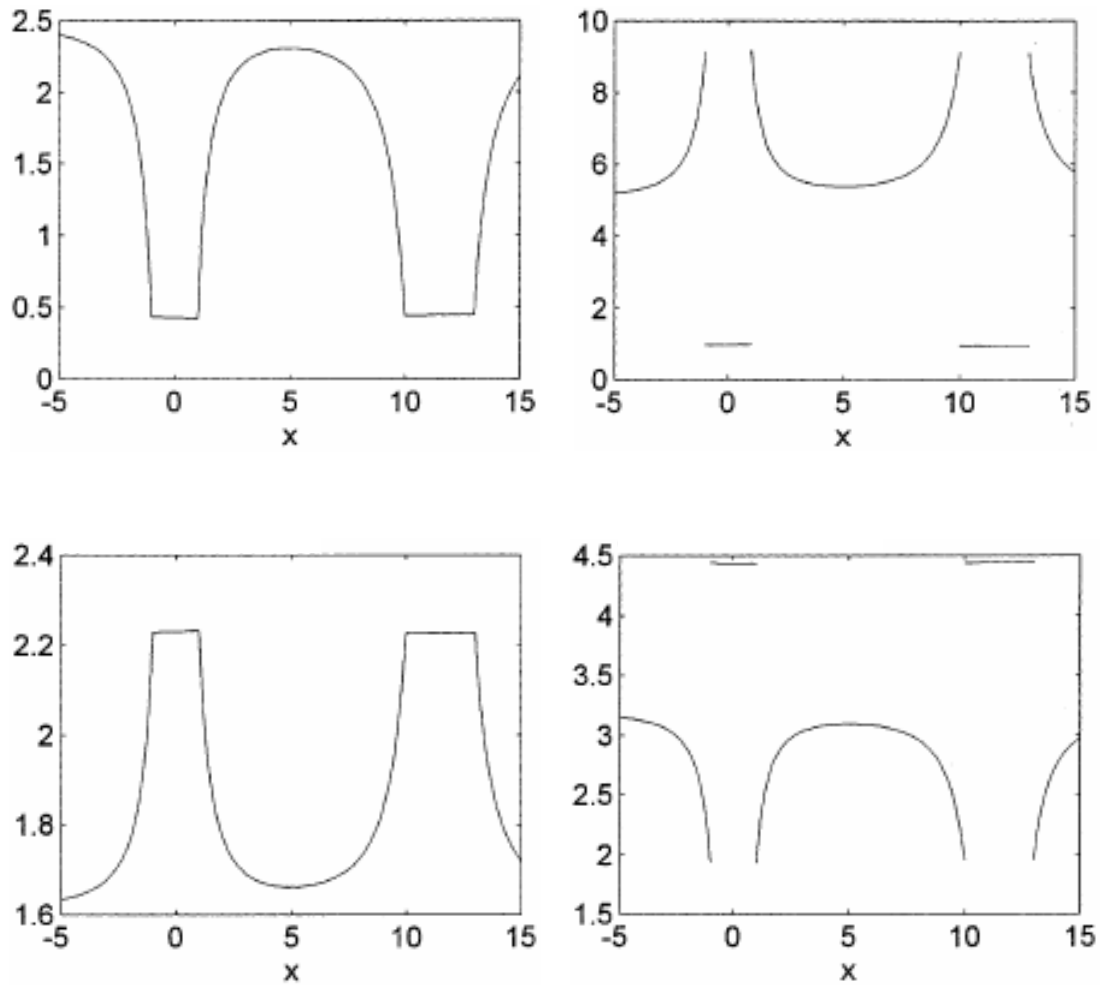
Wang and Shen's data [88] for Figure 3-17
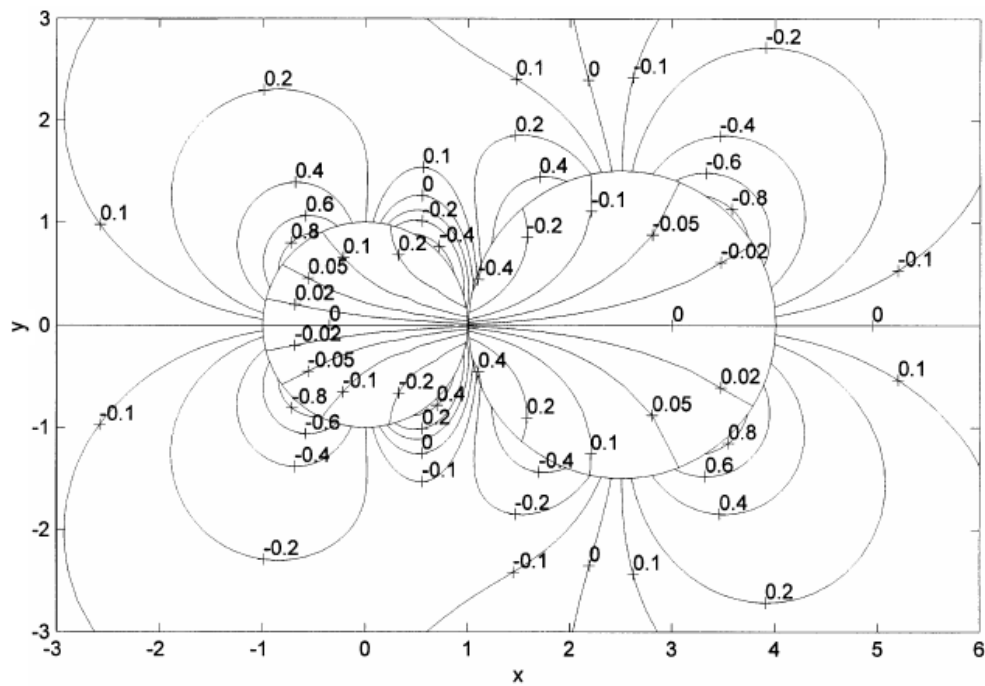
Wang and Shen's data [88] for Figure 3-18 (a)
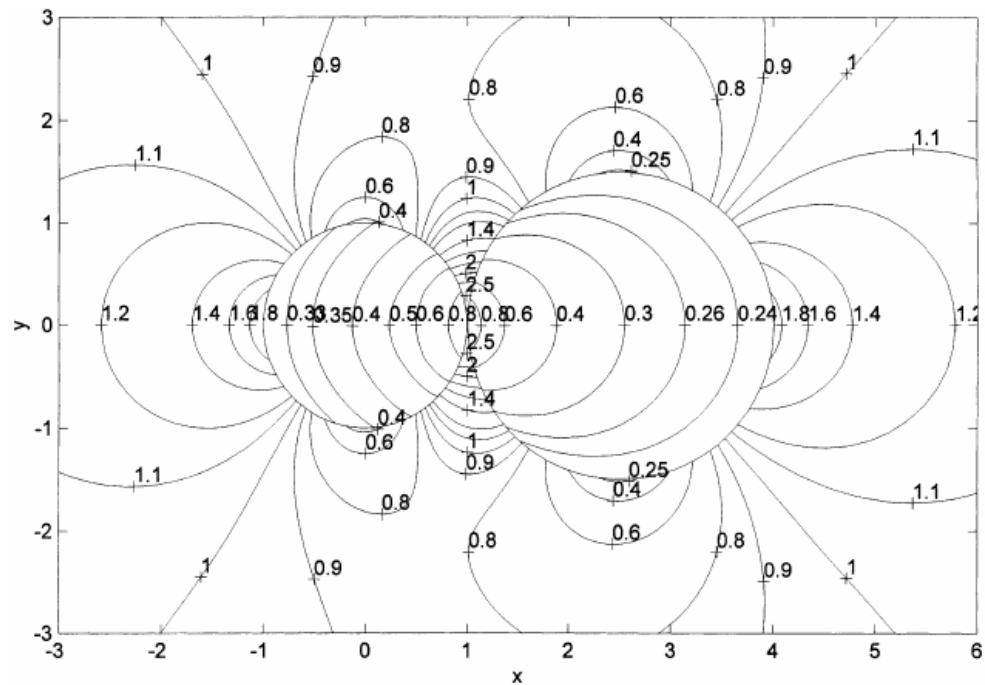
Wang and Shen's data [88] for Figure 3-18 (b)

139
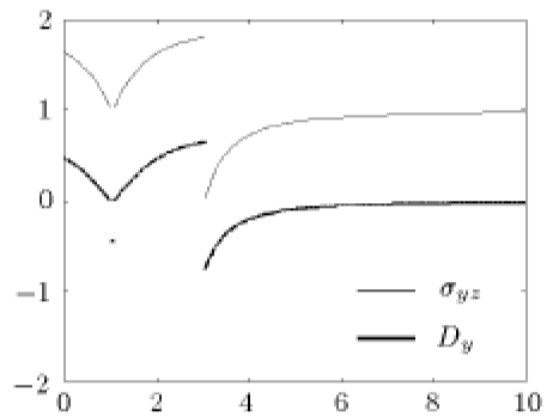
Wu and Funami's data [95] for Figure 3-19 (a)
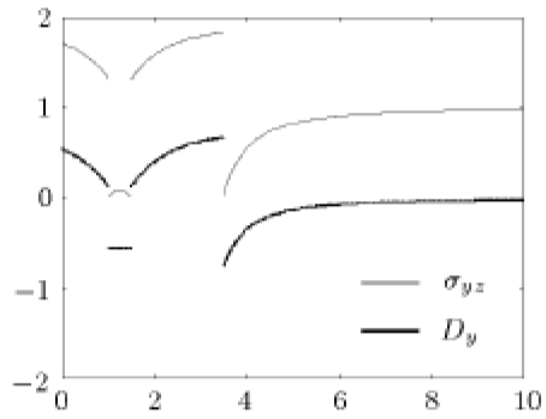
Wu and Funami's data [95] for Figure 3-19 (b)
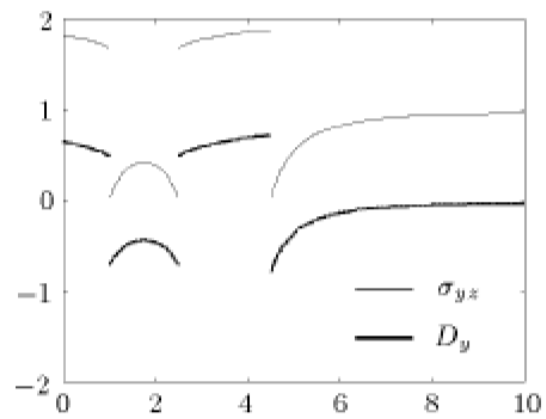
Wu and Funami's data [95] for Figure 3-19 (c)

140
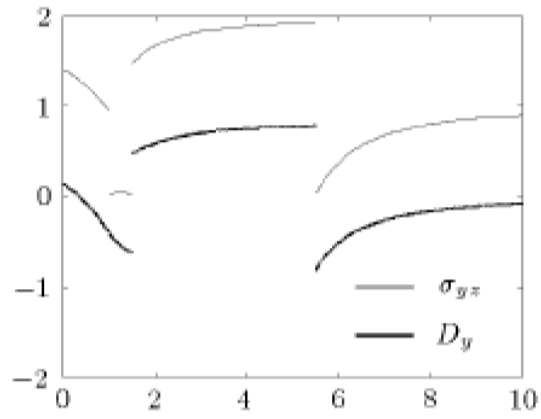
Wu and Funami's data [95] for Figure 3-20 (a)
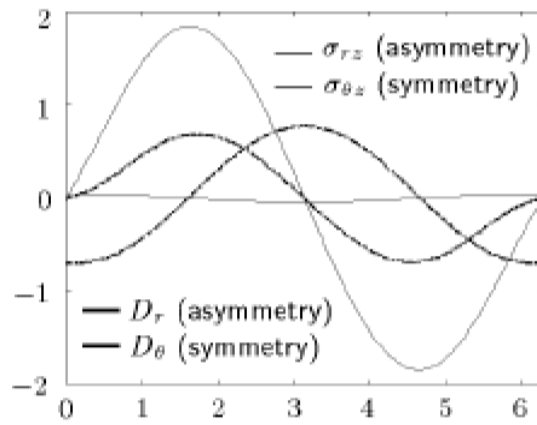
Wu and Funami's data [95] for Figure 3-20 (b)
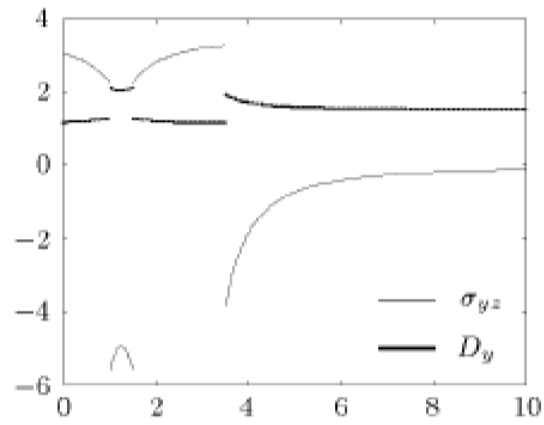
Wu and Funami's data [95] for Figure 3-21 (a)
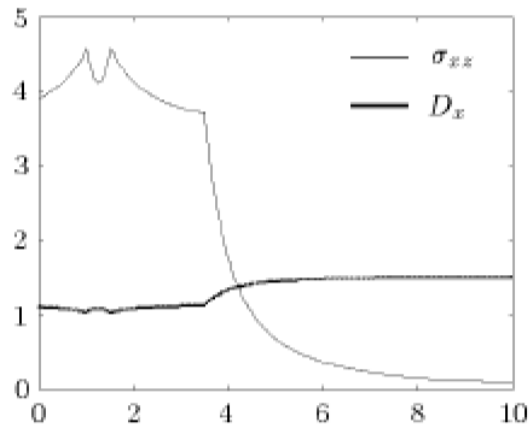
Wu and Funami's data [95] for Figure 3-21 (b)
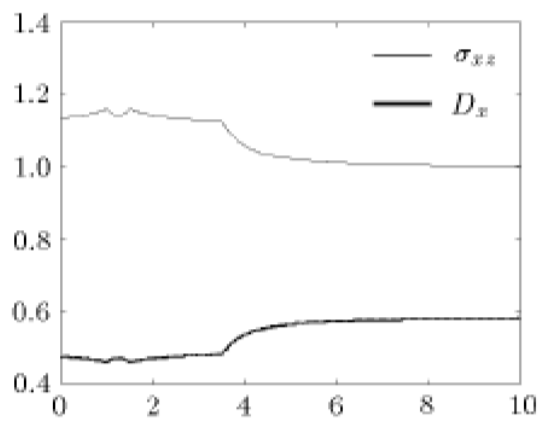
Wu and Funami's data [95] for Figure 3-21 (c)
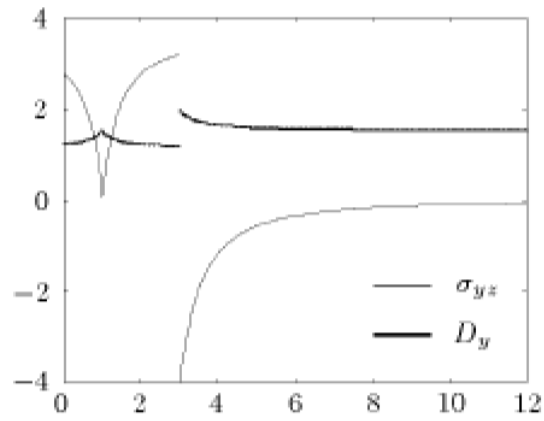
Wu and Funami's data [95] for Figure 3-22 (a)
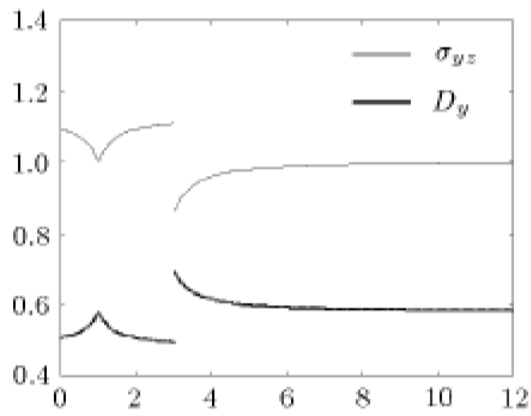
Wu and Funami's data [95] for Figure 3-22 (b)

143

$$E_x^\infty = E_\infty$$
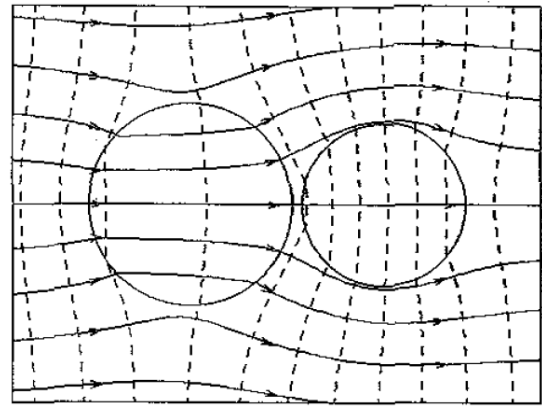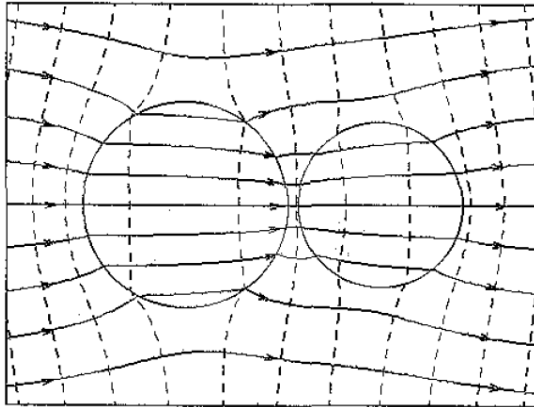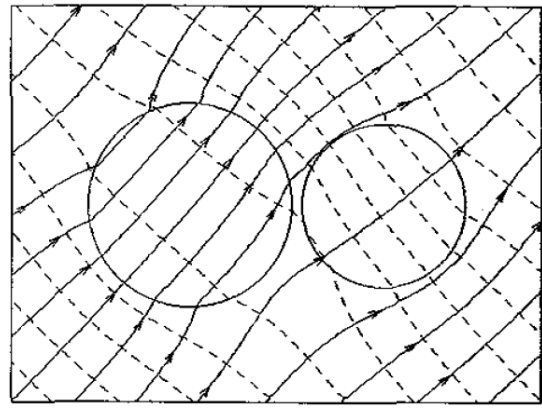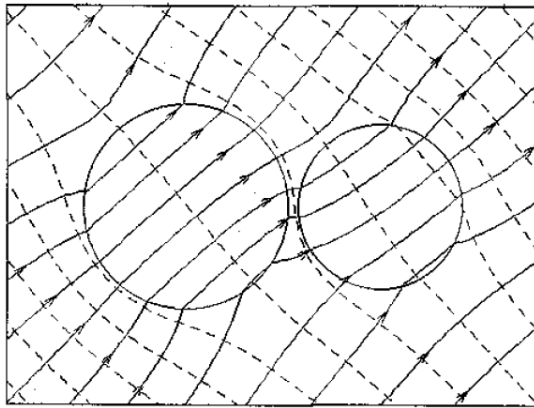
$$E_x^\infty = E_\infty \cos 45° \quad \text{and} \quad E_y^\infty = E_\infty \sin 45°$$
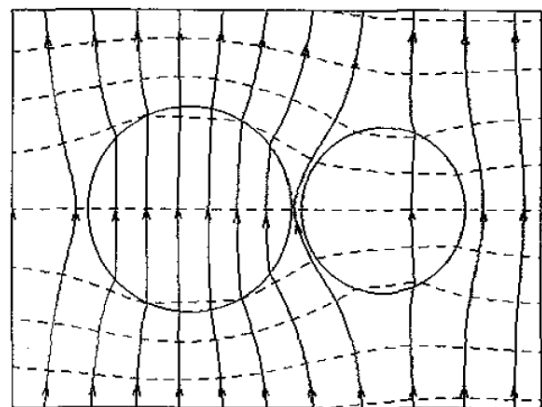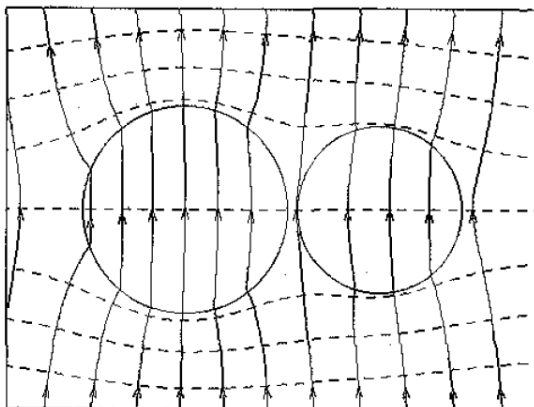
$$E_y^\infty = E_\infty$$

Emets and Onofrichuk's data [46] for   Emets and Onofrichuk's data [46] for
Figure 3-24 (a)   Figure 3-24 (b)

144
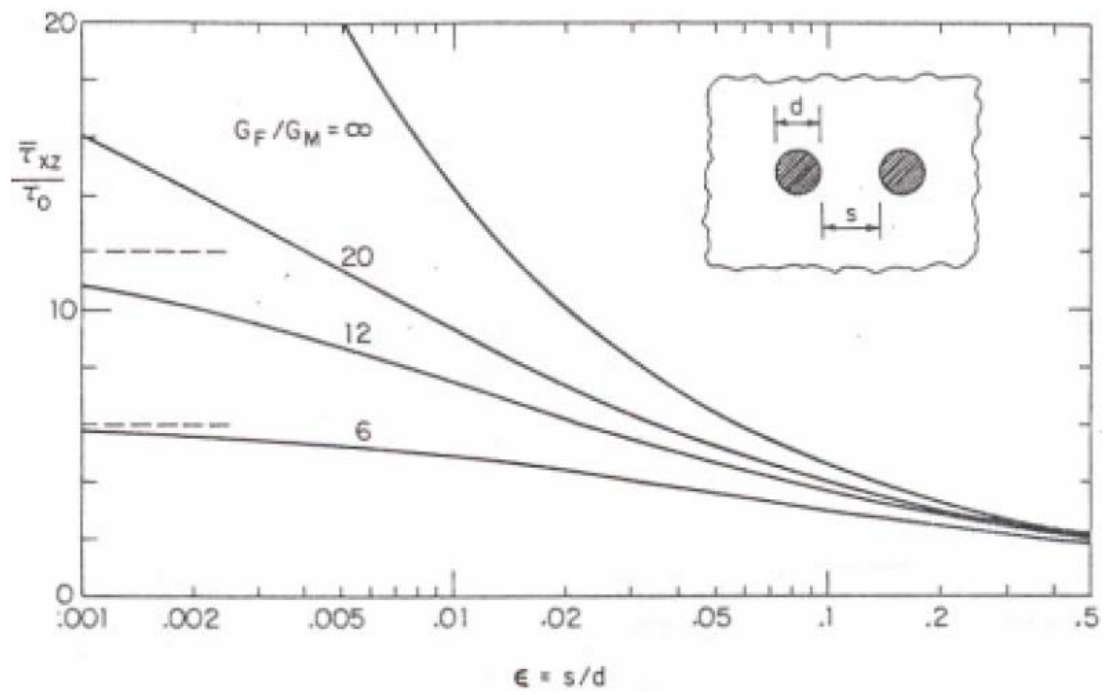
Budiansky and Carrier's data [15] for Figure 4-3 (b)
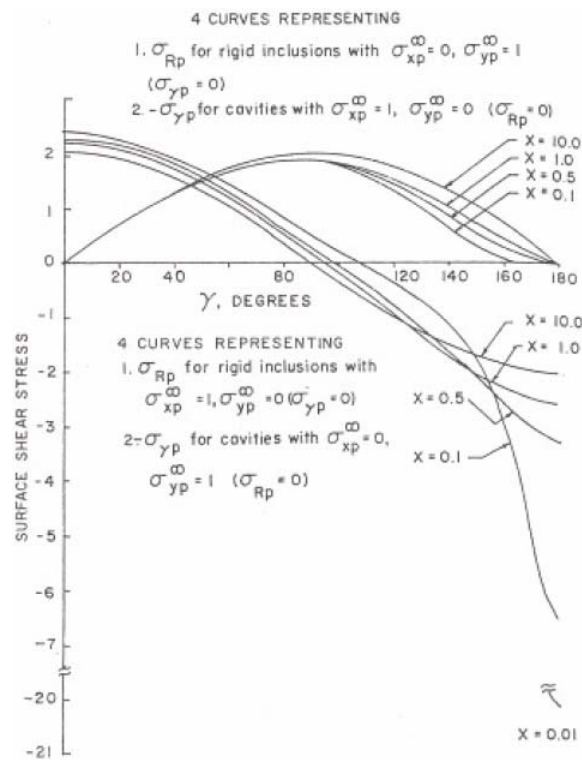
Goree and Wilson's data [50] for Figures 4-4 (b) and 4-4 (c)
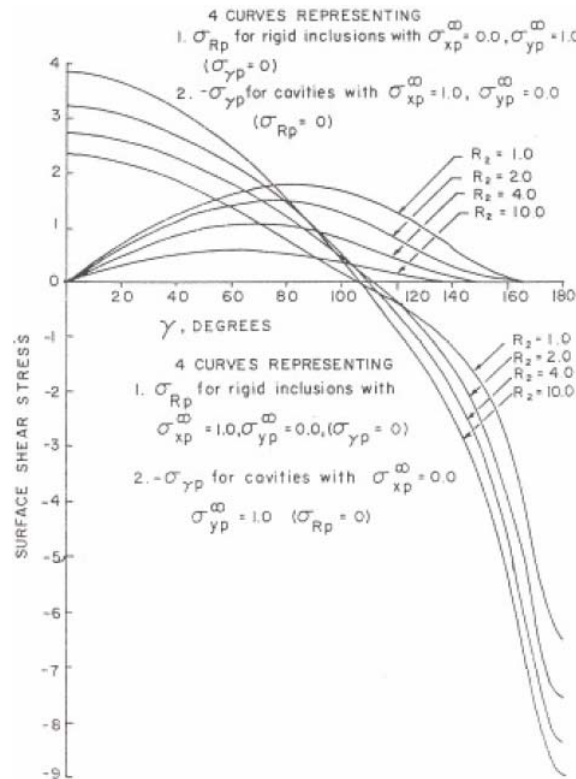
Goree and Wilson's data [50] for Figures 4-4 (d) and 4-4 (e)

146
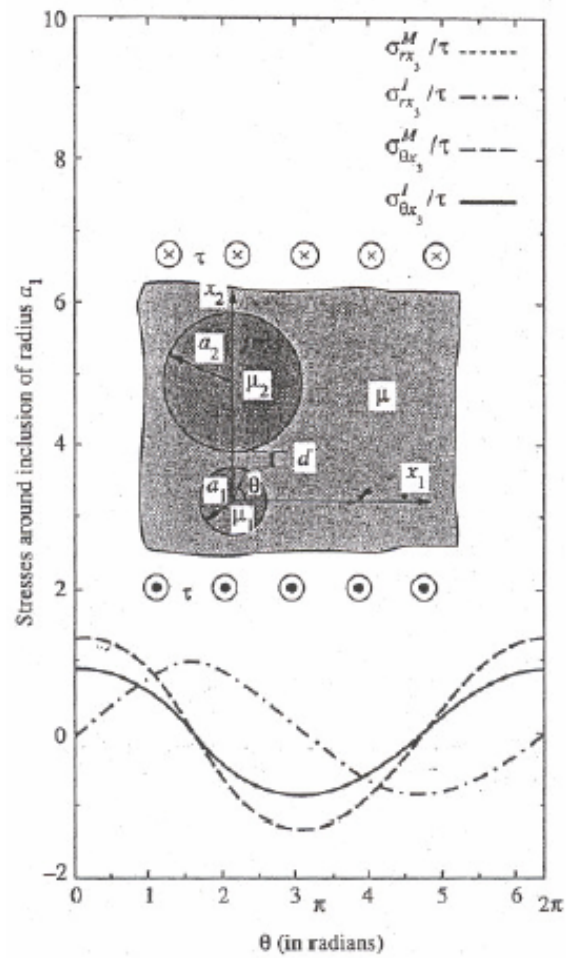
Honein *et al.*'s data [56] for Figure 4-5 (b)
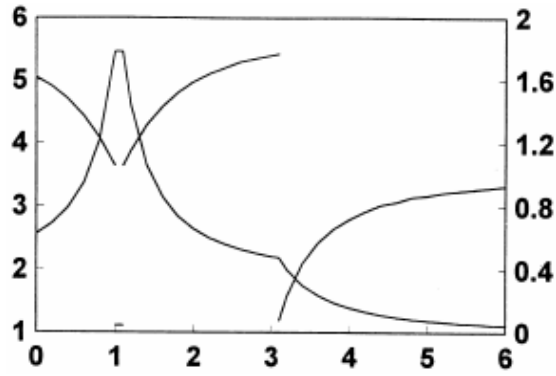
Wu's data [94] for Figure 4-6 (b)
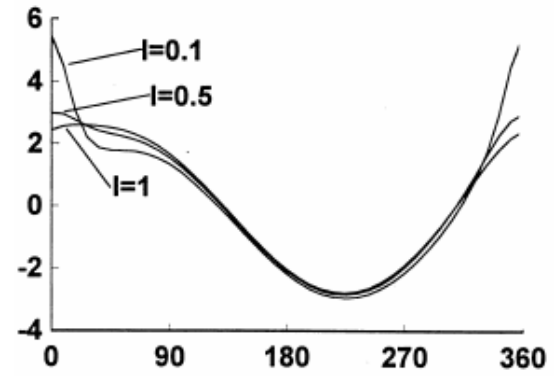
Wu's data [94] for Figure 4-6 (e)
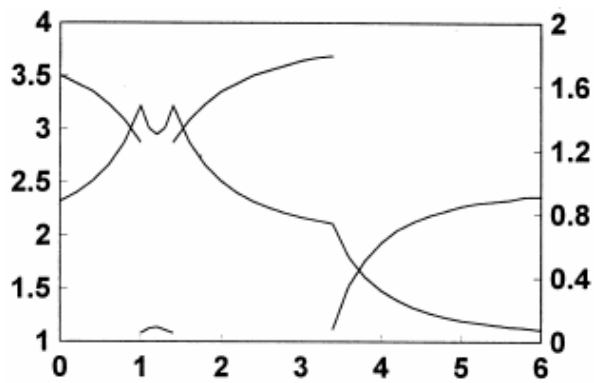
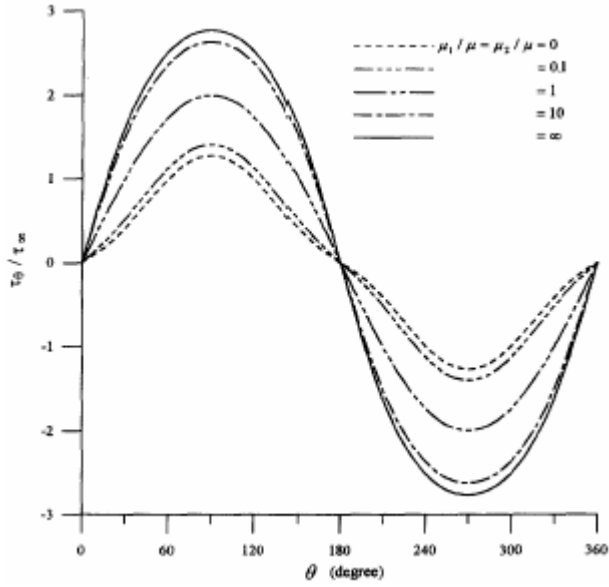Wu's data [94] for Figure 4-6 (c)
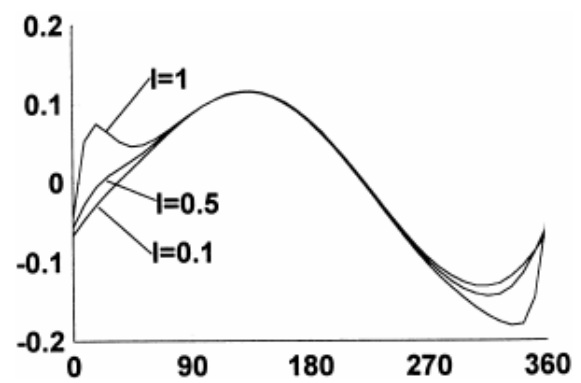
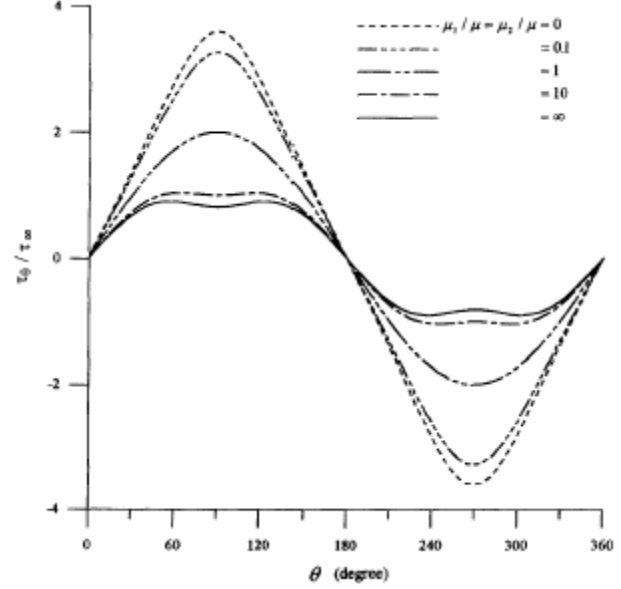Wu's data [94] for Figure 4-6 (f)
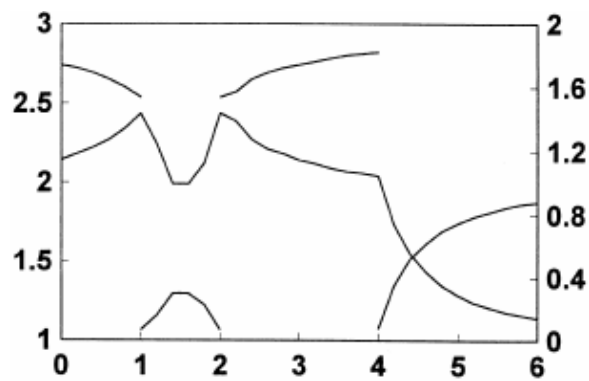
Wu's data [94] for Figure 4-6 (d)
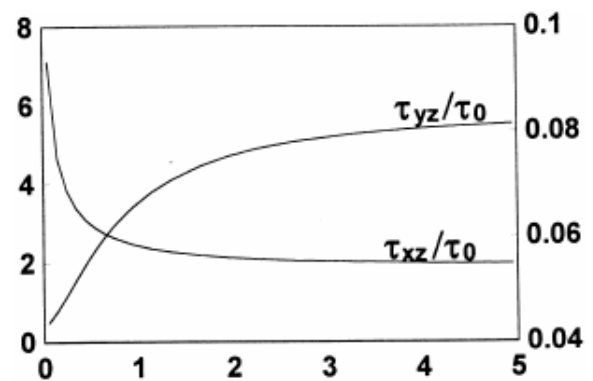
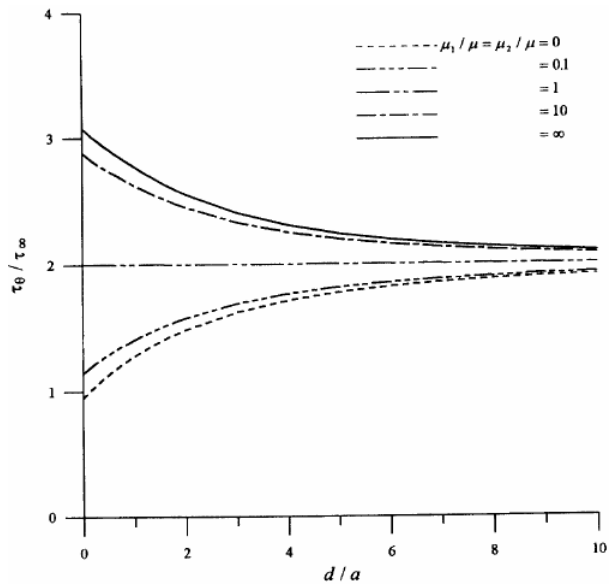Wu's data [94] for Figure 4-6 (g)
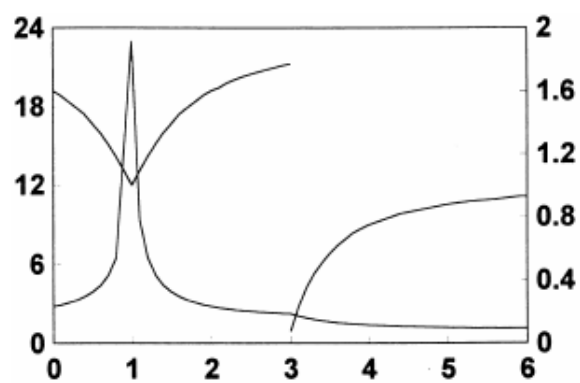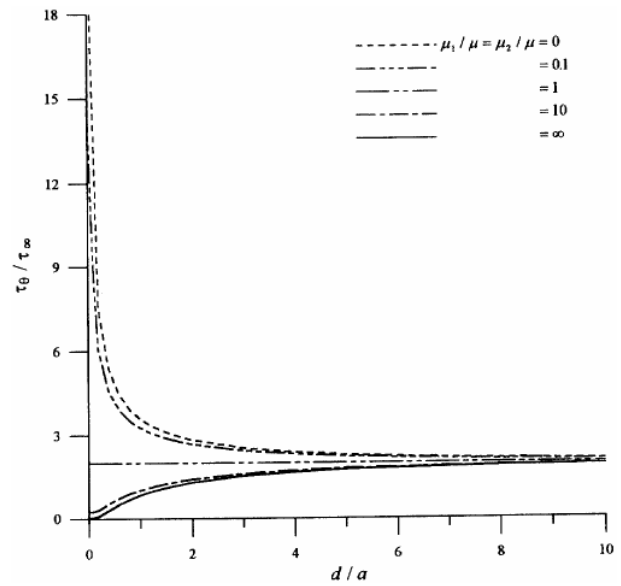
Wu's data [94] for Figure 4-6 (h)

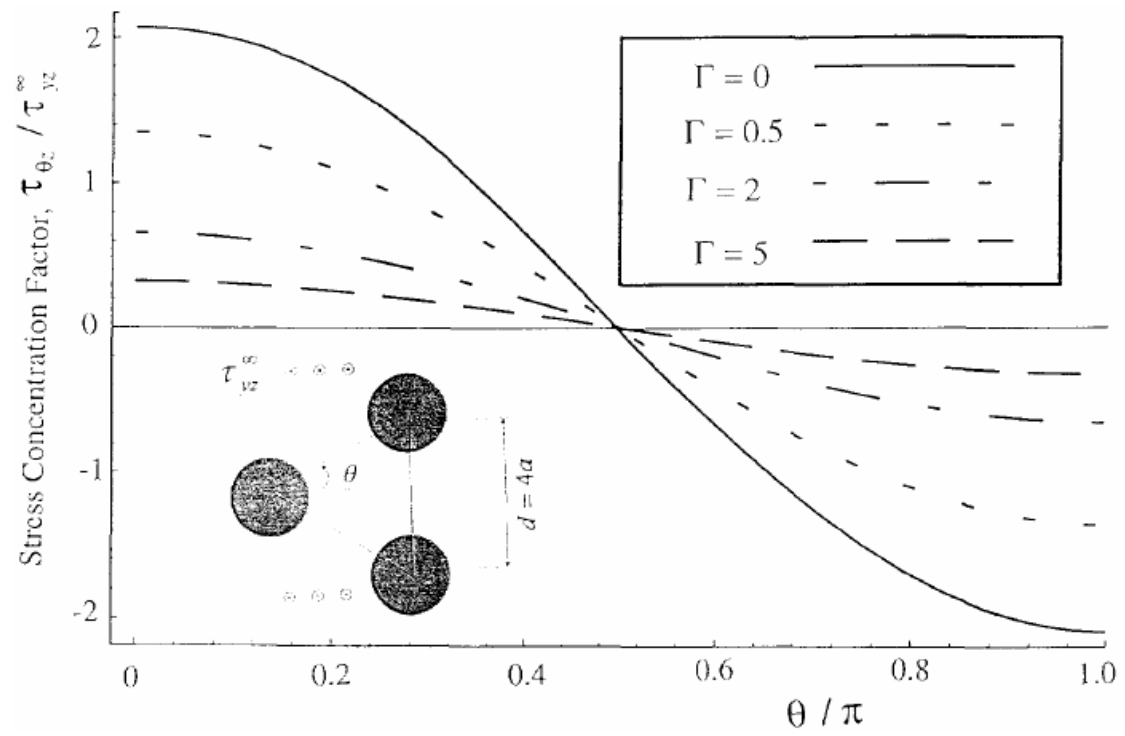Chao and Young's data [22] for Figure 4-7 (b)

Chao and Young's data [22] for Figure 4-7 (c)

Chao and Young's data [22] for Figure 4-7 (d)

Chao and Young's data [22] for Figure 4-7 (e)

150

Gong's data [48] for Figure 4-8 (b)

作者簡歷

中文姓名：吳安傑
英文姓名：An-Chien Wu
出生日期：民國 71 年 10 月 04 日
籍　　貫：台灣
聯絡地址：台北縣中和市復興路 328 號 4 樓
聯絡電話：(02) 2247-2903
行動電話：0910250435
電子信箱：*chien71@msn.com*
學　　歷：

國立台灣海洋大學河海工程研究所碩士 (2004.09 ~ 2006.06)
國立台灣海洋大學河海工程系學士 (2000.09 ~ 2004.06)
台北市立大同高級中學 (1997.09 ~ 2000.06)
台北縣立永和國民中學 (1994.09 ~ 1997.06)
台北縣立復興國民小學 (1988.09 ~ 1994.06)

著作目錄：

(A) 期刊論文

1　Chen JT, Shen WC and Wu AC, 2006, "Null-field integral equations for stress field around circular holes under antiplane shear," *Engineering Analysis with Boundary Elements*, Vol. **30**, pp. 205-217.

2　Chen JT and Wu AC, 2006, "Null-field approach for the multi-inclusion problem under anti-plane shears," *ASME Journal of Applied Mechanics*, **Accepted**.

3　Chen JT and Wu AC, 2006, "Null-field approach for piezoelectricity problems with arbitrary circular inclusions," *Engineering Analysis with Boundary Elements*, **Accepted**.

(B) 會議論文

1　Wu AC, Shen WC and Chen JT, 2005, "Null-field integral equation for stress field around circular inclusions under anti-plane shear," *The 29th National Conference on Theoretical and Applied Mechanics*, Hsinchu, Taiwan.

2　Wu AC and Chen JT, 2006, "A new approach for piezoelectricity problems with circular inclusions," *The 8th National Conference on Structure Engineering*, Sun Moon Lake, Taiwan.